3-30-2022

Experimental Analysis and Numerical Investigation of Aerodynamics of Elevated Structures

Nourhan Abdelfatah
Florida International University, nabde006@fiu.edu

FLORIDA INTERNATIONAL UNIVERSITY

Miami, Florida

EXPERIMENTAL ANALYSIS AND NUMERICAL INVESTIGATION OF AERODYNAMICS OF ELEVATED STRUCTURES

A dissertation submitted in partial fulfillment of

the requirements for the degree of

DOCTOR OF PHILOSOPHY

in

CIVIL ENGINEERING

by

Nourhan Abdelfatah

2022

To: Dean John L. Volakis
College of Engineering and Computing

This dissertation, written by Nourhan Abdelfatah, and entitled Experimental Analysis and Numerical Investigation of Aerodynamics of Elevated Structures, having been approved in respect to style and intellectual content, is referred to you for judgment.

We have read this dissertation and recommend that it be approved.

_____
Arindam Gan Chowdhury

_____
Ioannis Zisis

_____
Seung Jae Lee

_____
Wallied Orabi

_____
Peter Irwin, Co-Major Professor

_____
Amal Elawady, Co-Major Professor

Date of Defense: March 30, 2022

The dissertation of Nourhan Abdelfatah is approved.

_____
Dean John L. Volakis
College of Engineering and Computing

_____
Andrés G. Gil
Vice President for Research and Economic Development
and Dean of the University Graduate School

Florida International University, 2022

DEDICATION

In the memory of my father, Mr. Sayed Abdelfatah (May Allah bless his soul).

I owe you this work and everything I achieved in life.

ACKNOWLEDGMENTS

Alhamdulillah, Thanks Allah the Almighty for His blessing and for giving me strength during my study and my whole life.

I would like to express my ample gratitude to my major advisor, Dr. Amal Elawady, for her mentorship, guidance, and continuous support since I joined her research group and through my Ph.D. journey. Giving me the opportunity to start experimental work from the first year to get more experience and do extensive valuable studies on my dissertation topic. I would like also to express my deepest gratitude to my co-major advisor, Dr. Peter Irwin. It was such a great honor to get the chance to work with him. I really appreciate his scientific support, and constructive ideas that enriched my dissertation.

I am eternally grateful to Dr. Arindam Chowdhury for his guidance through my courses and experimental test at the Wall of Wind Experimental Facility. I really appreciate his support, and encouragement. I sincerely appreciate Dr. Ioannis Zisis guidance during my first steps in numerical analysis. Many thanks for his valuable suggestions.

I would like to express my sincere gratitude and appreciation to the committee members, Dr. Seung Jae Lee and Dr. Wallied Orabi, for their help, continuous support, valuable suggestions, and insightful inputs.

Thanks to Dr. Armin Mehrabi, the Graduate Program Director at the Civil and Environmental Engineering department at FIU, for his guidance and support during my journey of doctorate degree study.

I would like also to acknowledge the support of my colleagues in the wind engineering team and the Wall of Wind staff for their help during my experimental work.

I am sincerely grateful to Mr. James Erwin, who helped me in the experimental work, and Dr. Mohammadtaghi Moravej, who helped me in the post-test analysis part.

I am thankful to the National Science Foundation (NSF) for supporting my research. The financial support provided by the NSF Award (Award# 1520853 & 2037899) is much acknowledged and appreciated. Furthermore, I would like to thank the University Graduate School (UGS) in Florida International University (FIU) for offering me the prestigious Dissertation Year Fellowship (DYF) to support writing and finalizing my dissertation.

A special feeling of gratitude is for my husband, Dr. Hassan Eldeeb. His unconditional love, support, and wisdom made the Ph.D. journey more pleasant. Thanks for being there for every challenge I face. And to our lovely son Hamza Eldeeb. He was born in the middle of this journey, and his patience allowed me to work hard on this dissertation. I hope I would be able to make it up to him.

Thanks to my mother, Ms. Hanaa Tantawy, who did her best to provide me with the best education and life. All the sacrifices she did, have made me what I am now. Nevertheless, my sisters' support, Eng. Mennatuallah and Dr. Rana who encouraged me during the Ph.D. journey. No matter the distance, you are the closest to my heart.

ABSTRACT OF THE DISSERTATION

EXPERIMENTAL ANALYSIS AND NUMERICAL INVESTIGATION OF AERODYNAMICS OF ELEVATED STRUCTURES

by

Nourhan Abdelfatah

Florida International University, 2022

Miami, Florida

Professor Amal Elawady, Co-Major Professor

Professor Peter Irwin, Co-Major Professor

In coastal residential communities, flooding is a frequent natural hazard that impacts the area. Elevated low-rise buildings are constructed to reduce the hydrodynamic load from surges and flooding. Yet, elevated buildings are exposed to high-intensity wind during hurricanes. Due to the current lack of information, wind loading on elevated coastal structures is not adequately addressed in current international guidelines. Post-storm damage assessment has revealed severe damages sustained by elevated buildings' components such as roofs, walls, and floor. Creating an air gap underneath the floor changes the structure's aerodynamics. Besides, the wind speed increase, due to elevation, causes an increase in the resulting wind loads. These factors result in a variation of the pressure distribution from their slab on grade counterparts. To address this knowledge gap, large-scale experimental studies were conducted at the Wall of Wind Experimental Facility at Florida International University, to assess wind effects on elevated houses. The experimental program was supplemented by numerical simulations using Computational Fluid Dynamics (CFD) to provide a visual explanation of the flow streamlines through

different configurations of coastal houses. The study covers different numbers of stories, varying stilt heights, different floor aspect ratios, number of stilts, and the effect of adding stairs. This study provides experimental and numerical aerodynamic datasets to assess local and area-averaged peak pressure coefficients for the building surfaces of the tested cases. From the experimental and numerical studies, the resulting external pressure coefficients compared to the provided coefficients by the international standards for on-ground cases show their applicability for elevated house walls and roof surfaces. For the elevated building floor underside surface, the provided external pressure coefficients for flat roofs, by ASCE 7-16, can be used while using the wind speed at the mean roof height as a reference. This study reveals a significant increase in the total shear, vertical forces, and overturning moment on the building foundations. The study also includes a visualization of the wind streamlines through the air gap showing the flow circulation below the model floor and behind every stilt. The provided flow streamlines justify the observed suction on the floor surface due to flow separation at the floor edges and around the stilts. The flow streamlines also show a considerable increase in the wind velocity passing through the air gap. Design recommendations and guidelines are proposed in the last chapter to adequately calculate wind loads on elevated buildings and increase the resiliency of coastal residential structures.

LIST OF CONTENT

CHAPTER PAGE

LIST OF TABLES

TABLE PAGE

LIST OF FIGURES

FIGURE PAGE

CHAPTER V

1. CHAPTER I

INTRODUCTION

1.1 Hurricane Hazards in Coastal Areas

Coastal areas attract high populations, due to the beautiful nature and weather, in the United States and around the world. Population migration to coastal cities results in the creation of many workforce opportunities in business and entertainment sectors. In the US only, more than 8 trillion dollars in goods and services, over 55 million employment opportunities, and income of more than 3 trillion dollars that total about 50% of the nation's economy were invested in coastal cities [1]. Such observation justifies that almost 40% of the world's population lives 100km or less from the coast, according to the United Nations [2]. In 1996, Hinrichsen estimated that by 2025 approximately 70% of the world population would live 200km from the shoreline [3].

The National Oceanic and Atmospheric Administration (NOAA) [4] has published tropical storms and hurricane records since 1851 in the Atlantic Ocean, the Caribbean Sea, and the Gulf of Mexico. Statistical analysis of the published extreme wind events showed a total increase of 36% in the number of storms over the past 50 years. In addition, currently, there is a 50% probability that ten storms will occur per year [5]. Thus, along the shoreline, residential structures are frequently exposed to strong windstorms and flooding hazards that cause severe structural damage resulting in significant economic losses and fatalities.

From the financial impact point of view, the losses of hurricanes are majorly expressed by the dollar amounts of insurance claims. Hurricanes (Harvey, Irma, and Maria) in 2017

resulted in claimed losses that exceeded $265B [6]–[8]. In 2018, Hurricane Michael's landfall near Mexico Beach, FL, impacted the region with wind speeds exceeding 67m/s and a storm surge exceeding 1.9m, causing insurance losses of more than $7.2 billion in Florida alone [9], [10]. Furthermore, in 2019, Hurricane Dorian, whose eye hit the Bahamas and its cone impacted Florida and South and North Carolina, resulted in insured losses of about $6.5 billion [11]. In 2020, the coastal areas of the US were hit by Hurricanes Sally, Laura, and Delta. The insured losses were estimated to be more than $15 billion for Hurricane Laura alone [12], [13].

The loss statistics, together with the increased number of rapidly intensified hurricanes, emphasize the fact that the recorded human and financial tolls from hurricanes of the last few decades have been immense and are expected to increase during the next years. This has led to calls for improving resiliency of the built environment in coastal areas. In an attempt to overcome flooding hazards impacting coastal communities, the Federal Emergency Management Agency (FEMA) recommends elevating coastal structures to a safe level, named the Base Flood Elevation (BFE), defined with respect to the structure's location relative to the seashore [14]. In many cases, this construction practice helps protect coastal houses against flooding hazards [15], [16]. In addition, several architectural benefits motivate owners to build their houses on stilts, such as increasing the natural ventilation by creating an air gap underneath the house floor, maximizing the aesthetic perspective of the house view, and allowing building houses in rocky areas [17]. Yet, the wind actions on such elevated buildings are critical and should be carefully considered.

1.2 The Necessity of Studying the Aerodynamics of Elevated Houses

Elevating residential houses to the Base Flood Elevation (BFE) is an effective way to avoid flooding hazards [14], [18]. However, damage assessment studies in the wake of recent hurricanes demonstrate that elevated homes remain vulnerable to wind hazards. Elevating a building on stilts changes its structural properties and exposes it to higher wind intensity. The building's new configuration allows the formation of new wind forces compared to an on-ground replica [19], [20]. After hitting the building windward wall, the flow streamlines experience a considerable change after elevation, as shown in Figure 1.1. The critical changes occurring due to house elevation are listed in the following points;

(1) The flow separation at the top and bottom edges of the windward wall is affected by the presence of air gap, consequently, it affects the resulting pressure distribution on the roof and walls.

(2) The air moving under the building passes through a narrow region where an increase in the wind speed is predictable, causing potential structural damages.

(3) The presence of stilts and the floor surface is expected to result in flow separation and turbulence, causing higher suction.

(4) The change in the pressure distribution over the surfaces and the suction force acting on the floor affect the resulting shear force and overturning moment on the foundation.

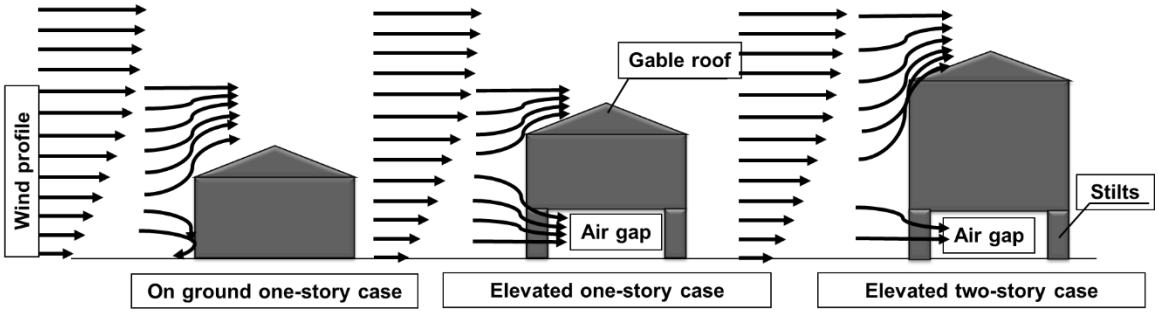

Figure 1.1 Schematic drawing of the air flow through gable roof houses

Figure 1.2 A one-story elevated house after hurricane Dorian in 2019

The stated aerodynamic changes resulting from elevating a low-rise building on stilts justify the considerable wind-induced damages experienced by numerous coastal buildings during recent hurricanes, including roof and wall cover loss [21], [22]. In the literature, Amini et al. showed several modes of damage experienced by elevated houses during Hurricane Michael [5]. The damage survey showed that the most common failure mode is the pull-out of wall and roof cladding. Figure 1.1 displays roof and wall damage of a one-story elevated house located in Abaco Island, Bahamas, after the impact of Hurricane Dorian. This structure is located 150m away from the shoreline. The severe damage displayed is believed to result from high-intensity wind and wind-borne debris impacts.

(a) (b)

Figure 1.3 Two-story elevated house wall and roof cladding damage (a) Hurricane Sally, and (b) Hurricane Laura

Similarly, Figure 1.3 (a-b) presents a typical wall and roof cladding damage observed on two-story residential houses recorded after the passage of hurricanes Sally and Laura, respectively [23]. The gable-roof elevated house shown in Figure 1.3a is located 300m away from Alabama's southern coast. The figure shows that more than 50% of the building wall cladding has been removed. The building shown in Figure 1.3b was hit by Hurricane Laura which caused severe damage to both the roof and wall cladding.

Despite the severity and destructive effects, there has been a little attention in the literature regarding the evaluation of wind actions on elevated coastal buildings. Holmes studied the effect of elevating a tropical house on the resulting surface pressure distribution [24]. The author tested on-ground and elevated models using small-scale 1:50 and 1:100 gable-roof models at the James Cook University wind tunnel facility in Australia. The eave heights of the on-ground and elevated models were 3.0 and 5.1 m, respectively. The roof pitch angle was 10°. The two models were tested only under three different wind directions of 0°, 60°, and 90°. The barrier-roughness method was adopted to adjust the scaling of the

flow with respect to the model size [25]. A rural terrain wind profile Atmospheric Boundary Layer (ABL) was produced, and the assumed roughness length was 0.035 m. The results showed a significant increase in the wall pressure coefficients, especially on the windward walls, as the model elevation increases. The increase of mean pressure coefficient on the windward wall was around 35% for 0° wind direction, and 30% for 90° and 60° wind directions.

Speaking about the scaling effects, Holmes observed discrepancies between the observed peak pressures measured using the 1:100 scale model compared to those measured for the 1:50 scale model. The smaller model showed lower peak pressure values, although the mean pressure coefficients recorded using the two scaled models were nearly the same. It was suggested that the reason behind such discrepancies was Reynolds Number (Re) scaling mismatch. Mismatching of Re similarity in wind tunnel testing is expected to affect the resulting peak pressures, especially for the corner zones subjected to oblique winds [26]. As a result, the use of large-scale models is recommended to reduce expected Reynolds number (Re) mismatching effects and increase the reliability of peak pressure values [27], [28]. Accurate consideration of Re is essential to reproduce corner vortices and flow separation and reattachment points [27], [29], and [30]. After testing a small scale (1:100) low-rise gable roof building, Hoxey et al. concluded that the Re effect could be as high as -0.5 in the pressure coefficient (C_p) value per decade of the Re values [28]. Recently, Moravej conducted a wind tunnel study using various scaled models of the Texas Tech Building [31] [32]. The largest-scale model (1:6) showed the best agreement in the external pressure distribution compared with the full-scale measurements. Additionally, a large-scale wind testing is preferred to reproduce better building details, which in turn

affects the aerodynamics of the building. On the other hand, for large-scale wind tunnel testing, it is typically not possible to simulate the full spectrum of turbulence eddies, particularly the large (i.e., low frequency) eddies, due to the limitations of the size of the test section. This may result in an underestimation of peak pressure coefficients. To address this issue, an analytical approach named Partial Turbulence Simulation (PTS) method has been previously developed and validated by the Wall of Wind (WOW) Experimental Facility (EF) research team to correct the measured peak wind pressures using large-scale models [33]. More details about the use of this analytical method are provided in the next chapters.

The topic of elevated houses aerodynamics has started to get higher focus in the recent years. Amini et al. conducted a parametric numerical study to evaluate the effect of elevating the structure on the resulting mean pressure coefficients using Computational Fluid Dynamics (CFD) simulations [34]. The study utilized the experimental results reported by Holmes [24] to validate their CFD model to further investigate other elevation heights and the wind flow characteristics. The author simulated a 1:20 on-ground and elevated (by 2.1 m and 4.2 m (full scale)) gable roof building. The results showed a slight increase in the suction coefficients on the roof surface for the examined elevated models. After counting the wind velocity increase and model elevation, the author stated that the increase of the pressure coefficients over the model surfaces caused an increase of 50 % and 95 % in the overturning moment acting on the 2.1 m and 4.2 m elevated cases, respectively, compared to the on-ground case. Also, Amini and Memari surveyed the performance of several coastal houses impacted by recent hurricanes [35] using publicly

available damage survey studies. The study recommended considering the new aerodynamics of elevated houses to resist higher levels of wind forces.

Very limited information is available in the current national and international standards for the design of elevated structures. For example, the American standard ASCE 7-16, provides external pressure coefficients for the edge and middle zones of the underside of elevated tanks or silos [36]. However, there is no recommendation for different elevations or geometrical changes. Besides, these values are recommended for cylindrical structures, which are not applicable for box buildings. This year (2022), the last released version of the American standard ASCE 7-22 include new provisions to calculate wind loads on elevated houses while considering the findings of the large-scale tests conducted in WOW [37], [38]. The Australian and New Zealand standard AS/NZS1170.2 [39] recommends using the same pressure coefficients values for the windward walls of elevated or non-elevated cases. For the floor surface, AS/NZS1170.2 standard recommends an averaged pressure coefficient value depending on the stilt's height while neglecting the effect of other geometrical configurations.

Both reasons, the lack of guidelines and the noticeable damages occurring due to hurricanes and extreme wind events, emphasize the importance of studying the aerodynamics of elevated structures, which is the main core of this dissertation's research aims. The external pressure coefficients on the structure surfaces are needed for an adequate design. Wind flow characteristics need to be investigated to avoid any future damages. The following section shows the objectives and the steps taken in the current study to fill the explained knowledge gaps.

1.3 Research Objectives

This research study constitutes two integrated experimental and numerical analyses of wind actions on elevated low-rise buildings. As a first step towards filling the current research gaps, a large-scale experimental program is conducted at the Natural Hazard Engineering Research Infrastructure (NHERI) Wall of Wind (WOW) Experimental Facility at Florida International University (FIU). The experimental study aims to provide an understanding of the main differences between the aerodynamics of elevated buildings compared to their on-ground replica and the role of the floor underside air gap in changing the wind flow surrounding the structure. The experimental program includes an on-ground case, different stilt heights, and different number of stories under varying wind directions. The test program is designed while considering the commonly used and the maximum stilt heights according to FEMA recommendations [14] and recent post-hurricane damage surveys [23]. The experimental study evaluates the local peak pressure coefficients on the building surfaces, including the roof, floor, and walls of typical elevated houses. These values are then used to calculate the wind loads on each surface cladding (i.e., area-averaged pressure coefficients).

The experimental study also includes a discussion on the differences between area-averaged pressure coefficients obtained from experimental data and those available in national and international standards. For the floor surface, a proposed empirical method is developed to provide the floor area-averaged pressure coefficients for different stilt heights. Also, to better understand the variation of wind loads with the variation of the house elevation, mean wind forces on the model surfaces are calculated and presented.

For the numerical simulations, Computational Fluid Dynamics (CFD) is used to simulate the air flow around elevated houses. Compared to experimental wind tests, CFD methods provide a wide range of output data to describe the air flow characteristics and the resulting wind loads. CFD is also distinguished by its ability to simulate different flow turbulence characteristics, atmospheric boundary layer profiles, and various building geometries at a low cost compared to conventional wind tunnel testing [40]. In this study, both Reynolds-Averaged Navier–Stokes (RANS) and Large Eddy Simulation (LES) models of elevated buildings, including those tested physically, are developed. The CFD models are first validated against the experimental results and then extended to assess the aerodynamics of other geometrical configurations. The RANS model can be an effective tool to perform an extensive parametric study to provide insights on the mean wind loading. However, it is insufficient to calculate peak velocity and pressures. LES simulation has shown the efficiency and accuracy of simulating wind flows through bluff bodies in literature [41]–[44]. It allows simulating time-dependent flow and calculating instantaneous velocity. The developed numerical models contribute to understanding the building aerodynamics, the change in mean and peak pressures along the model surfaces, and the damage modes observed in recent hurricanes. The wind flow characteristics are studied, and the resulting wind pressure effect is demonstrated as well.

The following bullets summarize the main research objectives of the dissertation;

1- Perform large-scale experimental wind testing on elevated houses with different stilt heights and number of stories.

   a) Analyze the experimental data to present the resulting pressure coefficient on the building surfaces.

b) Assess the sufficiency of available design guidelines and standard recommendations to calculate wind loads on elevated houses.

c) Propose guidelines to calculate external wind pressure on the floor surface.

2- Develop and validate a CFD model and conduct an extensive numerical parametric study.

a) Use the recorded experimental data to identify the boundary conditions and validate the numerical model.

b) Study the flow characteristics of the validated CFD models.

c) Perform parametric study to identify the geometrical controlling parameters that affect the aerodynamics of elevated houses (i.e., Stilt height, Aspect ratio, .etc.).

d) Perform CFD simulation using LES to estimate peak pressure coefficients.

1.4 Dissertation Structure

The structure of this dissertation is organized as follows to present the full study done to fulfill the research aims stated in the introduction "*Chapter 1*".

Chapter 2 introduces the wind effect on one-story elevated houses with different stilt heights through a large-scale experimental test at the Wall of Wind Experimental Facility (WOW-EF) at FIU. The test plan is designed to investigate how the air gap underneath the floor would change the aerodynamics of elevated buildings compared to their slab-on-grade counterparts. The test results are compared to their corresponding values given in the ASCE 7-16 standard when possible. The study proposes preliminary pressure coefficients and zone divisions for the floor underside surface, which is not currently available in the

design standards. The results of this study demand more parametric studies on elevated structures.

Chapter 3 presents an extensive experimental study on one- and two-story elevated houses with different stilt heights. The results are used to update the proposed zone scheme suggested in Chapter 2. Based on the suggested zoning, the pressure coefficients are calculated and compared to international standards. This study recommends examining other building shapes and stilt arrangements as well as the effects of partially blocking the underneath of the building which is widely noticed for elevated low-rise structures. Accordingly, to perform a parametric study, numerical simulations are needed to identify the controlling parameters with respect to the geometrical configurations and to understand the effect of the new aerodynamics on the flow streamlines.

Chapter 4 presents the RANS CFD model developed for elevated buildings. First, to validate the CFD model, a comparison between the data extracted from the CFD simulation with WOW results is conducted. Consequently, a parametric study is presented. This study investigates the wind flow characteristics surrounding the buildings while considering various geometrical configurations and assesses the wind actions on elevated structures and their variations with the building's stilt height and floor aspect ratio. The mean wind forces coefficients on the model surfaces and foundation are evaluated. However, the RANS simulations are limited to mean wind forces and pressure coefficients. Thus, to present peak pressure coefficients, Large Eddy Simulation is needed.

Chapter 5 presents a numerical study performed using Large Eddy Simulation. A simulation of an elevated model tested at the WOW EF is included in this chapter. First, the model parameters are validated by comparing mean and peak pressure coefficients

obtained using the LES simulations to the experimental results. Second, the instantaneous flow streamlines and the flow separation and vortex shedding beneath the model floor level are discussed. This chapter also includes a simulation to examine the effect of increasing the house floor aspect ratio and the number of stilts on the resulting peak pressure coefficients.

Chapter 6 Summarizes the research findings and the contribution of this study. It includes the proposed guidelines to calculate wind pressures on elevated houses' Component and Cladding. Some Recommendations for future work are added to this chapter as well.

2. CHAPTER II

A STUDY OF AERODYNAMIC PRESSURES ON ONE-STORY ELEVATED HOUSES

The importance of studying the aerodynamics of elevated houses is discussed in the Introduction chapter of this dissertation. To fulfill the main research aim about assessing the elevated houses' aerodynamics, a large-scale experimental study is conducted at the Natural Hazard Engineering Research Infrastructure (NHERI) Wall of Wind (WOW) Experimental Facility at Florida International University (FIU). The study provides an understanding of the main differences between the aerodynamics of elevated buildings compared to their on-ground replica. It also identifies the role of the underside air gap in changing the wind flow surrounding the structure. The experimental program considers one on-ground model and three different stilt heights (i.e., zero-stilt height) under varying wind directions. This chapter discusses the model configuration and instrumentation in section 2.1, and then the test program in section 2.2. Next, in section 2.3, the post-analysis methodology is explained. The results section (2.4) starts with evaluating the peak pressure coefficients on the roof, floor, and walls of the tested elevated houses. The area average peak pressure coefficients are also presented and compared with their corresponding values given in the ASCE 7-16 standard when possible. These values can be used in calculating the wind loads on the components and cladding of each surface (i.e., area-averaged pressure coefficients). They can also help in the design of the building foundations. Then, it presents a proposed empirical method to evaluate the floor area-averaged pressure coefficients for different stilt heights.

2.1 Model Description and Test Objectives

A typical low-rise gable roof building model is adopted for this study. The prototype dimensions are 8.76 m long, 6.4 m wide, and 3.8 m high. The roof pitch slope is 18°. To examine the effect of elevating a structure on the wind pressure distribution, four different stilt heights are adopted for this study: zero-stilt (e.g. slab-on-grade), 0.6 m stilt, 2.15 m stilt, and 3.65 m stilt. The chosen geometric configurations represent typical elevated houses in the coastal regions of the United States. Only four stilts are used to elevate the models to assess the wind effect on the raised floor surface while minimizing the shielding effect of any intermediate column. The building roof angle and floor aspect ratio are chosen to match with typical configurations found in surveyed damaged elevated houses after the impact of Hurricane Irma [23].

A large length scale of 1:5 is chosen for this test. The large length scale enables a relatively high Reynolds number of about 1.3×10^6 to be achieved. This increases the level of confidence in the resulting peak pressure coefficient. Moreover, the ratio between the area of the building model and the area of the test section, also known as the blockage ratio, is less than 5% to minimize blockage effects [45]. The test model is constructed using 5x10 cm wooden members for internal frames and four edge 10x10 cm wooden members for the stilts. The surfaces of the test models are covered by 9-mm thick polycarbonate panels. Figure 2.1 shows an illustrative plan view of the test model on the turntable of the WOW facility.

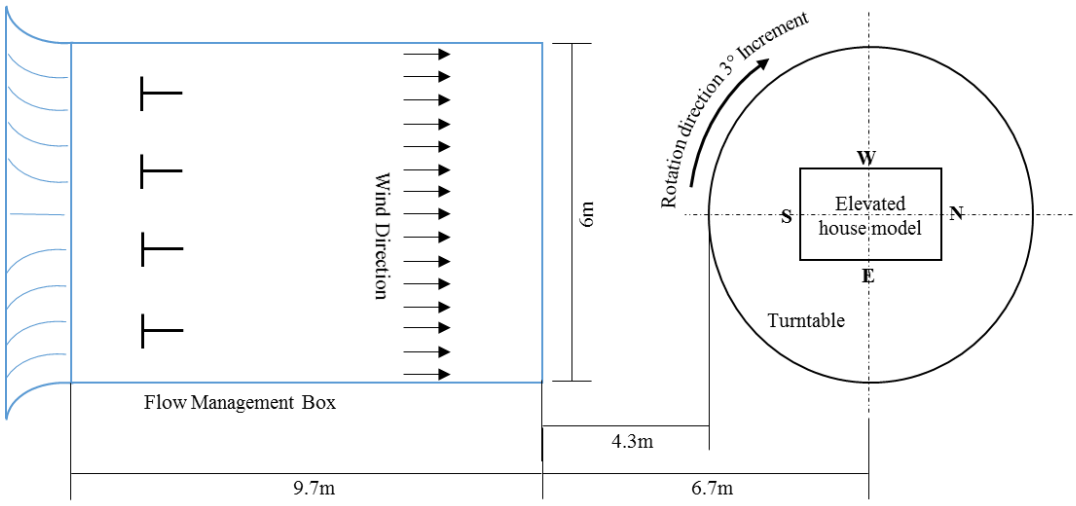

Figure 2.1 Plan view of the test arrangement

All models are tested under wind directions ranging between 0° to 90° in 3° increments. A schematic of the model showing the geometric notations used in this study is provided in Figure 2.2, and the building dimensions for each test case are given in Table 2.1.

Table 2.1 Summary of stilt house dimensions

Building, Scale	Length (*L*)	Width (*B*)	Height (*H*)	Stilt Heights (*SH*)
Full scale, 1:1	8.76 m	6.4 m	3.8 m	0.0, 0.6, 2.15, 3.65 m
Test Model, 1:5	175 cm	128 cm	76 cm	0.0, 12, 43, 73 cm

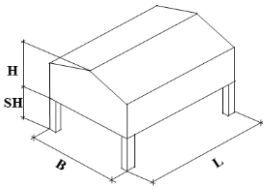

Figure 2.2 Model schematic

2.2 Experimental program at the Wall of Wind Experimental Facility

The Wall of Wind (WOW) Experimental Facility (EF), located at FIU, is a large-scale open-jet wind testing facility. The WOW contains 12-fans arranged in two rows in an arc shape. The WOW is capable of producing wind speeds that reach up to 70 m/s, which is equivalent to a Category 5 hurricane on the Saffir-Simpson Scale [46], [47]. Figure 2.3

shows the WOW intake and a 6 m x 4.3 m flow management box which encloses roughness elements and spires to simulate Atmospheric Boundary Layer (ABL) flows. The facility is equipped with an automated turntable of 4.9 m diameter that allows rotations of the test model to simulate different wind directions. More design details and testing capabilities of the WOW are provided by Chowdhury et al. [46].

(a) (b)

Figure 2.3 Wall of Wind facility (a) WOW 12-fans intake, and (b) downstream flow management

As shown in Figure 2.4, the large-scale models are fixed at the center of the turntable at the WOW EF. The tested cases are named with reference to their scaled stilt height: (a) zero-stilt, which represents an ordinary slab-on-grade low-rise gable roof building, and it is used for comparison purposes with the elevated house cases, (b) 12-cm stilt, which represents a full-scale stilt height of 0.6 m (e.g., typical elevation for mobile homes), (c) 43-cm stilt, and (d) 73-cm stilt. The last two cases are decided to present typical elevated houses with full-scale stilt heights of 2.15 m and 3.65 m, respectively. These elevations are identified from a recent damage assessment survey [23].

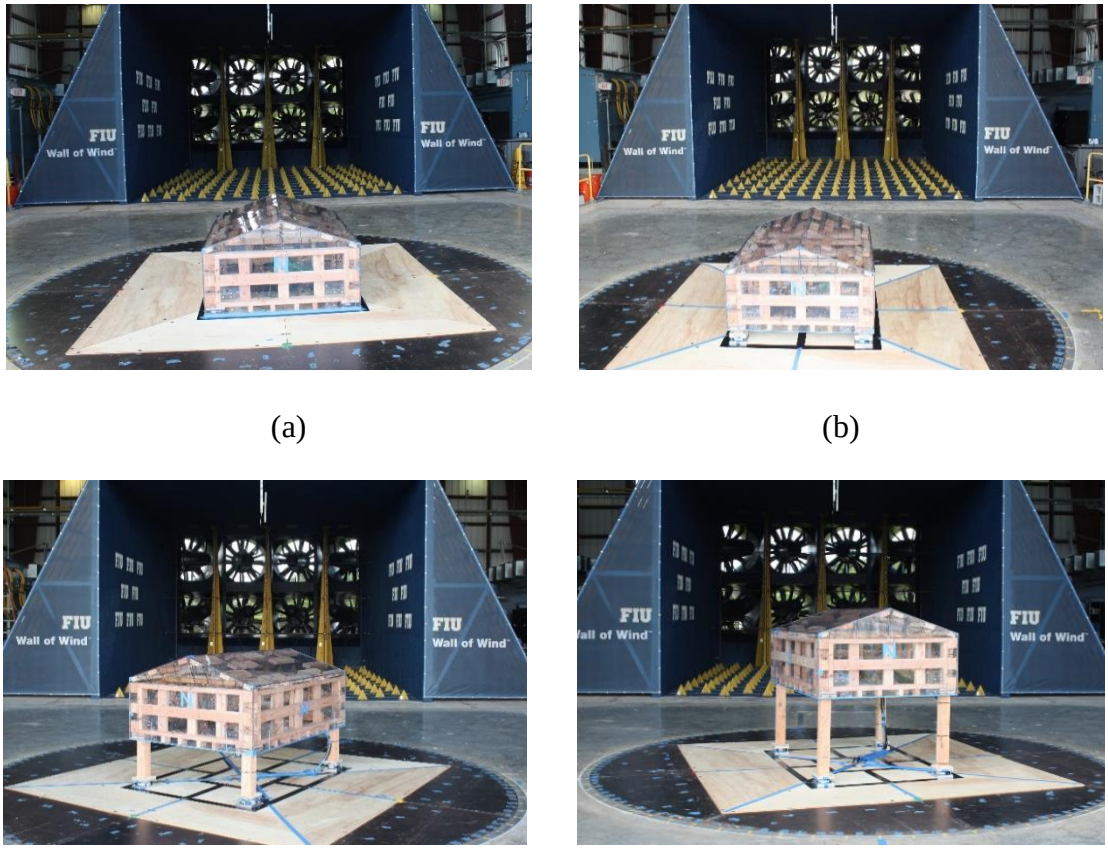

Figure 2.4 Four test models at the WOW EF (a) 0 stilt, (b) 12-cm stilt, (c) 43-cm stilt, and (d) 73-cm stilt

Cobra probes, which are capable of measuring the three components of the wind velocity, are used to measure the velocity profile before placing the model on the turntable (Figure 2.5a). Cobra probe measurements are also taken at the roof mean height of each test case (e.g., 65.5 cm for zero-stilt, 77.5 cm for 12-cm stilt, 108.5 cm for 43-cm stilt, and 138.5 cm for 73-cm stilt). A sampling frequency of 2,500 Hz is used for cobra probes measurements. For all the test cases, the WOW fans are operating at 40% throttle equivalent to a mean wind speed of 28 m/s. This throttle rate is chosen to optimize the test without exceeding the pressure measurement range of the pressure scanner.

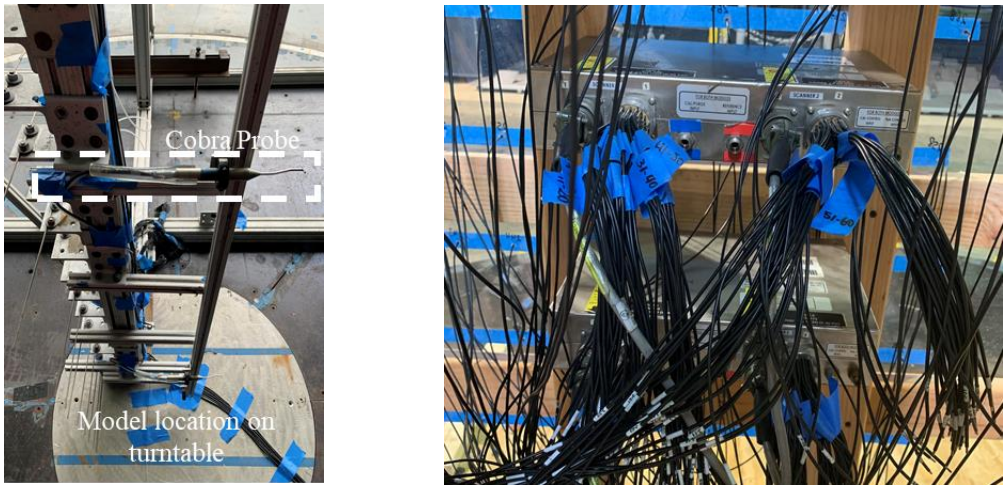

(a) (b)

Figure 2.5 Test instrumentations used during the test (a) Cobra probes, and (b) Scanivalve ZOC33

Scanivalve ZOC33 pressure scanners are used to measure wind pressure time histories. All the instruments are calibrated before starting the test. 375 pressure taps are distributed over the building surfaces, as shown in Figure 2.6. The pressure taps are connected to a total of six Scanivalve ZOC33 pressure scanners using flexible tubes, as shown in Figure 2.5b. The tubes used are 1.2m in length and their inner diameter is 1.3mm. The figure shows that a relatively dense distribution is used at the model edges to capture high-pressure gradients expected near the corners and edges.

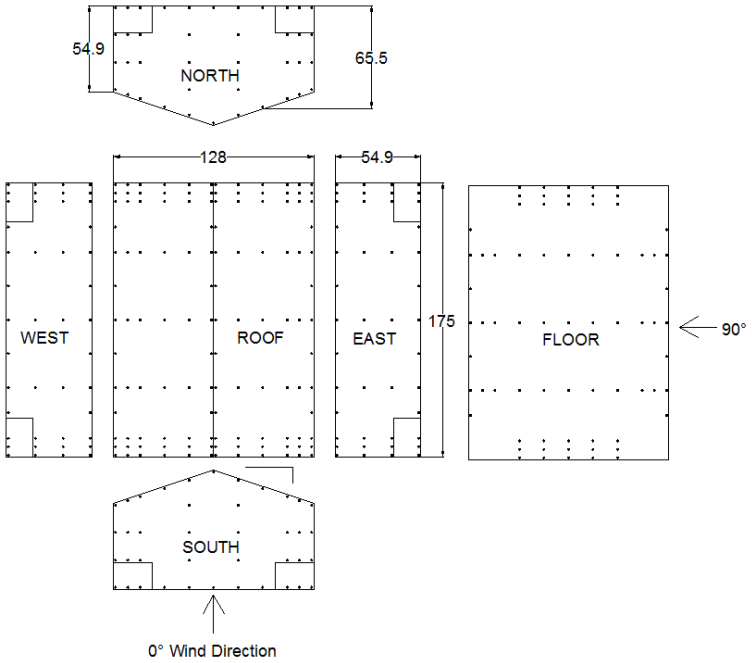

Figure 2.6 Pressure taps location on the walls, floor, and roof of the scale model (all dimensions are in cm)

Pressure data are recorded with a sampling rate of 520 Hz. For each of the tested cases, the test duration is 60 seconds. Flow field parameters are adjusted to simulate an open terrain exposure. Figure 2.7 shows the normalized mean wind velocity (U/ U_{ref}) obtained for an open terrain exposure along the height; Z, normalized to the reference height, Z_{ref}, at 10 m in full-scale. The reference wind speed, U_{ref}, is the mean wind speed at the reference height. The resulting turbulence intensity did not precisely match the full-scale counterpart, as shown in Table 2.2. This is because the turbulence spectrum simulated for the large-scale testing lacks part of low-frequency turbulence. Consequently, the resulting pressure-time history is corrected using the Partial Turbulence Simulation (PTS) technique to compensate for the missing turbulence. More details about this method are discussed in section 2.3.

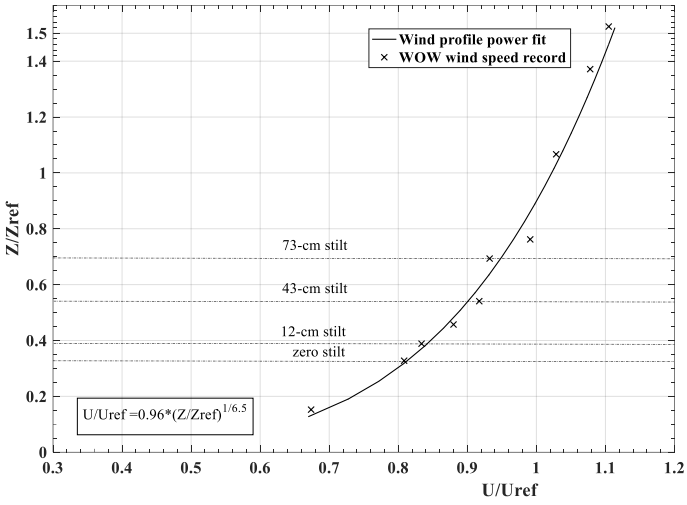

Figure 2.7 Vertical profile of the mean velocity

2.3 Data Analysis and Methodology

As mentioned earlier, the WOW fans, spires, and roughness elements are adjusted to produce the wind profile of the open terrain category. As expected, the relatively long length of the pressure tubing causes some distortion during pressure-time history data collection. The distortion of pressure signals caused by the tubing is compensated for using the inverse transfer function method described by Irwin et al. [48], and a low pass filter at 250 Hz is applied. The Transfer Function causes the deviation RMS between the long tubing data and short tubing data to reach $2x10^{-4}$. Then, the pressure coefficients for each pressure tap are calculated using Eq. (2.1).

$$C_P = \frac{\mathrm{P}}{\frac{1}{2}\rho V^2} \tag{2.1}$$

where ρ is the air density, P is the peak differential pressure (difference between the model surface and the reference pressure), *V* is the 3-sec gust wind speed at the mean roof height for each stilt case.

The limited test section size impedes the ability to form large eddies with respect to the model size. As a result, a deficiency in the low-frequency content of the wind tunnel spectrum occurs and, unless compensated for, would lead to an underestimation of peak pressure coefficient values. Figure 2.8 shows the normalized wind speed turbulence power spectrum at the building roof height compared to the Von Karman spectrum curve. The full-scale spectrum curve is obtained using a surface roughness length, z, equal to 0.08 m, equivalent to the open terrain exposure simulated at the WOW. In the plot, the frequency is denoted as n (Hz), the turbulence power spectrum is denoted as S, and the mean roof height is denoted as z (m). The mean wind speed (U) and turbulence intensity (I_u) are calculated at the mean roof height of each stilt case. Using the Engineering Sciences Data Unit (ESDU) [49], the full-scale non-dimensional longitudinal turbulence spectral density is computed for a coastal region using the ASCE Minimum Design Loads and Associated Criteria for Buildings and Other Structures (ASCE 7-16). These figures illustrate the missing low-frequency part for all cases. To ensure the accuracy of the estimated peaks, the partial turbulence simulation (PTS) method is used to compensate for missing low-frequency content in the peak estimation process.

The PTS is an analytical method based on the quasi-steady theory assumptions. The method depends on matching the non-dimensional power spectrum of the longitudinal turbulence for the large-scale model and the full-scale spectrum for the high frequencies. Then, assuming a Gaussian probability distribution for the low-frequency turbulence, the PTS method combines the low-frequency effects with the high-frequency data obtained in the wind tunnel in order to include the entire spectrum. The peak pressure coefficients can

be estimated by dividing the sample period into subintervals where peak values could be treated as independent. Each subinterval has its own peak value. And the probability that this peak is not exceeded in one hour at full scale is set at 0.78. Figure 8 shows that at high frequencies of the model spectrum and the full-scale spectrum successfully match each other. After adjusting the resulting pressure coefficients using the PTS method, the peak values are calculated at full scale. These procedures are done for each stilt height using the flow characteristic parameters listed in Table 2.2.

Table 2.2 Normal flow characteristics used for partial turbulence simulation analysis

Test Case / Parameter	Case 1		Case 2		Case 3		Case 4	
	Full scale (ESDU)	Scale model	Full scale (ESDU)	Scale model	Full scale (ESDU)	Scale model	Full scale (ESDU)	Scale model
I_u(%)	22%	14%	21%	13%	20%	11%	19%	9%
${}^{x}L_u$(m)	18.15	0.5	22.65	0.5	34.63	0.5	47.45	0.5
H (m)	3.274	0.65	3.8	0.77	5.40	1.083	6.93	1.38
U (m/s)	45.76	20.01	46.59	20.63	48.24	22.69	49.52	23.07

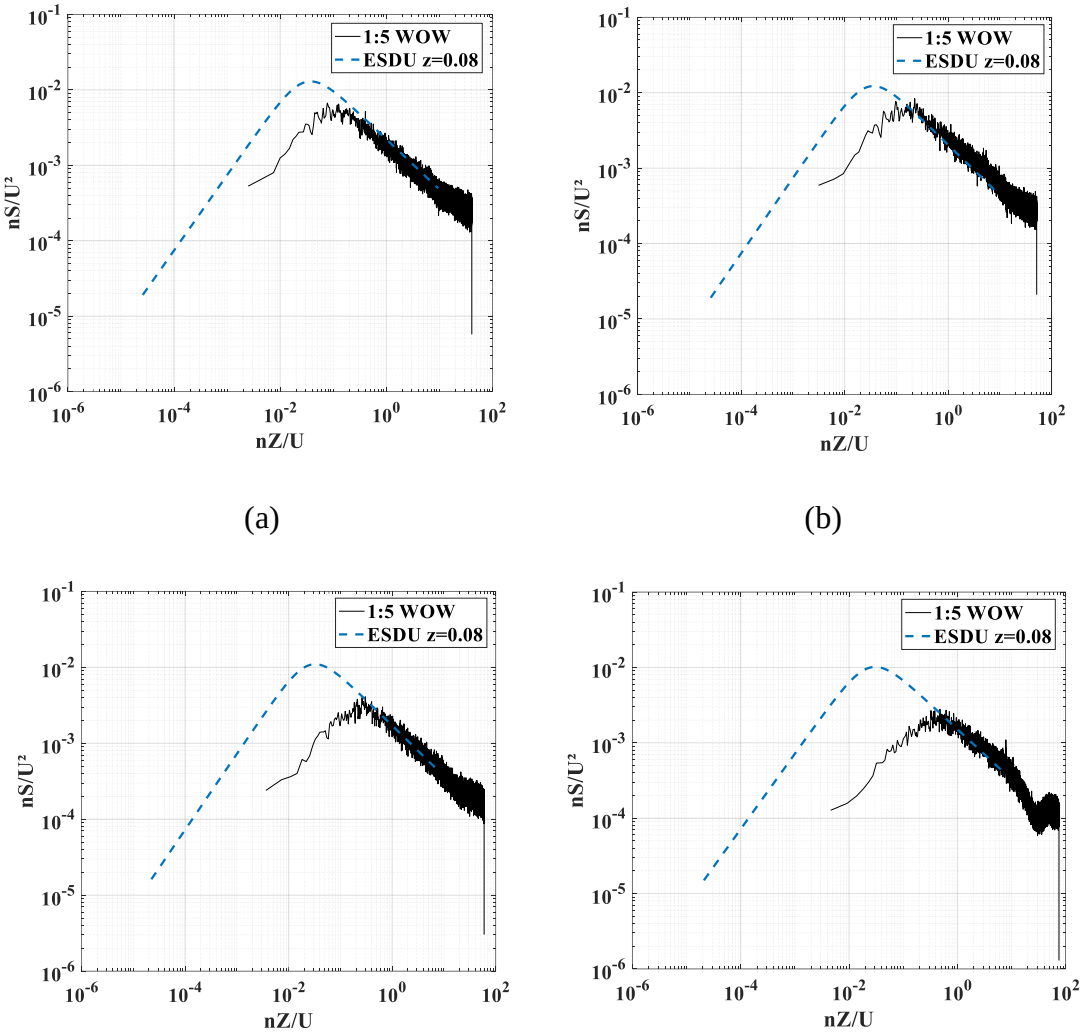

Figure 2.8 Turbulence power spectra of the WOW four stilt cases and full-scale (ESDU) for an open terrain (a) 0 stilt, (b) 12-cm stilt, (c) 43-cm stilt, and (d) 73-cm stilt

In addition to presenting the local point peak pressure coefficients and distribution, area-averaged peak pressure coefficients are calculated to gain an insight into the wind loads acting on components and cladding elements. Following the ASCE 7-16 Standard provisions [36], the procedure of averaging the local pressure values for different effective

areas for all wind directions up to 360º is adopted, as explained by He. et al. [50]. These procedures are applied as follows:

(1) The zone boundaries for the walls and roof are specified with respect to the zoning procedure described in the ASCE 7-16 standard for the Component and Cladding chapter.

(2) The zone dimensions are calculated based on the full-scale dimensions of the study building and then are scaled down to the model scale.

(3) For each zone, several possible tributary areas (e.g., representing roof components and cladding affected by wind) are identified.

(4) For every possible tributary area, the resulting pressure-time history of the enclosed taps is averaged over the specified tributary area, and the corresponding area-averaged time histories (C_{Pavg}) are computed.

(5) The PTS technique is then applied for each of the calculated C_{Pavg} to compensate for the missing low-frequency turbulence and estimate the corrected averaged peak pressure coefficients ($C_{P, avg, peak}$).

(6) The variations of $C_{P, avg, peak}$ with respect to the tributary area considered are plotted.

(7) The plotted lines are interpolated or extrapolated as needed and the $C_{P, avg, peak}$ value corresponding to a tributary area of 0.9 m^2 (full-scale) is obtained and recorded.

The tributary area of 0.9 m^2 is selected to match the one recommended by the ASCE 7-16 Standard for the smallest effective wind area for the Components and Cladding.

2.4 Results and Discussion

As mentioned earlier, each stilt model is tested under varying wind directions ranging between 0° to 90°, with the remaining directions being covered by considerations of symmetry. Therefore, the peak pressure coefficients obtained from the four quarters of the

building are used to identify and plot the most critical peak pressure coefficients. Hence, the current representation addresses the worst-case wind effect over the full range of wind directions (i.e., 0° to 360°). This section starts by showing the distribution of local point peak pressure coefficient. Then, the analysis adopted to obtain the area-averaged pressure coefficients is discussed. Finally, the test results are compared to their corresponding values given in the ASCE 7-16 standard when possible.

2.4.1 Local peak pressure coefficient distribution

The absolute maximum peak pressure coefficients obtained from all tested wind directions are determined and plotted. Starting with the zero-stilt case, Figure 2.9 shows the peak pressure coefficients over the roof, and the walls after applying the PTS technique (C_{Ppeak}). The symbols S and E denote the position of each wall of the building (South wall, and East wall, respectively). Due to the symmetry of the building, the results are presented only on the East and South walls. Figure 2.10 to Figure 2.12 show the contour plots for the cases of 12-cm stilt, 43-cm stilt, and 73-cm stilt, respectively. For the roof surface, Figure 2.9 to Figure 2.12 show minor changes when the stilts are introduced and when stilt height increases. High suction areas are observed along the roof edges and ridge for the four tested cases with C_{Ppeak} reaching a maximum suction of -3.8 at certain taps in the ridge area. These observations agree with the Moravej et al. [51] findings that reported no significant variations of the pressure coefficients for a slab-on-grade gable roof structure as the wall height increases. This means that the flow streamlines surrounding the roof are not highly affected by the increase in the elevation. The areas of the high suction where the flow separation occurs are similar at the edges and along the roof ridge. For the wall surfaces of the zero-stilt case, Figure 2.9 shows that the maximum C_{Ppeak} is around 1.4 at the south and

east walls. For the three elevated cases, the positive C_{Ppeak} along the south and east walls does not show a considerable change compared to the zero-stilt case. Only the 12-cm stilt south wall shows a slightly higher C_{Ppeak}. The positive C_{Ppeak} is large over the whole surface of the on-ground case. However, the elevated cases experience lower C_{Ppeak} at the lower zone next to the floor surface. This is due to the presence of the air gap where the wind outflows, unlike the on-ground case. The negative C_{Ppeak} values are higher on the lower part of the walls near the floor surface because of the flow separation at the lower edge of the walls.

For the floor surface, the results depicted in Figure 2.10 to Figure 2.12 show a change in the distribution of the C_{Ppeak} as the stilt height increases. The area of critical suction is observed to be greater in the case of taller stilts. The negative pressure coefficient values for the 12-cm stilt case range between -0.9, and -3.2, while for the 73-cm stilt case, the range is found to be from -1.95 to -3.4. The variation of the positive C_{Ppeak} in the floor surface is not significant compared to the negative C_{Ppeak} distribution. The 12-cm stilt case experiences lower C_{Ppeak} ranging between 0.2 and 0.5. As the stilt height increases, the positive C_{Ppeak} increases with a maximum of 0.7 in the 73-cm stilt case. Generally, the pressure coefficient contour of the floor surface is similar in shape to a flat roof surface. However, for the floor surface, the extent of the suction region increases with the increase in the stilt height. This is because of the size difference of the vortices formed below the house, which depends on the air gap's height beneath the floor. These vortices are found to be more pronounced for the oblique wind directions ranging between 30º and 60º.

In the study by Holmes, the resulting turbulence spectrum in case of the 1:50 model was not in a good agreement compared to the Von Karman Spectrum [24]. Holmes has pointed

out high negative pressure coefficient points at the corner area where pressure distribution is sensitive to the location and size of vortices. Those values agree with the current study's findings. Unlike Holmes [24], where only 3 wind directions are considered, the current study addresses the wind effect over the full range of wind directions (i.e., 0° to 360° in fine angle increments) which can enable developing design guidelines that account for worst loading cases. In addition, there is a good match with the response spectrum of the ESDU in the high-frequency region, which provides improved confidence in the measured peak pressures. The stated observations motivated the author to propose a simple criterion to calculate the area-averaged external pressure coefficients, as explained in section 2.3.

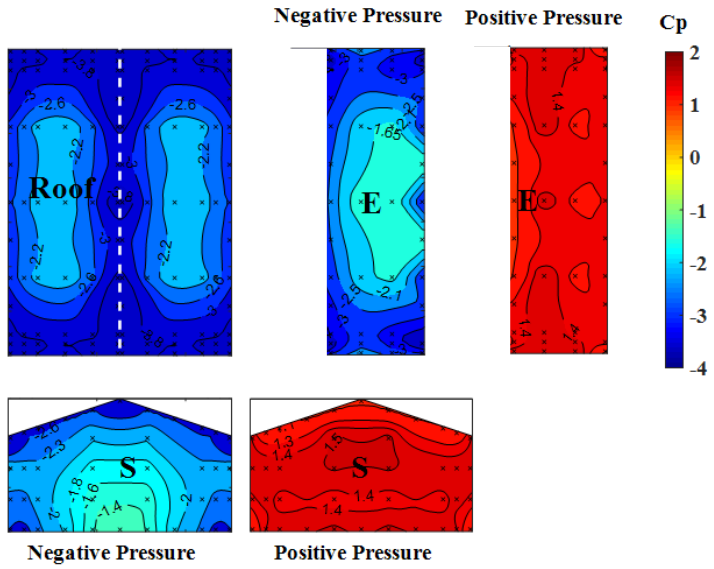

Figure 2.9 Maximum local peak pressure coefficients (C_{Ppeak}) among all wind directions for zero-stilt model

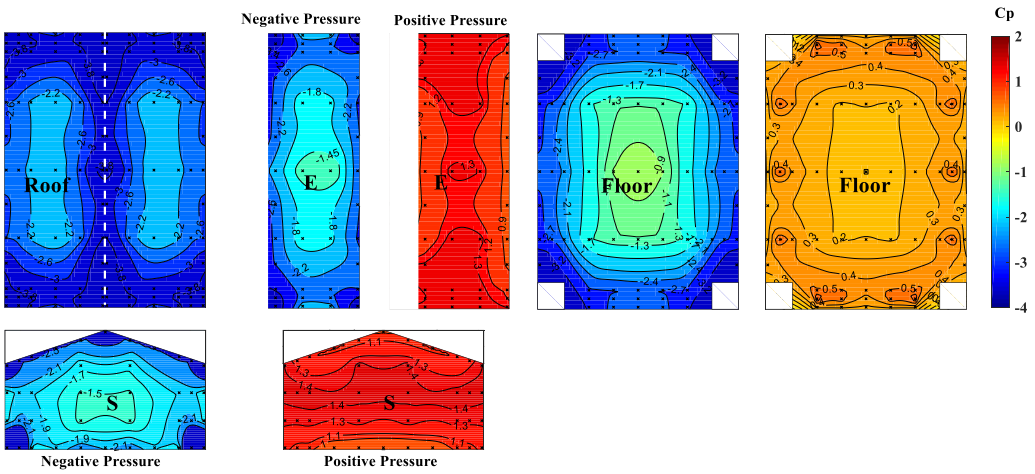

Figure 2.10 Maximum local peak pressure coefficients (C_{Ppeak}) among all wind directions for 12-cm stilt model

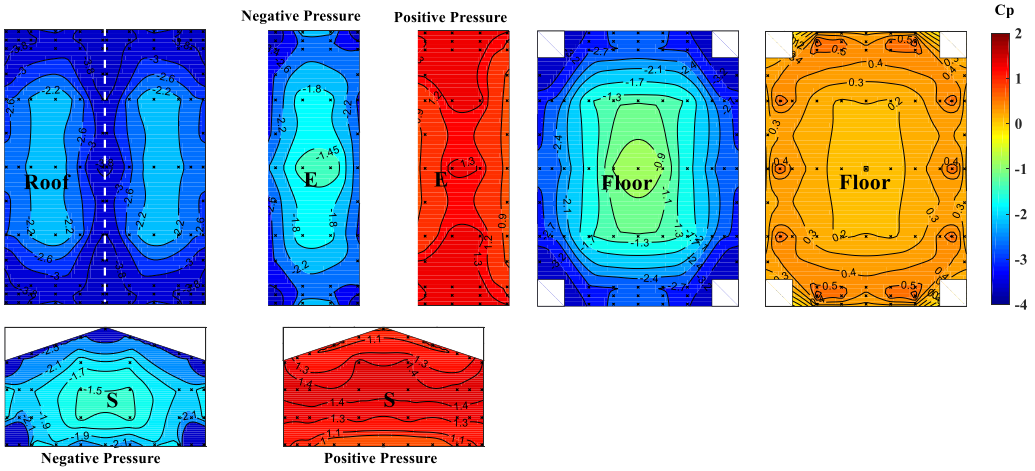

Figure 2.11 Maximum local peak pressure coefficients (C_{Ppeak}) among all wind directions for 43-cm stilt model

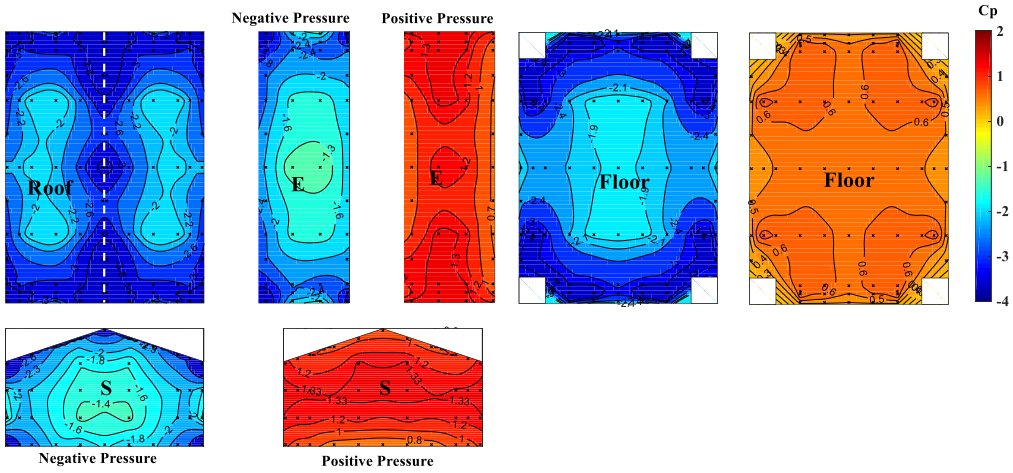

Figure 2.12 Maximum local peak pressure coefficients (C_{Ppeak}) among all wind directions for 73-cm stilt model

2.4.2 Estimation of area-averaged peak pressure coefficients

This section aims to evaluate the peak area-averaged wind pressure coefficient ($C_{P,\,avg,\,peak}$) that could be used to estimate wind loading on components and cladding zones following the recommendations provided by the ASCE 7-16. The analysis is done as explained in section 2.3. Figure 2.13 shows the roof zone division for the tested model according to the ASCE 7-16. The figure also shows the distribution of pressure taps located in each zone. For a roof slope of 18°, the dimension "a" in the figure is taken to be 0.9 m (full-scale) (18 cm model-scale). Considering zone 2n as an example, A1, A2, and A3 in Figure 2.13 are the possible "assumed" tributary area for the "component and cladding," and Ag is the total area of zone (2n). The area-averaged pressure coefficient time history $C_{P\ avg\ i}$ (t) corresponding to the selected tributary areas are calculated using Eq. (2.2).

$$C_{p\ avg\ i}(t) = \frac{\frac{\sum(P_i(t)*A_i)}{\sum A_i}}{\frac{1}{2}.\rho.V^2} \tag{2.2}$$

Where $P_i(t)$ is the pressure-time history for the tap T_i, A_i is the tributary area of the tap T_i. The procedure taken to calculate the $C_{P, avg, peak}$ is as follows;

(1) The tributary area A_1 which covers pressure tap "T_1" is calculated.

(2) The $C_{P\ avg\ 1}$ is calculated using Eq. (2.2). (3) The PTS is applied to compensate for the missing turbulence, giving $C_{P, avg, peak1}$.

(4) $C_{P\ avg2}$ is computed by averaging the two taps T_1 and T_2 enclosed in the total area of A_1 and A_2 using Eq. (2.2).

(5) PTS is applied on the resulting time history to get $C_{P, avg, peak2}$

(6) Similarly, $C_{P,\ avg,\ peak3}$ of A_g is computed using T_1, T_2, and T_3.

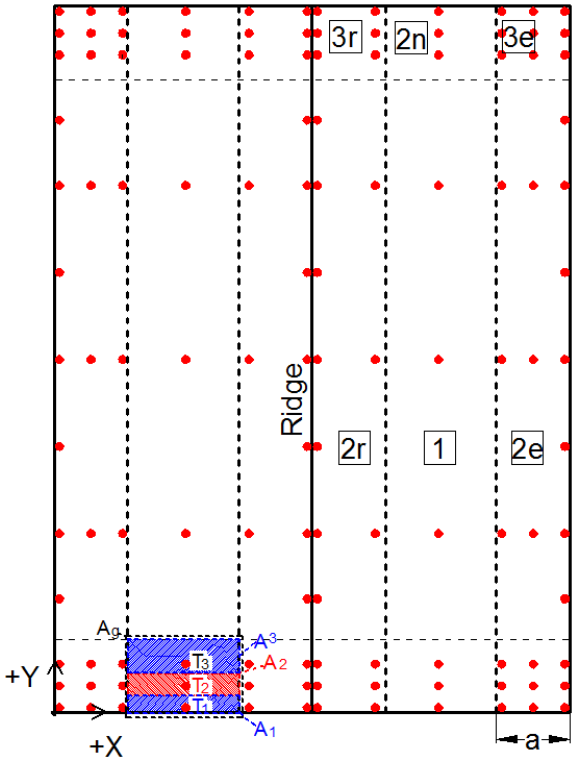

Figure 2.13 Pressure tap location through the zone boundaries of the roof surface according to ASCE 7-16

(7) The values of $C_{P, avg, peak1}$, $C_{P, avg, peak2}$, $C_{P, avg, peak3}$ are plotted against the corresponding tributary area in order to interpolate the $C_{P, avg, peak}$ corresponding to the tributary area of 0.9 m^2.

The following sections (2.4.1, 2.4.2, and 2.4.3) discuss the resulting values of $C_{P, avg, peak}$ for each of the model components, i.e., roof, walls, and floor, respectively.

For the zero-stilt case, the roof $C_{P, avg, peak}$ is obtained for all zones while considering the worst case of all tested wind directions. Figure 2.14a shows the $C_{P, avg, peak}$ for the zero-stilt

case, and Figure 2.14b shows the external pressure coefficients C_{Pext} provided by ASCE 7-16, in the Component and Cladding chapter. In the figure, the roof ridge is presented as a dashed line in the middle. In Figure 2.14, both $C_{P, avg, peak}$ plots (test results and ASCE 7-16) correspond to the tributary area of 0.9 m^2 in full scale. The figure shows that the values of $C_{P, avg, peak}$ obtained for the zero-stilt case are close to the C_{Pext} values recommended by the ASCE 7-16 in table 30.3-2B. It should be noted that for the ASCE 7-16, the C_{Pext} values cover a wide range of roof slopes (i.e., 7º-20º) and building heights (i.e., 0 to 18.3m). This may justify why the $C_{P, avg, peak}$ values at the edge zones obtained in the current study are slightly lower than those provided by the ASCE 7-16. This agreement is a good starting point for proceeding with the comparison of the stilt height effect.

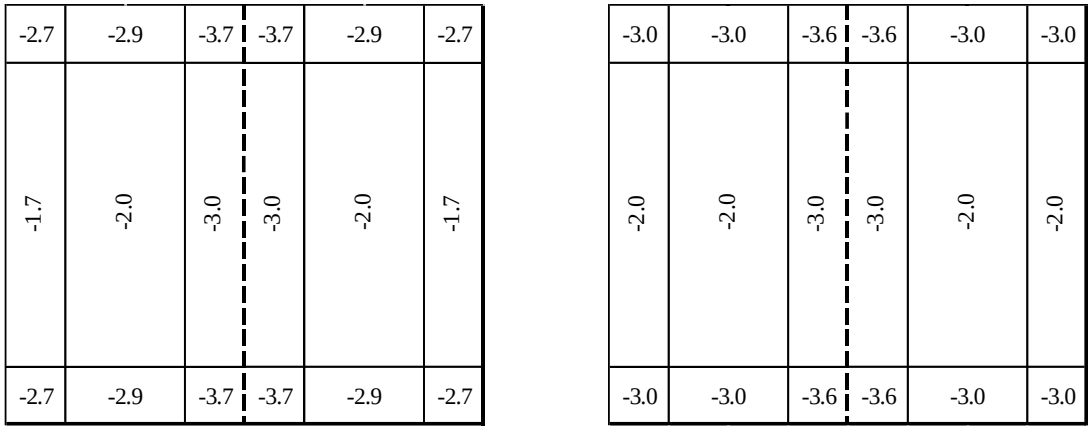

Figure 2.14 Comparison between WOW results and ASCE 7-16 a) $C_{P, avg, peak}$ obtained from WOW for zero-stilt model, and (b) C_{Pext} obtained using ASCE 7-16

Figure 2.15 compares the roof $C_{P, avg, peak}$ of the four tested stilt cases, including the zero-stilt case. In this figure, the roof $C_{P, avg, peak}$ values exhibit a slight tendency to decrease as the stilt height increases. A maximum reduction of 11% is observed at the corner zone between the zero-stilt and 43 cm stilt cases. It's worth mentioning that the pressure

coefficients are calculated for each stilt case using the corresponding 3-sec wind speed at the mean roof height. Therefore, this procedure considers the increase in the wind speed with the height in calculating pressure coefficients. This in turn means an increase in the global and local uplift wind forces on the roof as the mean roof height increases.

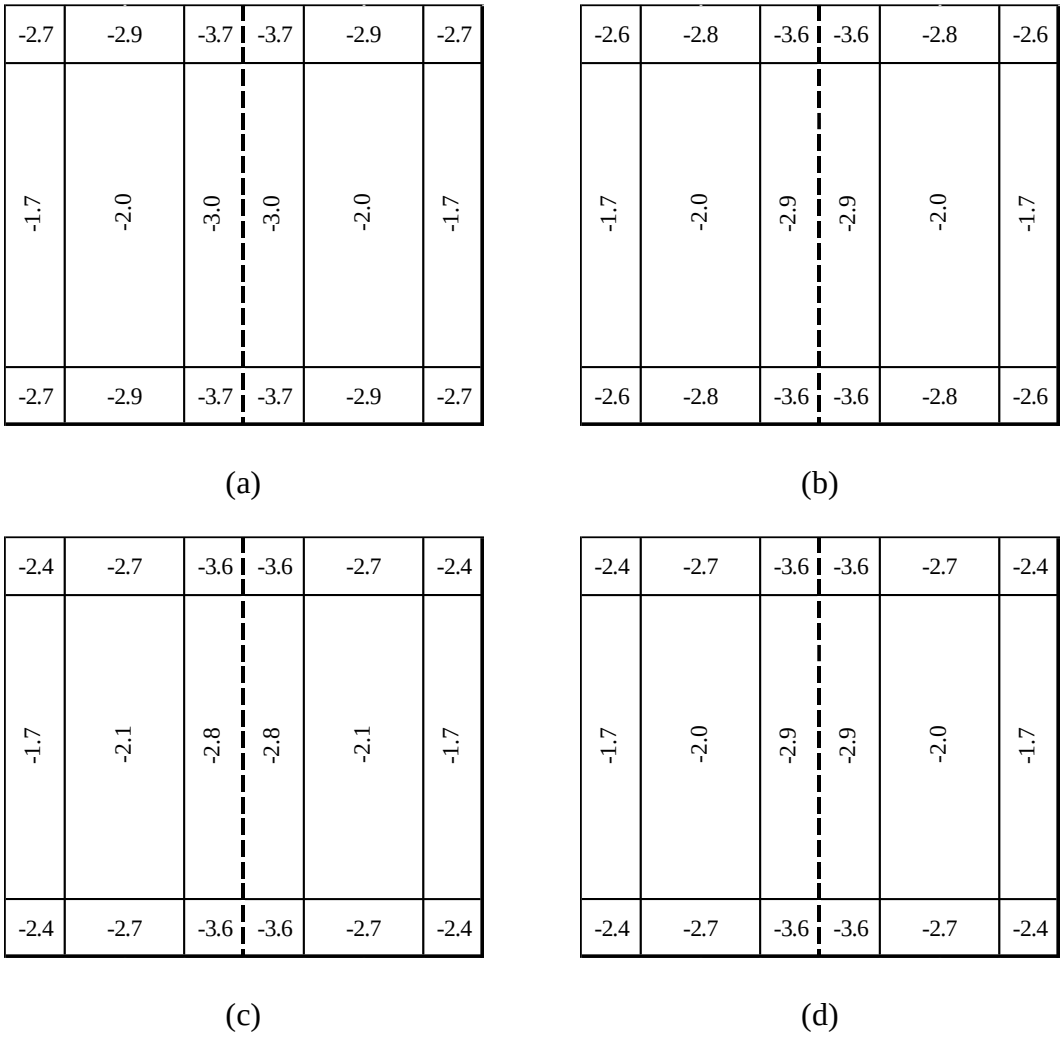

Figure 2.15 WOW $C_{P, avg, peak}$ on house's roof comparison of each stilt height (a) 0 stilt, (b) 12-cm stilt, (c) 43-cm stilt, and (d) 73-cm stilt

Similar to the analysis procedure described for the roof, this section presents the $C_{P, avg, peak}$ for the model walls. Following the ASCE 7-16 Component and Cladding chapter,

Figure 2.16 shows the zone boundaries for the gable walls. In the figure, the dimension is taken to be 0.9 m (full-scale) (18 cm model-scale). The C_{Pext} of the zero-stilt model is calculated using ASCE 7-16 provisions for the full-scale dimensions and provided in Tables 2.3-2.4. The tables show the negative and positive C_{Pext} values corresponding to a tributary area of 0.9 m^2 in the full scale, respectively. Also, for the test results, using the wall zones provided by the ASCE 7-16 (zone 4 and 5, see Figure 2.16), the area-averaged pressure coefficient for each zone $C_{P, avg, peak}$ is computed for each stilt as listed in Tables 2.3-2.4.

Table 2.3 Negative $C_{P, avg, peak}$ values on walls of each stilt model compared to C_{Pext} value of ASCE 7-16

Zone name	*Peak negative pressure coefficient ($C_{P, avg, peak}$)*				*C_{Pext}*	
	Zero-stilt	*12-cm stilt*	*43-cm stilt*	*73-cm stilt*	NIST	*ASCE 7-16*
4	-1.4	-1.4	-1.3	-1.3	-1.3	-1.1
5	-1.7	-1.7	-1.6	-1.8	-1.6	-1.4

Table 2.4 Positive $C_{P, avg, peak}$ values on walls of each stilt model compared to C_{Pext} value of ASCE 7-16

Zone name	*Peak positive pressure coefficient ($C_{P, avg, peak}$)*				*C_{Pext}*	
	Zero-stilt	*12-cm stilt*	*43-cm stilt*	*73-cm stilt*	NIST	*ASCE 7-16*
4	1.4	1	1	1	1.5	1
5	1.2	1.1	1	1.1	1.3	1

As for the wall suctions, Table 2.3 shows that the negative $C_{P, avg, peak}$ values do not experience much change as the stilt height increases. $C_{P, avg, peak}$ of the zero-stilt model is about 20% higher than the C_{Pext} value recommended by the ASCE 7-16. This difference slightly decreases as the stilt height increases except for zone 5 of the 73-cm stilt case. Table 2.4 shows that the positive $C_{P, avg, peak}$ values are much closer to the ASCE 7-16,

especially when the model is elevated. For the edge zone of the three elevated cases, $C_{P,\ avg,\ peak}$ positive value agrees well with values recommended by the ASCE 7-16 standard.

For the wall positive pressure, the zero-stilt walls exhibit 30% higher $C_{P,\ avg,\ peak}$ positive value than the C_{Pext}. The observed differences encouraged the author to conduct a further investigation by comparing the area-averaged pressure coefficients for the walls obtained from the current test to those values available within the National Institute of Standards and Technology (NIST) aerodynamic database for a similar gable-roof building. The chosen building has full-scale dimensions of 13.7 m length, 10.7 m width, and 3.9 m height. This building is tested on-ground using a length scale of 1:100 and a wind speed of 37.5 m/s for an open terrain exposure category. The NIST C_{Pext} values are provided in Tables 2.3-2.4. It is observed that the resulting C_{Pext} values obtained using the NIST database agree well with WOW $C_{P,\ avg,\ peak}$ values for the zero-stilt case. For the positive pressure coefficients, the NIST results are higher by 7%, while for the negative pressure coefficients, the NIST results are lower by 6%. Thus, the differences between the calculated $C_{P,\ avg,\ peak}$ and the C_{Pext} provided by the ASCE 7-16 and the NIST database are considered in the acceptable range. On the other hand, in the case of the on-ground and elevated structures, the Australian and New Zealand wind loading standard AS/NZS 1170.2 recommends using a single value of (0.8) for the windward wall.

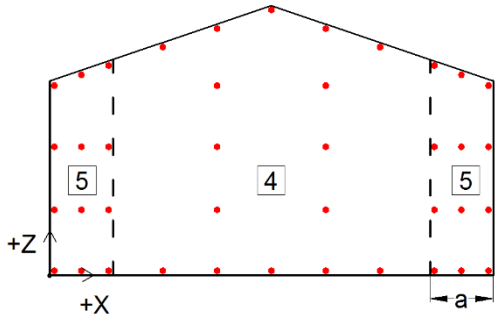

Figure 2.16 Pressure tap location and zone boundaries on south face according to ASCE 7-16

2.4.3 Proposed external pressure coefficients for the floor of elevated residences

The floor underside surface is a distinctive area from the perspective of the wind pressure distribution that has received little to no attention in the literature. The structural system supporting the floor needs to be designed adequately to avoid wind-induced failure in the beams, joists, and cladding. In addition, it is expected that the overall wind forces acting on the structure and the foundation would vary compared to an on-ground structure as a result of the additional forces on the floor underside. Figures 2.10 to 2.12 show that the wind load on the floor surface is highly affected by the size, number, and locations of the stilts. The resulting positive and negative wind forces on the floor surface should be considered in the design of the foundation. The compression force on the floor (i.e., positive pressure) increases the resulting structural uplift and overturning moment. The suction force decreases the overall uplift and overturning moment as it counters the suction force on the roof. In addition, the suction force may cause a punching force on the building floor slab against the columns. The objective of this section is to propose area-averaged peak pressure coefficients to be used for the floor surface for design purposes. The boundaries and zoning for the floor of elevated houses are proposed herein. Unlike the constant pressure coefficients recommended by ASCE 7-16 for the undersides of elevated tanks, the results obtained in the current study exhibits a noticeable change in the pressure distribution on the floor as the stilt height increases. The zoning scheme proposed in this chapter is based on observing the extent of the suction zones of the local peak pressure coefficients and their change with the increase in the stilt height. As discussed earlier, the high peak negative pressure region becomes larger as the stilt height increases, see Figures 2.10 to 2.12. In addition, high suction is found to be more severe near the edge columns,

which indicates the formation of the edge vortices. Figure 2.17 (a-b) shows the proposed zone boundaries for the 12-cm stilt height case. Following the zone numbering provided by the ASCE-7-16 for flat roofs (which is similar in geometry to the floor), the floor surface is divided into three regions: (1) middle area of the floor; (2) rectangular area along the floor edges; (3) L shaped area around the model columns. The zone width is considered as a variable named "a" in the current study. Empirically, this variable is found to be approximately equal to 0.3 of the mean roof heights for each stilt case while the length is found to be about twice the width (2a), as shown in Figure 2.17. The variable “a” is chosen to cover the high-suction zone at the edges and around the columns. It should be mentioned that the width and the length of the suggested zones are applicable only for the tested model dimensions. Also, they are applicable in case of using the wind velocity at the mean roof height while calculating the wind force on the floor surface. For this reason, more parametric studies are needed to check the validity of this finding on other shapes of elevated houses. This underlines the need for more research studies to confirm these observations for other building configurations (i.e., different floor aspect ratios, columns arrangements, etc.).

(a) (b)

Figure 2.17 Zone boundaries of the floor surface for 12-cm stilt model (a) zone dimensions, and (b) tap location in each zone

The next step is to determine the pressure coefficient for each suggested zone. Similar to the analysis adopted for the roof and the walls, the $C_{P,\,avg,\,peak}$ values corresponding to a tributary area of 0.9 m^2 are obtained. Figure 2.18 (a-c) shows sample plots of $C_{P,\,avg,\,peak}$ variation with tributary area for each zone for the 12-cm stilt case. The best fit line is drawn, then the $C_{P,\,avg,\,peak}$ value corresponding to 0.9 m^2 is extrapolated.

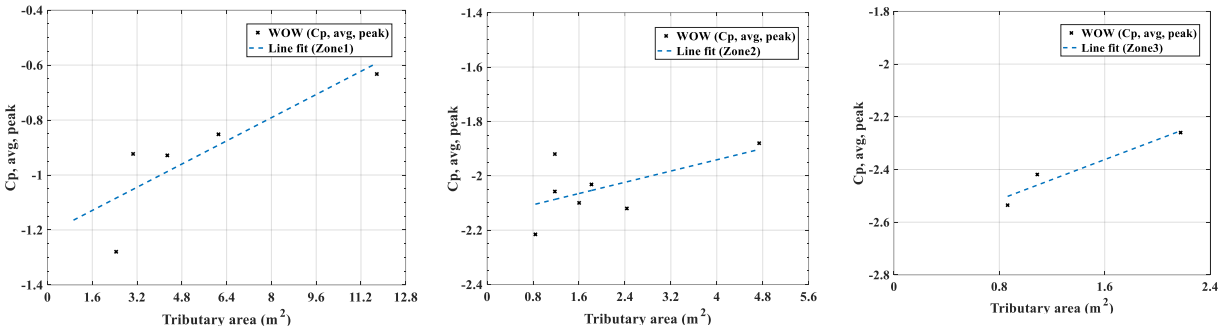

(a) (b) (c)

Figure 2.18 Estimating $C_{P,\,avg,\,peak}$ of the floor surface for 12-cm stilt model (a) zone 1, (b) zone 2, and (c) zone 3

This method is applied for each floor zone for all tested stilt height cases. The resulting $C_{P,\,avg,\,peak}$ values corresponding to a tributary area of 0.9 m^2 are shown in Figure 2.19. The figure shows that the $C_{P,\,avg,\,peak}$ of zones 2 and 3 do not experience a considerable change with the increase of the stilt height. However, the $C_{P,\,avg,\,peak}$ of the middle zone, increases significantly by increasing the stilt height; approximately 50% increase is noticed by increasing the stilt from 12-cm to 43-cm, and approximately an increase of 6 % is observed by increasing the stilt from 43-cm to 73-cm. This indicates an increase in the total suction force acting on the building floor with the increase in the stilt height. It should be noted that the $C_{P,\,avg,\,peak}$ values shown in Figure 2.19 are lower than the local peak values

presented in Figure 2.10 to Figure 2.12. This results from the lack of correlation between the local pressures at each tap considered in the area-averaging process, as clarified by (Beste and Cermak, 1997). The positive $C_{P, avg, peak}$ values are nearly equal along the floor surface. The calculated positive $C_{P, avg, peak}$ values in each zone are shown between brackets in Figure 2.19. The figure shows no significant difference between the zones positive $C_{P, avg, peak}$ for all stilt cases. It worth mentioning that the air gap beneath the building does not include any blockage (e.g., storage rooms or garages). For this reason, the positive pressure coefficient values are not significant in this case.

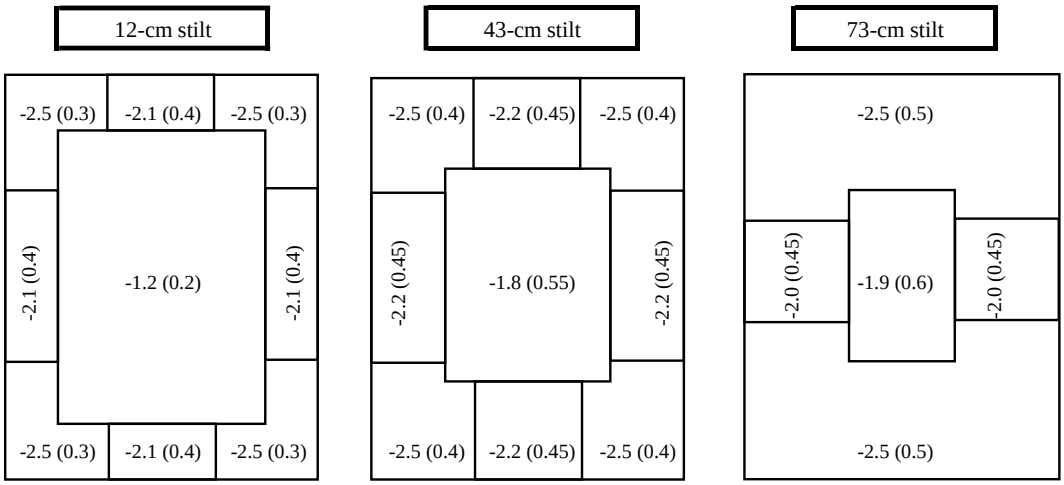

Figure 2.19 $C_{P, avg, peak}$ on floor comparison for three stilt models

As mentioned in the introduction, the Australian and New Zealand wind loading standard (AS/NZS 1170.2) provides the recommended external pressure coefficient for the underside of an elevated house. For the prototype of the current model, in the case of elevating the house by 0.6m (full-scale), the AS/NZS 1170.2 recommends using C_{pext} (-0.283 and 0.378). For the other two stilts, the external pressure coefficient C_{pext} is

recommended to be (-0.6 and 0.8). Table 2.5 shows a comparison between the C_{pext} values recommended by the Australian standard and the $C_{P, avg, peak}$ of the floor surface measured at the WOW. To compare with the single C_{pext} value provided by the AS/NZS 1170.2 standard, a new area-averaged pressure coefficient value on the whole floor surface is used instead of the ones presented in Figure 2.19. To calculate the $C_{P, avg, peak}$ for the whole floor, the measured pressure-time history on the floor surface of the WOW tested model is averaged for the whole surface. Then, the PTS is applied to calculate the peak values, as illustrated in section 2.3. The maximum-minimum negative values among all wind directions are provided in table 2.5. The table shows that the negative values in AS/NZS 1170.2 are slightly smaller in magnitude than what is observed in this study, except for the 12-cm stilt case where the WOW negative pressure coefficient is significantly higher than the value provided by the standard.

Table 2.5 Negative $C_{P, avg, peak}$ values on the floor of each stilt model compared to C_{Pext} value of AS/NZS 1170.2

	External negative pressure coefficient		
Stilt case	*12-cm stilt*	*43-cm stilt*	*73-cm stilt*
WOW	-0.76	-0.70	-0.73
AS-NZS	-0.283	-0.6	-0.6

In the future, it is recommended to test the elevated case with a partially closed air gap under the floor to determine the total positive force increase with height, as it would lead to a pronounced increase in the overall uplift and overturning moment acting on the building. Generally, both negative and positive wind loads should be considered to assure structural integrity and safety. More studies are encouraged to assess the variations of wind actions for typical configurations of elevated buildings. For future work, it is recommended

to study different roof shapes, floor aspect ratios, number of stories, and different arrangements of the stilts.

2.5 Conclusion

This chapter presents the effect of air gap beneath the elevated house model on the resulting peak pressures coefficients compared to their slab-on-grade counterpart. The following results are observed from the four large-scale models tested at the WOW EF. The local peak pressure coefficients, C_{Ppeak}, on the roof and the walls show minor changes as the stilt height increases. However, the aerodynamics of the floor is influenced by the stilt height. High suction regions are particularly observed for the floor surface around the columns and the edges. The extent of the high suction zones on the floor underside is more significant for higher stilt cases, and the magnitude of peak pressure coefficients is found to increase as the stilt height increases. The presence of the columns in the case of elevated houses contributes to the formation of floor separation, especially for oblique wind directions. These vortices are believed to be the main reason for the high suction region observed at the corners. The variation of the local positive C_{Ppeak} on the floor surface as a function of stilt height is not significant compared to negative C_{Ppeak}. However, both negative and positive pressures should be considered in the design of the floor surface as well as in estimating the loading on the foundation. Generally, it is expected that the size, number, and locations of the stilts affect the resulting wind loads, and thus more studies are needed to fill the current gaps.

The area-averaged pressure coefficients for the roof surface are in a good agreement with the C_{Pext} values provided by the ASCE 7-16 standard for a similar slab-on-grade building. These coefficients are calculated using the 3-sec wind speed at the roof mean

height. On the other hand, for the wall surfaces of the zero-stilt case, the resulting negative $C_{P,\ avg,\ peak}$ values tend to be higher than C_{Pext} provided by ASCE 7-16. For further investigation of the wall $C_{P,\ avg,\ peak}$ values, comparisons are done with the NIST database values of a similar building. This comparison shows a good agreement with the test results. With respect to the effect of the stilt height, the $C_{P,\ avg,\ peak}$ values on the roof surface show slight change for the three elevated cases. While for the walls, $C_{P,\ avg,\ peak}$ values are found to slightly decrease as the stilt height increases. It should be noted that the reference wind speed increases considerably for each larger stilt height, and thus the corresponding pressure value is expected to be higher.

The current study proposes pressure coefficients and zone divisions for the floor underside surface, which is not currently available in the design standards. The zone width of each stilt case is found to be correlated to the corresponding roof mean height of the elevated structure. The width and the length of the high suction corner and edge zones of the floor surface are found to increase as the stilt height increases. In the interior zone, $C_{P,\ avg,\ peak}$ values show a higher increase with the increase of the stilt height compared to the edge zones. The magnitude of the suction force acting downward on the floor underside surface increases by 30% with the increase of the stilt height. This should be considered in the building design as a function of the stilt height.

The current study results successfully introduced a new surface (floor) that has never been presented in detail. The pressure taps located over the floor surface successfully fulfill the study aim. However, it is necessary to densify the pressure taps over the high gradient regions and monitor the pressure distributions around the columns. In addition, more parametric studies are required on elevated structures. A wide range of real-world

geometric configurations should be considered, including larger aspect ratios, different numbers and locations of the stilts, and different numbers of building stories. The following chapters cover most of these recommendations to better understand the new aerodynamics.

3. CHAPTER III

A COMPARISON BETWEEN THE AERODYNAMICS OF ONE-STORY AND TWO-STORY LOW-RISE ELEVATED RESIDENCES

This chapter presents an investigation of the effect of increasing the number of stories and the stilt height on the overall wind actions on elevated buildings [52]. As explained in the introduction, this study aims to deliver a better understanding and to further reduce the current knowledge gap related to wind impacts on elevated coastal buildings. One-story and two-story gable roof residential houses are tested using four different stilt heights. Compared to the results stated in the previous chapter and published by Abdelfatah et al. [53], some adjustments are made in the current test phase to enhance the quality of the test and the results. The pressure taps are densified over the model surfaces, and an intermediate column is added in the middle of the longest span. The test program considered the maximum stilt height used for coastal houses according to FEMA recommendations [14] and recent post-hurricane damage surveys [23]. In this chapter, a summary of the test setup and the analysis strategy is included in sections 3.1 and 3.2, respectively. In section 3.3, contour plots of local peak pressure coefficients are presented. Section 3.3 also includes a discussion on the differences between area-averaged pressure coefficients obtained from the experimental data and those available in national and international standards for the on-ground case for the roof and wall surfaces. The area-averaged pressure coefficients on the floor surface are provided in section 3.4. To better understand the variation of wind loads with the variation of the house elevation, mean wind forces on the model surfaces are calculated and presented in section 3.5.

3.1 Experimental Procedures

The experimental program includes two main cases: (1) a one-story house and (2) a two-story house. Figure 3.1 shows a view of the flow management box and displays the arranged automated roughness elements and the vertical spires. These flow controllers can be adjusted to simulate the desired terrain category flow.

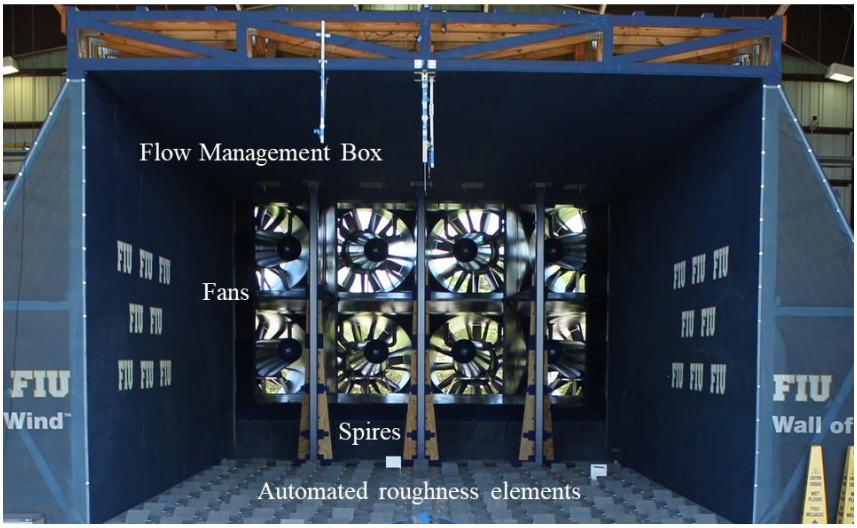

Figure 3.1 Wall of Wind 12-fans intake of the flow management box with automated roughness elements and spires.

The prototype on-ground dimensions are 8.76 m long, and 6.4 m wide. For the on-ground one-story and two-story cases, the model eave heights are 3.2m and 5.5 m, respectively. The roof pitch slope is 18°. In both test cases, the model is tested on-ground and then elevated with three different heights (full-scale): 2.15 m, 3.65 m, and 5.2 m. The models are tested using the same length scale of 1:5.

Unlike the model presented in chapter two, the long span is divided into two spans using two intermediate columns (Figure 3.2). Stilts used in elevated buildings are typically constructed with this small shift from the edges, according to FEMA [14]. Thus, a slight shift from the edge, 4.5 cm in the scale model, is taken at the outer side of each stilt, as shown in Figure 3.3. In addition, the pressure taps are distributed with a denser pattern, especially on the floor surface (Figure 3.3), to enhance the accuracy of the results.

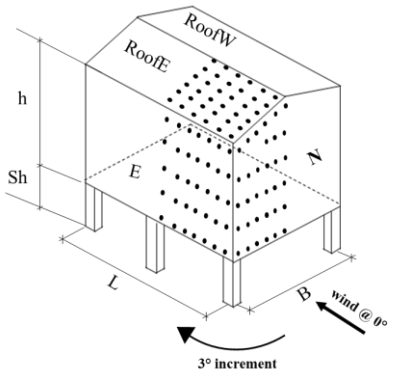

Figure 3.2 3D schematic of the tested model

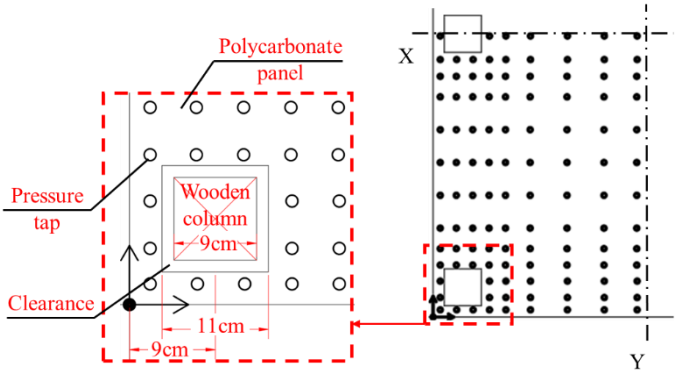

Figure 3.3 Pressure taps distribution on the floor surface

Figure 3.4 shows a sample of the tested models mounted on the turntable at the WOW EF. The materials used to build the model are the same as those used for the experiment explained in chapter two of this dissertation. Table 3.1 lists the eight model cases and their descriptions; 1S is used to describe one-story cases, while 2S describes two-story cases. All the model cases are tested for a wind direction range 0º to 360º with 3º increment.

(a) (b) (c)

Figure 3.4 Different cases of the scaled model inside WOW (a) one-story on-ground case (1S-0), (b) elevated one-story case (1S-73), and (b) elevated two-story case (2S-104)

Table 3.1 Model dimensions of the eight tested models (scale 1:5)

	Case number	Eave height (h)	Stilt height (S_h)
One-story	1S-0	64 cm	0 cm
	1S-43	64 cm	43 cm
	1S-73	64 cm	73 cm
	1S-104	64 cm	104 cm
Two-story	2S-0	110 cm	0 cm
	2S-43	110 cm	43 cm
	2S-73	110 cm	73 cm
	2S-104	110 cm	104 cm

During the test, the WOW fans are adjusted to produce the same mean wind speed reported in chapter two. Cobra probes are installed at different heights, including the mean roof height (MRH) of each tested case (e.g., 75 cm for 1S-0, 117 cm for 1S-43, 148 cm for 1S-73, and 178 cm for 1S-104). As explained in the previous chapter, Cobra probes are used to measure the wind velocity components before placing the model on the turntable with a sampling frequency of 2,500 Hz. The one-story and two-story models are

instrumented with 262 and 307 pressure taps, respectively. Due to the building symmetry, those taps are distributed on one-quarter of the model roof walls and floor. The pressure taps are connected to six Scanivalve ZOC33 pressure scanners using flexible tubes. Pressure data are recorded with a sampling rate of 520 Hz for 60 seconds.

3.2 Data Analysis

The fluctuation of wind speed in the three principal directions is recorded for 180 seconds at the model location. The mean wind speed (U) and the turbulence intensity (I_u) are calculated for each mean roof height (Z). Post testing, a transfer function is applied to the recorded pressure-time history as recommended by Irwin et al. [48]. Eq. 3.1 is used to calculate the pressure coefficients.

$$C_P = \frac{P}{\frac{1}{2}\rho V^2} \tag{3.1}$$

where ρ is the air density, P is the peak differential pressure (the difference between the model surface and the reference pressure), V is the 3-sec gust wind speed at the mean roof height for each stilt case.

As explained in chapter two, the limited test section size impedes forming large eddies with respect to the model size. Figure 3.5 (a-b) illustrate the missing low-frequency part for 2S-0 and 1S-43 cases, respectively. In the plot, the frequency is denoted as n (Hz), the turbulence power spectrum is denoted as S. In both cases, the wind speed is recorded at almost the same height (6 m in full scale). Using Engineering Sciences Data Unit (ESDU), full-scale normalized longitudinal turbulence spectral density is computed for the coastal region. To ensure the accuracy of the estimated peaks, the Partial Turbulence Simulation (PTS) method is used to compensate for missing low-frequency content in the peak

estimation process. Figure 3.6a shows the turbulence intensity (I_u) at the MRH of each case after adding the missing low-frequency turbulence. And Figure 3.6b shows the normalized mean wind speed profile (U/ U_{ref}); where, U_{ref} is the reference mean wind speed at the reference height (Z_{ref} =10m at full scale). The final local peak pressure coefficients are presented in the next section.

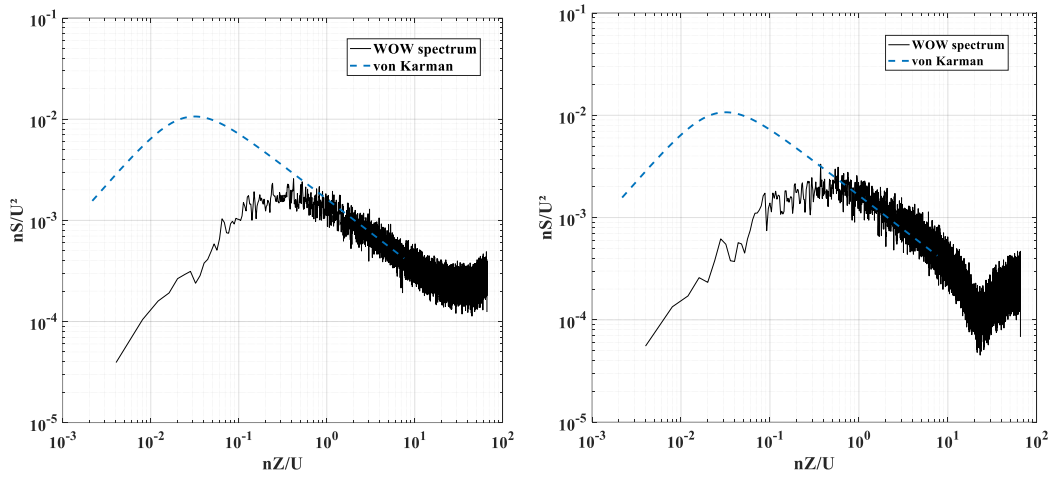

(a) (b)

Figure 3.5 Turbulence power spectra inside WOW compared to von Karman spectrum (a) case 2S-0, and (b) case 1S-43

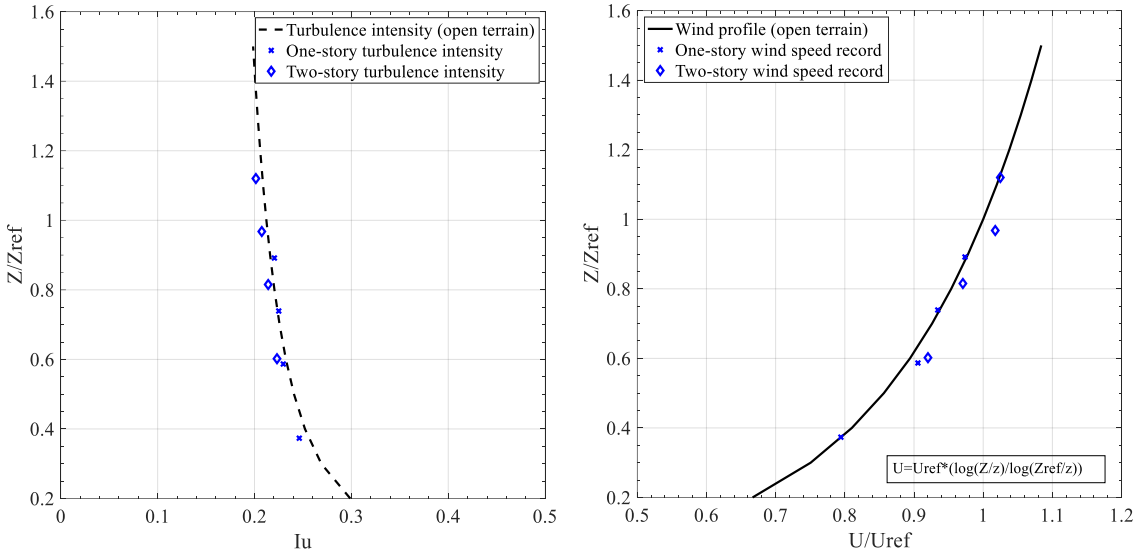

(a) (b)

Figure 3.6 Atmospheric Boundary Layer in WOW compared to full-scale wind profile [49] (a) turbulence intensity, and (b) normalized mean wind speed

3.3 Peak Pressure Coefficients on Roof and Walls

The local peak pressure coefficients are calculated using the 3-second gust wind speed at the model MRH (C_{Ppeak}). The change in the C_{Ppeak} distribution on the wall surfaces can be noticed by comparing on-ground and elevated cases. For instance, a reduction of C_{Ppeak} positive values and an increase in C_{Ppeak} negative values occur at the lower zone of the elevated model walls compared to their on-ground counterparts. By comparing Figure 3.7a with Figure 3.7c, the C_{Ppeak} positive values decrease by 60 % at the lower region, while a blue strip of high negative C_{Ppeak} values appears at the lower end of the walls of the elevated case (1S-104). This is observed as well for the two-story elevated cases (see Figure 3.7d).

On the other hand, the roof surface pressure coefficients did not exhibit significant differences between the tested cases. Roof C_{Ppeak} negative values are higher in the on-ground one-story case and slightly decrease as the elevation increases.

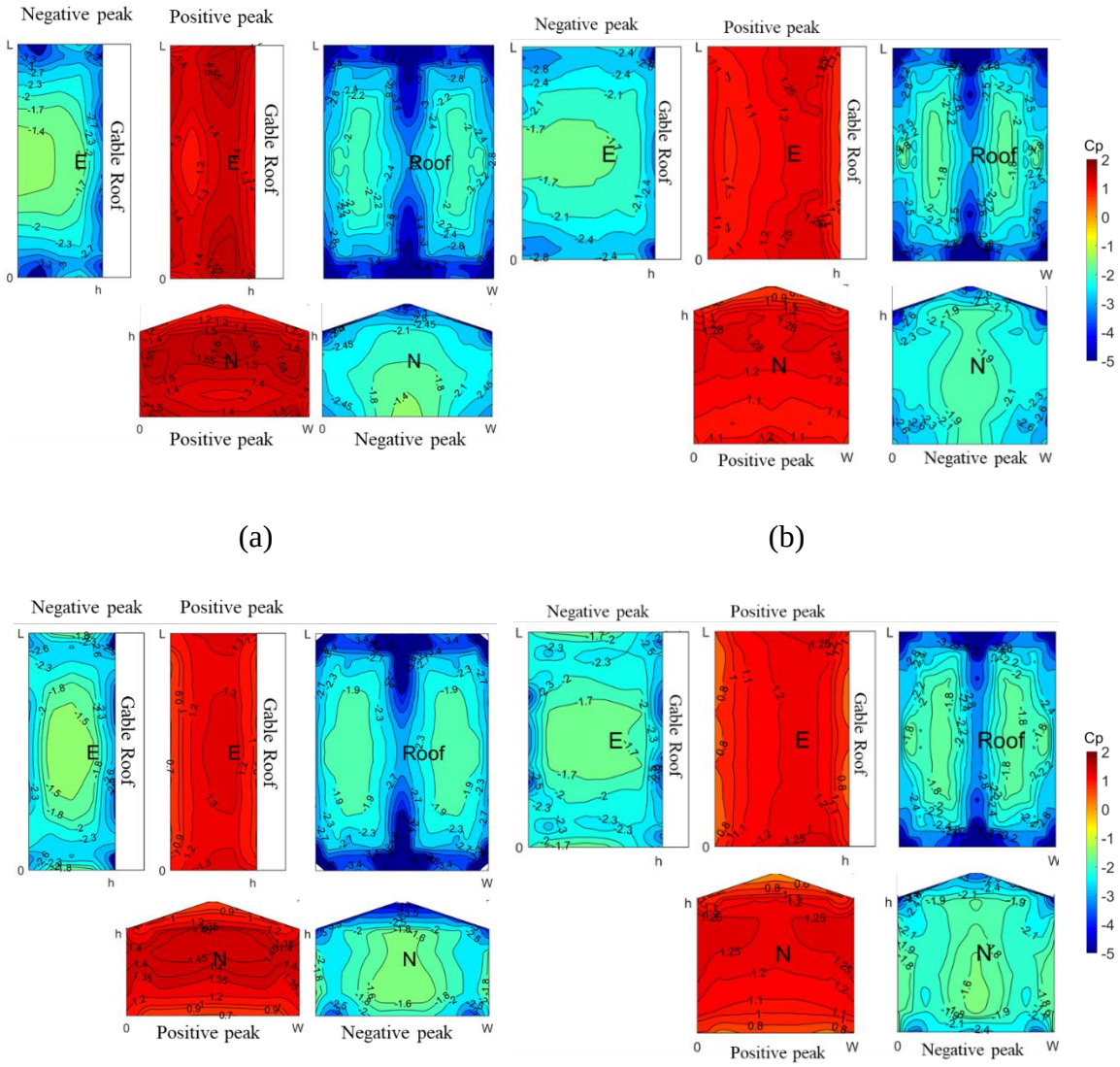

Figure 3.7 Maximum and Minimum local peak pressure coefficients (C_{Ppeak}) among all wind directions (a) case 1S-0, (b) case 2S-0, (c) case 1S-104, and (d) case 2S-104

The peak area-averaged wind pressure coefficients ($C_{P,\ avg,\ peak}$) are analyzed to estimate wind loading on Components and Cladding zones. Using the 3-sec wind speed at the mean roof height (MRH), the procedure of calculating $C_{P,\ avg,\ peak}$ is done by following the recommendations provided by the ASCE 7-16 and explained in detail in chapter two [53]. Figures 3.8 and 3.9 show the zone boundaries for the roof and wall surfaces, respectively.

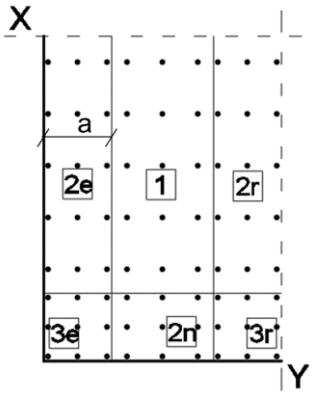

Figure 3.8 Zone boundaries of the roof surface according to ASCE 7-16

Table 2.2 summarizes the resulting $C_{P,\ avg,\ peak}$ for the roof zones obtained for the eight tested models while considering the worst case of all tested wind directions and tributary area 0.9 m^2. The $C_{P,\ avg,\ peak}$ values look consistent with no significant variations. They exhibit a slight tendency to decrease as the stilt height increases. The one-story cases exhibit 10% and 20% higher $C_{P,\ avg,\ peak}$ values compared to two-story cases. Compared to the 1S-0 case, the $C_{P,\ avg,\ peak}$ values of the one-story elevated cases are 5 % lower at the middle zone and 10% lower at the edge zones. While for the 2S-0 case, the $C_{P,\ avg,\ peak}$ values of the elevated cases are 12 % lower at the middle zone and 7% lower at the edge zones. The slight change in the $C_{P,\ avg,\ peak}$ values agrees with the results reported in chapter two. Consequently, the aerodynamics of elevated one- and two-story cases do not significantly affect the suction at the roof surface compared to their on-ground counterparts.

Table 3.2 $C_{P, avg, peak}$ of the roof surface

Test case / *Zone*	*1S-0*	*1S-43*	*1S-73*	*1S-104*	*2S-0*	*2S-43*	*2S-73*	*2S-104*
3e	-2.50	-2.42	-2.41	-2.26	-2.32	-2.09	-2.07	-2.12
3r	-3.02	-2.96	-3.02	-2.97	-2.78	-2.63	-2.67	-2.73
2e	-1.93	-1.78	-1.78	-1.72	-1.85	-1.65	-1.74	-1.68
2r	-2.40	-2.34	-2.23	-2.14	-1.97	-2.00	-1.85	-1.91
2n	-2.46	-2.30	-2.33	-2.26	-2.08	-2.06	-1.94	-2.00
1	-1.81	-1.72	-1.72	-1.68	-1.81	-1.63	-1.58	-1.63

The same procedures are applied on the wall surfaces. Tables 3-4 show the negative and positive $C_{P, avg, peak}$ values corresponding to a tributary area 0.9 m^2 (full scale), representing the envelope of all wind directions. The table shows that both positive and negative averaged coefficients are more critical in the on-ground cases. The positive $C_{P, avg, peak}$ values in the one and two story elevated cases are lower by 20% and 15%, respectively, compared to their on-ground counterparts. Additionally, the two-story cases $C_{P, avg, peak}$ values are 20% lower than one-story cases. The negative $C_{P, avg, peak}$ is not noticeably affected by the elevation in case 1S-43 compared to the on-ground replica. However, in the taller stilt cases (1S-73) and (1S-104), $C_{P, avg, peak}$ values are around 15% lower than the on-ground case. This decrease possibly is due to the larger reference wind velocity for taller buildings.

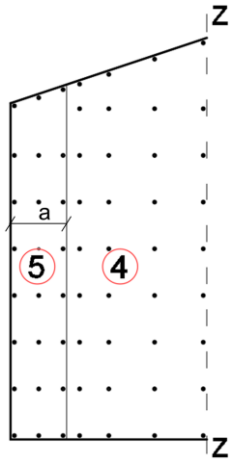

Figure 3.9 Zone boundaries of the two-story wall surface according to ASCE 7-16

Table 3.3 Negative $C_{P, avg, peak}$ values on walls of each stilt model

Test case	*1S-0*	*1S-43*	*1S-73*	*1S-104*	*2S-0*	*2S-43*	*2S-73*	*2S-104*
Zone name	*Peak negative pressure coefficient ($C_{P, avg, peak}$)*							
4	-1.76	-1.73	-1.50	-1.48	-1.72	-1.57	-1.50	-1.56
5	-2.22	-1.93	-1.95	-1.88	-1.84	-1.64	-1.55	-1.64

Table 3.4 Positive $C_{P, avg, peak}$ values on walls of each stilt model

Test case	*1S-0*	*1S-43*	*1S-73*	*1S-104*	*2S-0*	*2S-43*	*2S-73*	*2S-104*
Zone name	*Peak positive pressure coefficient ($C_{P, avg, peak}$)*							
4	1.24	1.03	1.01	0.98	0.97	0.86	0.81	0.83
5	1.25	1.08	1.07	1.04	1.00	0.91	0.85	0.92

The presented results indicate that a simple conservative approach would be to use the on-ground pressure coefficients to design roofs and walls of elevated cases. This agrees with the recommendations provided by the Australian and New Zealand wind loading standard [39], which provides the same pressure coefficient value for an elevated house's walls as for the on-ground case. The AS/NZS 1170.2 standard provides averaged pressure coefficient values (0.8 & -0.6) for the floor underside regardless of its dimensions [39]. Also, no advice is currently available in the ASCE 7-16 standard on elevated buildings. The following section presents the resulting pressure coefficients and wind forces for the tested cases. The wind effect on the floor surface is presented and compared with the roof surface wind loading results.

3.4 Floor Surface Zoning Scheme and Proposed Pressure Coefficients

This section provides floor local peak coefficients and a scheme for pressure distribution zoning. Based on the proposed zoning scheme, the area-averaged pressure coefficients for different effective areas are presented. In addition, the analyzed data from the current wind tests are compared with available design provisions for flat roof surfaces of low-rise buildings in ASCE 7-16 [36].

3.4.1 Local peak pressure coefficients on the floor surface

Figure 3.10 (a-c) shows the peak local pressure coefficient values for the one-story elevated cases among all wind directions. The pressure coefficients are calculated by taking the reference velocity at the MRH. The figure shows high suction regions observed along the floor edges. Using the mean roof height as a reference height to calculate the pressure coefficient on the floor could be misleading to present the effect of changing the model stilt height, especially for the multi-stories low-rise buildings. This is particularly important when looking at the effect of one-story vs. two-story cases. Alternatively, it could be more reasonable to use the floor height as the reference height. Thus, compared with Figure 3.10 (d-f), which presents the normalized pressures using floor height velocity as a reference, Figure 3.10 (a-c) shows smaller coefficients. In addition, Figure 3.10 (a-c) indicates slight differences in the pressure coefficients without a noticeable trend as the stilt height increases. In contrast, Figure 3.10 (d-f) shows a more consistent trend in the resulting pressure coefficients on the floor for the tested elevated cases. For this reason, C_{Ppeak} normalized using reference wind velocity at the floor surface is used to determine the

zoning scheme for the floor surface. More discussion on these observations is provided in the next section.

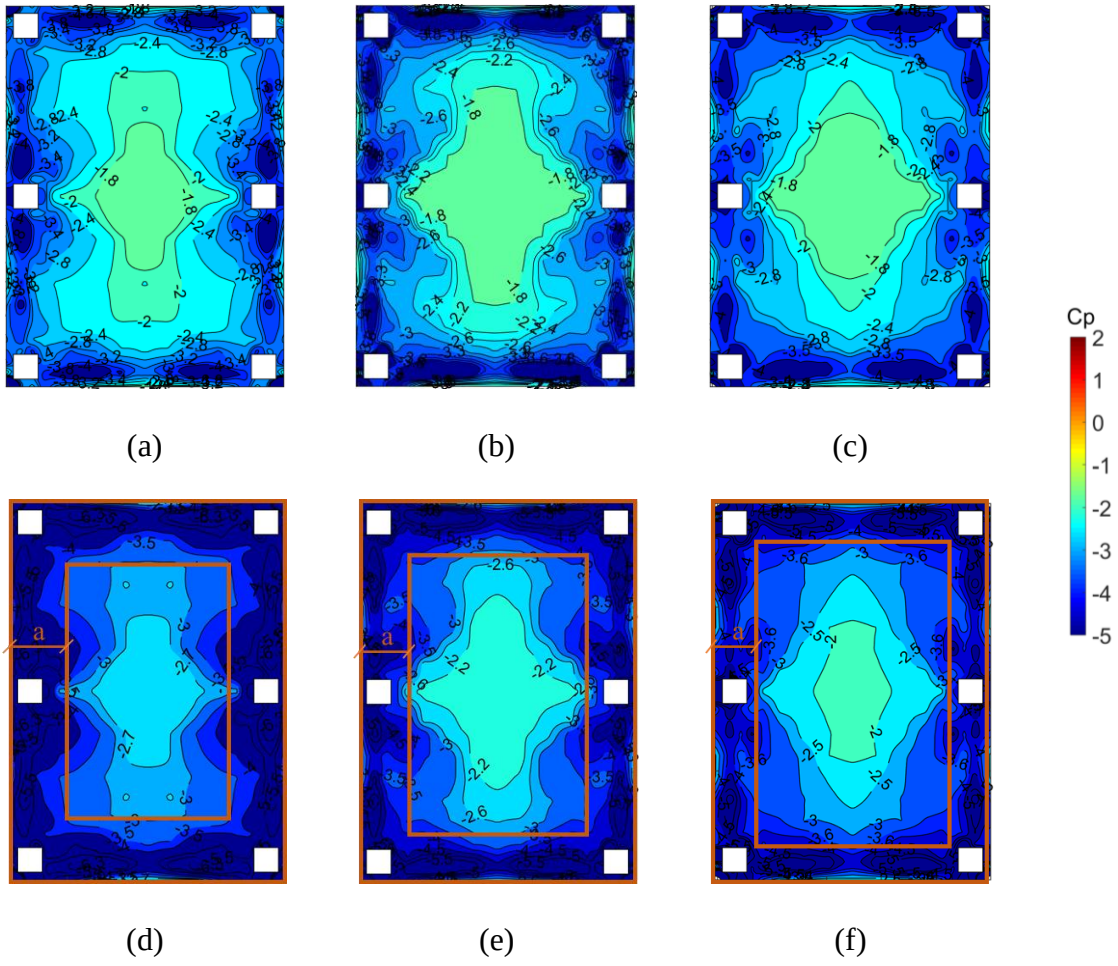

Figure 3.10 Minimum C_{Ppeak} contours on the floor surface among all wind directions (a) case 1S-43 using reference velocity at MRH, (b) case 1S-73 using reference velocity at MRH, (c) case 1S-104 using reference velocity at MRH, (d) case 1S-43 using reference velocity at floor level, (e) case 1S-73 using reference velocity at floor level, and (f) case 1S-104 using reference velocity at floor level.

3.4.2 Floor zoning scheme and area-averaged pressure coefficients

Figures 3.10 (d-f) and 3.11 (a-c) show the C_{Ppeak} contour plot for one-story and two-story elevated cases. The reference velocity is taken at the floor level, as stated in the previous

section. A slight reduction in the width of the high suction region occurs as the stilt height increases for both one-story and two-story cases. However, the one-story case exhibits higher pressure coefficient values compared to the two-story one. In the smallest stilt case (1S-43), the C_{Ppeak} ranges between -6.3 and -3.5 along the edges and reaches -2.7 at the middle region. In case 2S-43, the C_{Ppeak} range at the edge is between -5.5 and -3.3. The C_{Ppeak} values, normalized using dynamic pressure at the floor level, are used to obtain a zoning scheme for the floor surface. In chapter two, the author suggested dividing the floor surface into three zones: column, edge, and middle zones [22]. However, adding intermediate columns in this study caused an additional suction along the floor edge. Therefore, it is recommended to merge the edge and column zones into one zone. Consequently, the floor surface is divided into two zones. More investigations are needed for different column patterns.

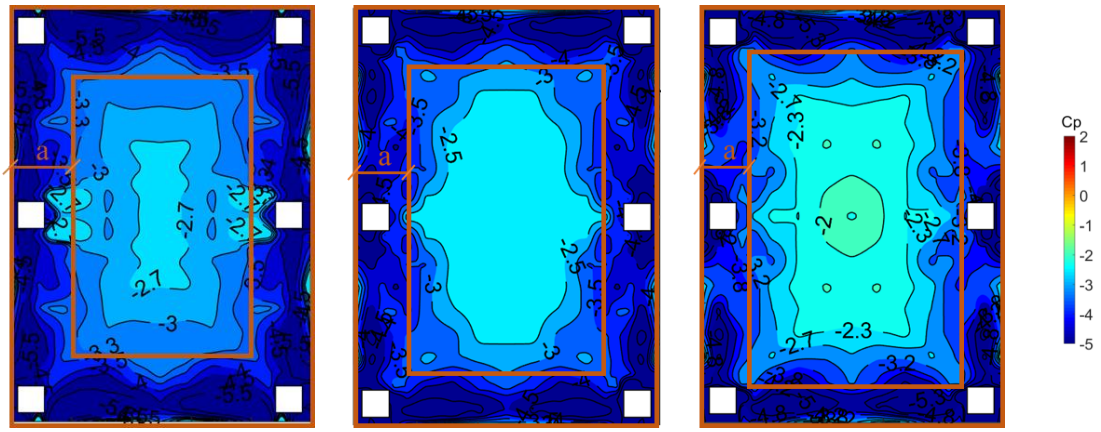

(a) (b) (c)

Figure 3.11 Minimum C_{Ppeak} contours on the floor surface among all wind directions using reference velocity at floor level (a) case 2S-43, (b) case 2S-73, and (c) case 2S-104.

Figure 3.12a demonstrates the proposed zones for similar floor surfaces: middle zone (1), and edge zone (2). This zoning scheme is similar to the one provided by the ASCE 7-16 standard for a flat roof. For each zone, the area average pressure coefficients ($C_{P,\ avg,\ peak}$) are calculated for different tributary areas and plotted in Figures 3.13 and 3.14. The width of zone 2 is a variable named "a" which is empirically estimated using Equation (3.2). This equation is recommended to be used under two conditions: (1) the column width "c" shall not be less than $S_h/10$, and (2) the zone width "a" shall not be less than 2c. As the relationship between the stilt height and zone width "a" is consistent in the one-story and two-story cases, the author suggests using the same equation for different numbers of stories.

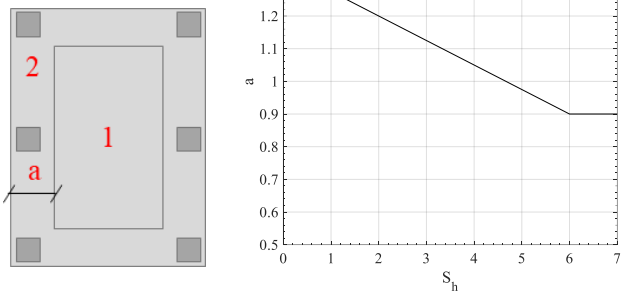

(a) (b)

Figure 3.12 Proposed zone boundaries of the floor surface; (a) zone labeling, and (b) zone width relation with the stilt height

$$a = 3c - \frac{3S_h}{40} \tag{3.2}$$

where S_h is the floor height, and c is the column width.

For the current case, the column dimension is fixed (0.45m square section in full scale), the relation between the zone width and the stilt height is drawn (Figure 3.12b). The graph reveals an inverse relationship between the two variables, for any given (c). The reduction of the zone width is linear until it reaches twice the stilt width (0.9m in full scale), and it remains constant after that.

Figure 3.13 shows the variation of $C_{P, avg, peak}$ with the corresponding effective tributary areas for zone 1. The plots show the resulting $C_{P, avg, peak}$ normalized using dynamic velocity at (1) the mean roof height (WOW (MRH)) and (2) the Floor level (WOW (Fl)). The plots also include the logarithmic relation between the external pressure coefficient and cladding effective area on a flat roof surface according to ASCE 7-16. To easily compare the floor pressure coefficients with these recommended for a flat roof provided by ASCE 7-16, the Logarithmic best fit (LBF) line is computed for the WOW data. The figure facilitates the evaluation of wind loading using different velocity reference heights. For the one-story cases, Figure 3.13 (a-c), the $C_{P, avg, peak}$ normalized using MRH velocity are close or lower than the ASCE external pressure coefficients for a flat roof. This is also observed in the two-story cases (Figure 3.13 (d-f)). This indicates that using the pressure coefficients of a flat roof surface to calculate wind forces on elevated building floor surface is conservative if the reference wind velocity is taken to be at the mean roof height. However, using the wind velocity at the floor surface, the recommended pressure coefficient for zone 1 ranges between -2.7 and -1.5 for tributary areas ranging between $0.9m^2$ to $46.5m^2$(full scale), respectively.

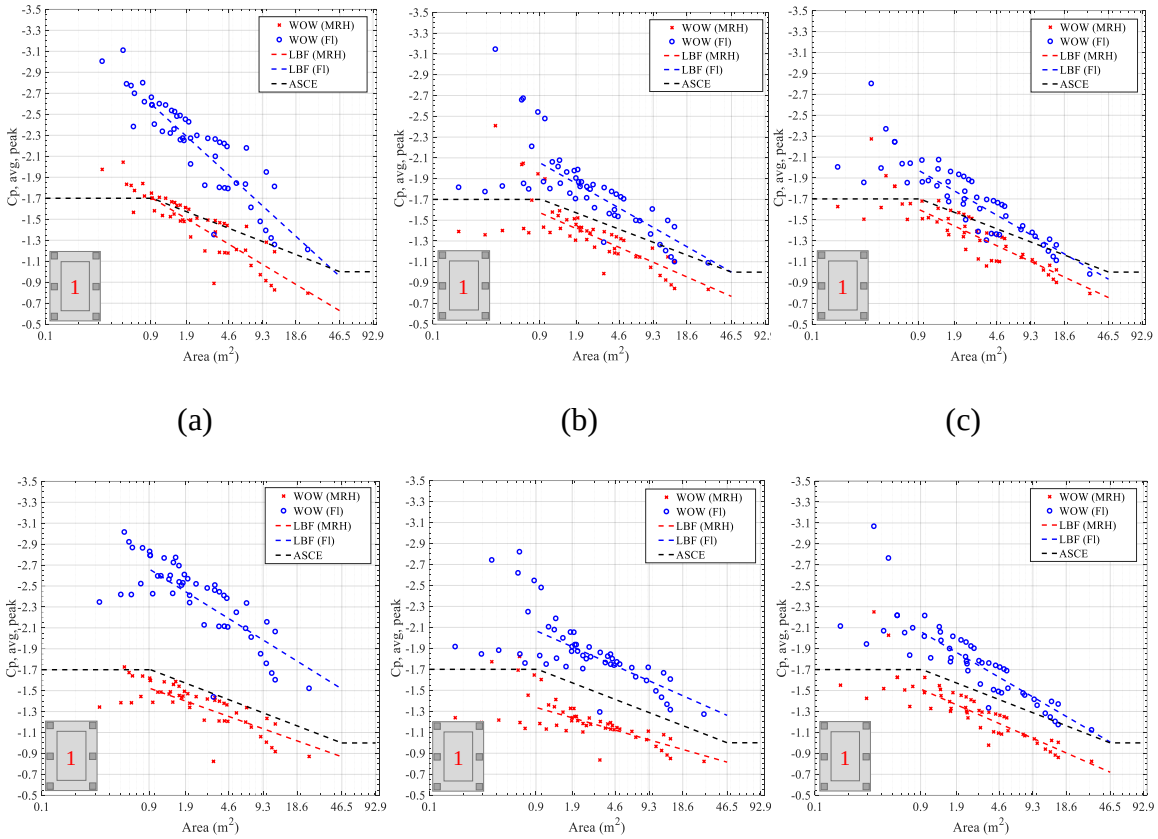

Figure 3.13 $C_{P,\ avg,\ peak}$ for the middle zone 1 for different effective tributary areas (a) case 1S-43, (b) case 1S-73, (c) case 1S-104, (d) case 2S-43, (e) case 2S-73, and (f) case 2S-104.

For the edge zone (2), the same observations are noticed in Figure 3.14 (a-f). The ASCE $C_{P,\ avg,\ peak}$ values for a flat roof are much more conservative compared to the WOW (MRH) values. Therefore, the ASCE values can be conservatively used to calculate vertical forces on the floor surface while using the reference wind velocity at the mean roof height. Otherwise, the $C_{P,\ avg,\ peak}$ on the floor surface can be estimated using a logarithmic relation of $C_{P,\ avg,\ peak}$ ranging between -3.1 and -1.7 for tributary areas ranging between 0.9m^2 to 46.5m^2(full scale), respectively. The ASCE 7-16 standard recommends using external pressure coefficients -0.9 and -0.6 for the edge zone and the middle zone of the elevated

tanks. From the results shown, it is clear that both values are not applicable to be used in case of elevated houses.

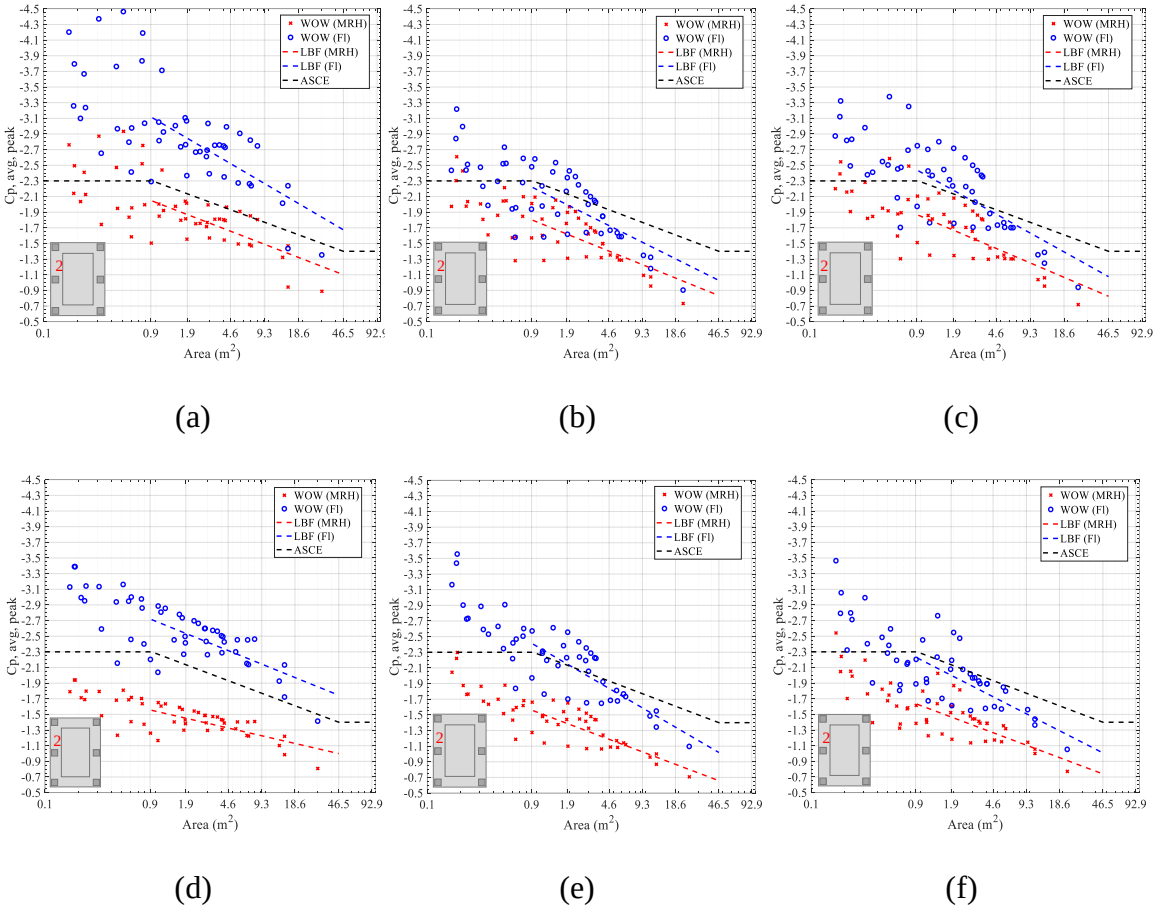

Figure 3.14 $C_{P,\ avg,\ peak}$ for the edge zone 2 for different effective tributary areas: (a) case 1S-43, (b) case 1S-73, (c) case 1S-104, (d) case 2S-43, (e) case 2S-73, and (f) case 2S-104

In the current study, the mean pressure coefficients ($C_{P,\ mean}$) are also averaged over the whole floor surface to get $C_{P,avg,\ mean}$. Because only the quarter is instrumented, only the mean coefficients are calculated as it could be derived using the model symmetry. Table 3.5 lists the resulting $C_{P,avg,\ mean}$ values on the floor surface for the critical case 90º wind direction. For the current tested cases, the external pressure coefficients are calculated using the AS/NZS 1170.2 standard to compare the recommended external coefficients by

AS/NZS 1170.2 standard against real conditions. The recommended negative external pressure coefficient over the floor surface is -0.6, which is 8 % to 45 % lower than WOW (Fl) $C_{P,avg,\ mean}$ value. It's worth mentioning that the pressure coefficients provided by the standard should cover peak values as well. Therefore, further investigation should be done to provide external pressure coefficients for the floor surface.

Table 3.5 Negative $C_{P,\ avg,\ mean}$ values on the floor of all the tested cases

No. of stories	*One-Story*			*Two-Story*		
Stilt case	*1S-43*	*1S-73*	*1S-104*	*2S-43*	*2S-73*	*2S-104*
WOW (Fl)	-0.98	-0.78	-0.73	-1.1	-0.92	-0.8

More studies are required on different configurations of elevated houses with various distributions of stilts to codify external pressure coefficients for the floor surface. Until then, the author recommends using the wind velocity at the building roof height to calculate the wind loads on the floor surface.

3.5 Mean Wind Forces on the Model Surfaces and the Expected Effects

It is of interest to investigate the total wind forces acting on the building surfaces to provide an insight into the overturning moment and base shears acting on the building. For each surface of the tested models, the mean wind force is calculated for every wind direction and normalized to the corresponding wind force for the counterpart on-ground case. Only for the floor surface, the wind force is normalized to the roof wind force multiplied by -1. Figure 3.15 (a-b) shows the variation of the normalized wind forces (F_n) with the stilt height (in full scale) for all surfaces. In general, the figure shows that elevated buildings experience higher forces compared to those imposed on an on-ground counterpart. For the roof surface, the plot is for the critical wind direction (60º) which

shows the highest suction. The plots show a gradual increase in the roof suction force till it reaches 29% and 21% in the one-story and two-story cases, respectively. However, there is no certain trend for the windward wall positive force, under the critical wind direction (0º); the increase is significant in the one-story case, unlike the two-story case. Figure 3.15 (a-b) also shows that the sidewalls' maximum suction force, for the wind direction (0º), occurs in the shortest stilt cases (1S-43) and (2S-43).

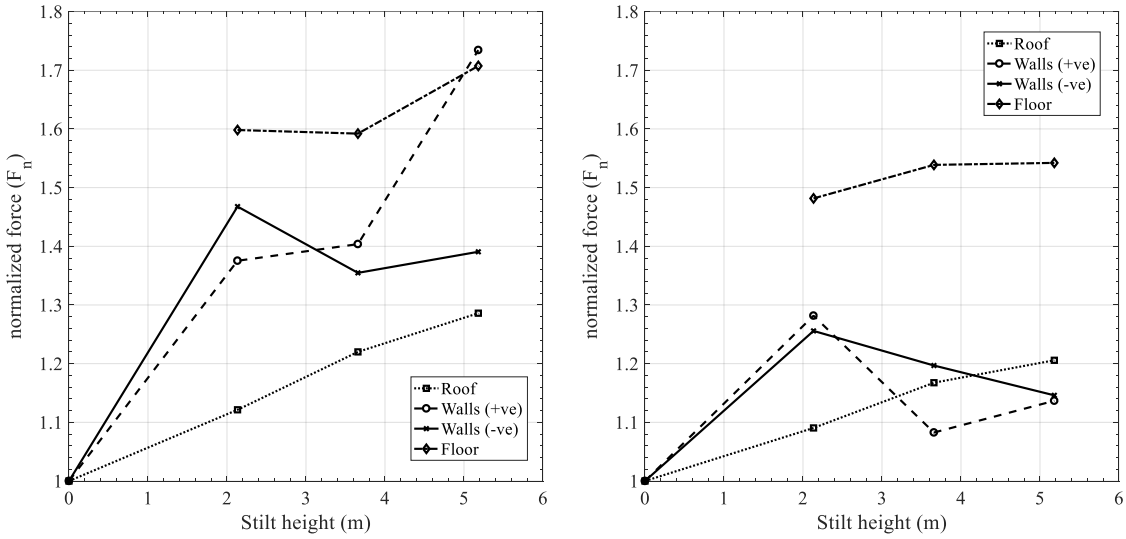

Figure 3.15 Normalized mean wind forces on each surface (a) one-story, and (b) two-story

For the floor, the critical wind case is found to be 90º. Figure 3.15 reveals that the vertical force, acting on the floor downward, shows more significant increase than the roof suction force. For the one-story case, the increase is 60% for the 1S-43 and 1S-73 cases and 70% for the 1S-104 case. On the other hand, in the two-story case, the increase is 48% for the 2S-43 case and around 54% for the 2S-73 and 2S-104 cases. The percentage is lower

in the two-story case because the force acting on the roof is more significant due to the increased wind speed at larger heights. In conclusion, the stilt height significantly affects the resulting total vertical, shear force, and overturning moment acting on the house foundations.

3.6 Conclusion

An experimental investigation of wind effects on elevated houses is conducted. This study considers two building types: (1) One-story and (2) Two-story gable roof models. Local peak pressure coefficients (C_{Ppeak}), calculated using the experimental pressure time histories, are used to present contour plots along each surface for the on-ground and elevated building cases. Compared to their on-ground counterparts, the following observations are found for the elevated buildings: (1) No significant change is observed in C_{Ppeak} values of the roof surface for the elevated cases; (2) The wall surfaces of the elevated cases experienced lower positive and higher negative C_{Ppeak} at the lower edge due to the flow separation; (3) High suction regions along the floor underside edges and around the stilts are observed. These observations agree well with chapter two findings.

For the floor underside surface, the resulting pressure coefficients show that shorter stilts cases sustain more suction force than taller stilts cases. From the variation of the peak pressure coefficient on the floor underside surface, a zoning scheme is proposed. The proposed zoning scheme adopts an empirical equation that incorporates the column's width and stilt height to calculate the width of the high suction edge zone. Based on the suggested zoning, the area-averaged pressure coefficients are calculated for the floor underside and compared to flat roof external coefficients available in the ASCE 7-16 standard. This comparison shows the applicability of using the pressure coefficients provided by ASCE

7-16 for a flat roof to calculate wind forces on the floor underside surface of an elevated house where the reference wind velocity is taken at the mean roof height of the elevated house building. Otherwise, higher pressure coefficients should be used if the floor level is considered at the reference height.

The experimental results show a considerable increase in the overall (global) uplift force on the roof surface and on the floor underside, especially in the one-story elevated cases, as the stilt height increases. As with any experimental investigation, the current results are obtained on a limited number of building configurations. It would be useful in the future to examine other building shapes and stilt arrangements as well as the effects of partially blocking the underneath of the building.

The following chapters present the usage of numerical analysis to examine different configuration variables. They provide a visualization of the flow streamlines and characteristics. The numerical study also investigates the resulting global wind loads on the house foundations.

4. CHAPTER IV

PARAMETRIC NUMERICAL STUDY TO EVALUATE MEAN WIND LOADS ON ELEVATED HOUSES

In this chapter, various configurations of elevated houses are numerically simulated to study the wind flow through the building and present the resulting wind pressures and forces. Computational Fluid Dynamics (CFD) method is adopted to perform the numerical simulations in this dissertation. The CFD analysis is a numerical approach used to simulate the air flow around bluff bodies by applying the equations of fluid motion at discrete points through the studied fluid field. The CFD numerical analysis has been successfully used in a wide range of applications in the wind engineering field. Compared to experimental wind tunnel tests, CFD simulations provide dense output data to describe the flow characteristics and the resulting wind loads. CFD is also distinguished by its ability to simulate different flow turbulence characteristics, atmospheric boundary layer profiles, and various building geometries at a low cost compared to conventional wind tunnel testing [40]. To successfully reproduce a wind tunnel test using CFD simulations, it is essential to accurately define the appropriate domain and mesh size, boundary conditions, and discretization methods. However, the computational cost factor is also critical because the most precise CFD modeling (e.g., Direct Analysis) could take years to be developed and analyzed. Several studies in literature discuss the effect of those parameters and how to choose the model size to provide accurate results at a reasonable computational cost [54]–[60].

This chapter presents a simulation of a full-scale (prototype) size of the on-ground and elevated houses tested at the Wall of Wind facility and reported earlier in this dissertation

using a steady-state Reynolds Averaged Navier Stokes (RANS) model. The RANS simulation is widely used to study the aerodynamics of low-rise buildings. Tominaga et al. used RANS model to test the wind effect on low-rise buildings with different roof angles. The authors were able to get a good agreement for the mean wind pressure compared to the model tested at a wind tunnel. The simulation of RANS model allowed the author to study the mean wind speed and mean pressure coeffcients near the model and over the flow field.

Amini et al. [34] conducted a parametric numerical study using RANS model to evaluate the effect of elevating the structure on the resulting mean pressure coefficients using Computational Fluid Dynamics (CFD) simulations [34]. The study utilized the experimental results reported by Holmes [24] to validate their CFD model to further investigate other elevation heights and the wind flow characteristics. The results showed the efficiency of the RANS model to present mean pressure coefficients. After simulating an on-ground case and two different stilt heights, Amini et al. [34] presented velocity streamlines and investigated the height effect on the uplift force and overturning.

Therefore, RANS model is chosen for the current numerical study to represent mean wind actions on elevated buildings. This simulation enables the understanding of elevated building aerodynamics, the change in mean pressures along the model surfaces, and attempts to understand the damage modes observed in recent hurricanes. The wind flow characteristics are investigated for different cases, and the resulting mean wind pressure is reported [63].

The chapter starts with a validation study comparing the mean pressure coefficients calculated using RANS modeling and the ones resulting from the experimental study.

Then, a parametric study is conducted with the following objectives: (1) investigate the characteristics of wind flow surrounding the building for various geometrical configurations, and (2) assess wind actions on elevated structures and their variations with the variation of the building stilt height and floor aspect ratio. This study aims at identifying the geometrical controlling parameters and, therefore, facilitate the codification of the results. In addition, the CFD study enables the identification of the most critical configurations and geometrical range for future experimental studies.

4.1 CFD Model Description

The model used in this simulation is the prototype dimensions of the elevated houses tested in the experimental program. Figure 4.1 shows a schematic of the simulated model and the coordinate system used in the numerical analysis. First, a validation study is conducted on the 2.15m elevated two-story model discussed in chapter three. The full-scale model is 8.76 m long and 6.4 m wide with a gable roof angle of 18º. The CFD simulation is performed for three wind directions; 0º, 45º, and 90º (i.e., 0º wind flow at Y-dir. and 90º wind flow at X-dir.). Next, the same data setup and boundary conditions are used to perform the parametric study to assess the relationship of the resulting wind load with the variation of the model stilt height and the floor aspect ratio. The study plan is summarized in Table 4.1. The stilt heights considered in this study range between 0 m and 5.2m stilts with 0.6m increment, and the floor aspect ratio ranges between 1 and 2.5 with 0.25 increment.

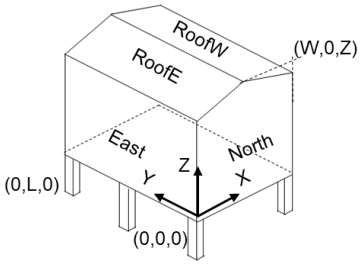

Figure 4.1 Full-scale elevated house schematic and the global axis

Table 4.1 Parametric study variables

One-story and Two-story elevated house																	
Different stilt heights											Different floor aspect ratio						
Floor aspect ratio	1.36										1	1.36	1.5	1.75	2	2.25	2.5
Stilt height (m) / Wind Direction	0.6	1.2	1.8	2.1	2.4	3	3.6	4.2	4.8	5.2	2.1 m						
Zero	*	*	*	* *	*	*	*	*	*	*	*	*	*	*	*	*	*
45	*	*	*	* *	*	*	*	*	*	*	*	*	*	*	*	*	*
90	*	*	*	* *	*	*	*	*	*	*	*	*	*	*	*	*	*
* Without Stairs											* * With Stairs						

The 1S and 2S symbols refer to the one-story and two-story cases, respectively. The stilt height in meters is added in numbers after the used symbol (i.e., 1S-5.2 for the one-story model elevated by 5.2m).

4.2 Governing Equations

As mentioned in the introduction, CFD methods adopt fundamental fluid equations to describe the air movement through the domain. These fundamentals are; (1) The mass conservation law, (2) The force acting on anybody is the product of mass and acceleration (Newton's second law), and (3) The energy conservation law. The simplified form of continuity and momentum equations are shown in equation Equations (4.1 and 4.2), for a

fluid velocity, pressure, location, and dynamic viscosity variables donated by u, p, x, and μ, respectively.

$$\frac{\partial u_i}{\partial x_i} = 0 \tag{4.1}$$

$$\rho\left(\frac{\partial(u_j)}{\partial x_j}\right) = -\frac{\partial P}{\partial x_i} + \mu\frac{\partial}{\partial x_j}\left(\frac{\partial u_i}{\partial x_j}\right) \tag{4.2}$$

To perform an accurate simulation, all the air properties, speed, friction, and volume forces should be defined precisely. The continuity, energy, and momentum equations are then embedded in the Navier Stokes equations and solved at the three dimensions based on the finite volume approach. The general form of the Navier-Stokes (NS) equations for incompressible flow is as shown in Equation (4.3) [64].

$$\rho\left(\frac{\partial u_i}{\partial t} + \frac{\partial(u_i u_j)}{\partial x_j}\right) = -\frac{\partial P}{\partial x_i} + \mu\frac{\partial}{\partial x_j}\left(\frac{\partial u_i}{\partial x_j} + \frac{\partial u_j}{\partial x_i}\right) + f_i \tag{4.3}$$

where body force is donated by the symbol f_i, t is time, and ρ is constant.

The difficulty of solving the flow equation is due to the second nonlinear term on the left side, which describes heat transfer through a fluid. The first term on the left side is the instantaneous acceleration. On the right side, the first term is for the pressure gradient, and the second one is the viscous dissipation which stabilizes the simulation. Equation (4.4) divides the instantaneous velocity into two parts; the mean velocity ($\bar{u}$) and the fluctuating part (u'_i). Equation (4.5) is substituted into the NS equation to incorporate the turbulence occurring in the wind flow.

$$u_i = \bar{u} + u'_i \tag{4.4}$$

Various fluctuating flow parameters can be averaged based on the averaging concepts proposed by Reynolds. This can be accomplished using RANS equation to help in reducing

the computational cost. RANS simulation calculates the mean values separately from the fluctuating variables by solving supplementary equations of turbulence statistics. This simulation has been proven to work efficiently only if used to calculate mean or RMS values of the flow quantities [65], [66]. It requires coarse mesh to transport large eddies.

$$\rho\left(\frac{\partial u_i}{\partial t}+\frac{\partial(u_i u_j)}{\partial x_j}\right)=-\frac{\partial P}{\partial x_i}+\frac{\partial}{\partial x_j}\left(\mu\left(\frac{\partial u_i}{\partial x_j}+\frac{\partial u_j}{\partial x_i}\right)-u'_i u'_j\right)+f_i \tag{4.5}$$

The turbulent model named RNG k-ε is used to perform the current simulation where, k is the turbulent kinetic energy, and ε is the turbulent dissipation rate. The RNG model which transports Equations (4.6 and 4.7) has been formed by using a mathematical technique called "renormalization group" (RNG) methods. Also, the simulation is performed as a steady-state, which averages the flow over time. This method has been explained in detail by Yakhot et al. [67].

$$\rho\left(\frac{\partial k}{\partial t}+\frac{\partial(k u_i)}{\partial x_i}\right)=\frac{\partial}{\partial x_j}\left(\alpha_k \mu_{eff}\frac{\partial k}{\partial x_j}\right)+G_k-\rho\varepsilon \tag{4.6}$$

$$\rho\left(\frac{\partial \varepsilon}{\partial t}+\frac{\partial(\varepsilon u_i)}{\partial x_i}\right)=\frac{\partial}{\partial x_j}\left(\alpha_\varepsilon \mu_{eff}\frac{\partial \varepsilon}{\partial x_j}\right)+C_{1\varepsilon}\frac{\varepsilon}{k}(G_k)-C_{2\varepsilon}\rho\frac{\varepsilon^2}{k}-R_\varepsilon \tag{4.7}$$

where, G_k is the generation of turbulent kinetic energy due to mean velocity gradients. μ_{eff} is the effective viscosity. $C_{1\varepsilon} = 1.42$, $C_{2\varepsilon} = 1.68$, and $C_\mu = 0.0845$. And for the current case, the inverse effective Prandtl numbers for k and ε are $\alpha_k = \alpha_\varepsilon \approx 1.393$. R_ε takes into account the effects of rapid strain in complex turbulent flows and is calculated using Equation (4.8).

$$R_\varepsilon=\left(\frac{C_\mu \eta^3\left(1-\frac{\eta}{\eta_0}\right)}{1+\beta\eta^3}\right)\frac{\rho\varepsilon^2}{k} \tag{4.8}$$

$\eta = S_k/\varepsilon$, and $\eta_0 = 4.38$

4.3 Computational Domain and Mesh Criteria

As recommended by Franke et al. [68], the domain dimensions are chosen to avoid any external effect through the domain walls. The distance between the tested model and the inlet should be less than 6H, where H is the total height of the building. As shown in Figure 4.2, this distance is taken as 5H, which is equivalent to the turntable location from the flow management box in the WOW EF. The height of the computational domain is considered to be 7H which takes the stilt height into account. The length behind the building till the outlet is taken to be 15H. The adopted dimensions allow the blockage to be less than 5% so it does not affect the test results [69].

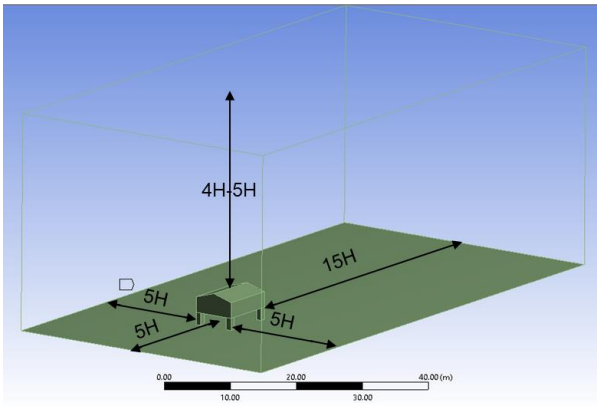

Figure 4.2 Full-scale single-story elevated house inside the wind flow domain and domain meshing.

The computational domain is meshed into tetrahedral cells. Mesh sensitivity analysis is conducted using the 1S-2.1 case, between coarse mesh (~1.7 M cells), moderate mesh (~3.3M cells), and fine mesh (~4.6M cells). The moderate mesh shows good performance and agreement with the experimental results. However, the fine mesh is chosen to precisely simulate the flow separation, reattachment, and vortices, as shown in Figure 4.3. For the large stilt cases, the number of mesh cells exceeds 5 million cells. In the chosen mesh size,

the cell size near the model walls is H/48 and the rate of mesh size increase does not exceed 20%. Mesh refinements are applied around the stilts to precisely monitor the flow separation. At the vertical direction, the first cell height is around 3.2 mm to keep the dimensionless wall distance (Y+) in the range (30-300) to model the log-law layer [70].

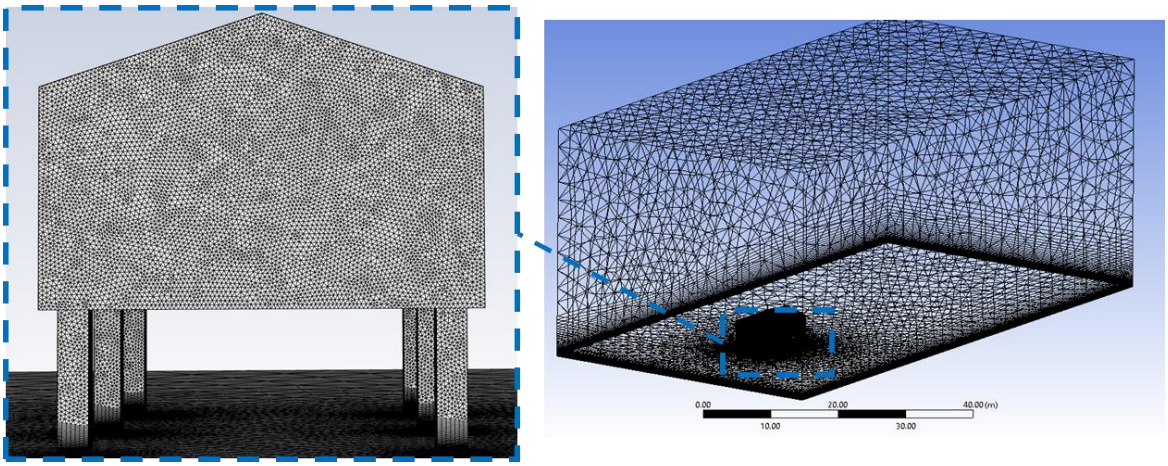

Figure 4.3 3D and frontal view of the simulated 1S-2.1 CFD model mesh using Ansys fluent

4.4 Boundary Conditions and Solver Settings

ANSYS FLUENT 19.0 commercial software is used. All the boundary conditions should be chosen carefully to describe the open terrain ABL and its characteristics. At the upwind boundary, the wind profile logarithmic law is used to define the mean wind velocity U change with height z, which is equivalent to the experimental study as well. Using the appropriate friction velocity (u^*), von Karman constant (κ=0.4), and roughness length (z_0 =0.08m), same as for WOW conditions, the mean win velocity U is defined using Equation (4.9). Figure 4.4 shows the wind profile at the model location of the computational simulation compared to the recorded mean wind speed at WOW EF. U_{ref} is the mean wind speed at the reference height (Z_{ref}), 10m in Full-scale and 2m in WOW.

$$U(z) = \frac{u^*}{\kappa} \ln \frac{z+z_0}{z_0} \tag{4.9}$$

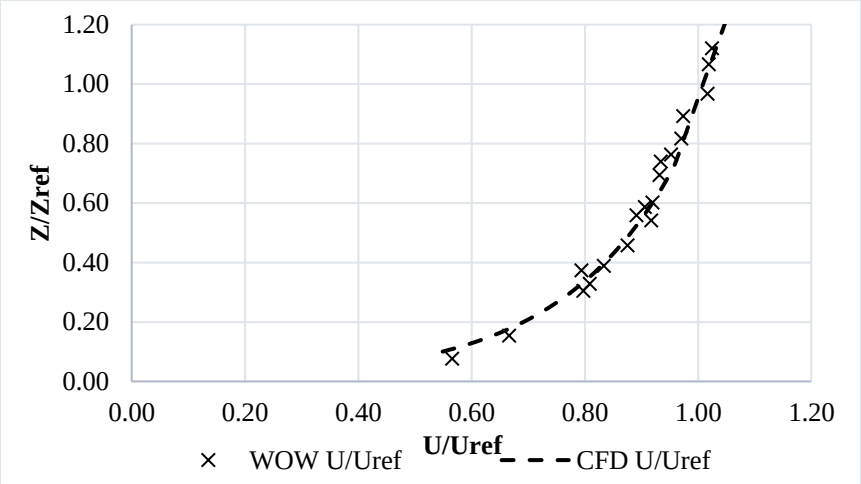

Figure 4.4 Wind flow ABL of the numerical and experimental flow

Both RANS (k-ε) and (k-ω) turbulent models successfully simulate wind effects on low-rise gable roof buildings [34], [61], [62], where ω is the specific dissipation rate. The (k-ε) RNG turbulent model is chosen for this study as it shows better performance [65], [66]. In addition, after comparing the resulting C_{pmean}, along the ridgeline of the roof surface, of (k-ε) and (k-ω), the RNG (k-ε) agreement with WOW is more acceptable, especially in the high suction region, as shown in Figure 4.5. In the figure, SST stands for the shear stress transport formulation.

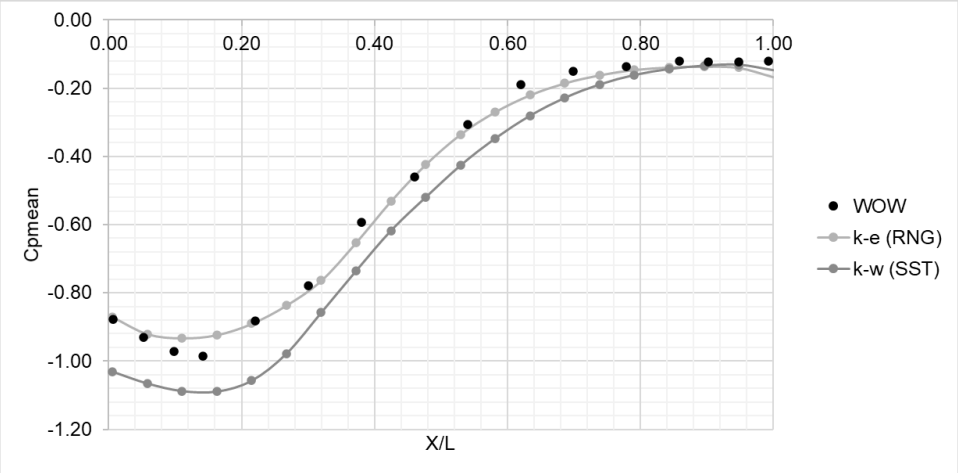

Figure 4.5 C_{pmean} comparison (k-ε) RNG and (k-ω) SST with WOW for the roof surface of 1S-2.1 case under 0º wind direction

The turbulent kinetic energy defines the wind turbulence (I_u) using Equation (4.10 and 4.11), where Cμ is the turbulence model constant and taken as 0.09 [71]. The turbulent dissipation rate is calculated using equation (4.12) as recommended by [72]

$$K(z) = \frac{u_*^2}{\sqrt{C_\mu}} \tag{4.10}$$

$$K(z) = \frac{(Iu\ U)^2}{2} \tag{4.11}$$

$$\varepsilon(z) = \frac{u_*^3}{\kappa(z+z_0)} \tag{4.12}$$

All the outer walls are defined as slip walls, and the ground surface is defined as a rough wall using the same roughness length as the prototype (z_0=0.08m). The roughness length is defined using input values; roughness height (C_s), roughness constant (K_s=0.5), and calculated using Equation (4.13) [54]. The used parameters for the numerical simulation are explained in this section and summarized in Table 4.1.

$$C_s = \frac{9.793\ z_0}{K_s} \tag{4.13}$$

Table 4.2 Numerical simulation parameters

Property	Setting
Solver	Pressure Based Steady
Viscous model	RANS
Turbulent model	k-ε RNG
Minimum cell size	H/48
Rate of cell size increase	<1.2
Y^+	<300
Velocity at the inlet	Defined ABL Equations (4.9 – 4.12)
Domain ground	0.08m roughness
Model walls	wall
Pressure velocity coupling	SIMPLE
Momentum	Second-order upwind
Turbulent kinetic energy	Second-order upwind
Turbulent disspation rate	Second-order upwind
Convergance Criteria	10^{-4} to 10^{-7}
Pressure Under Relaxation Factor	0.3

4.5 Validation Analysis using Experimental Results

In this section, comparisons are conducted between the mean pressure coefficient (C_{pmean}) distribution using CFD against their counterpart values from the WOW tests for the 2.1 m two-story (2S-2.1) elevated case, as shown in Figures (4.6-4.8). In the figures, the symbols N, S, E, and W refer to the wall location as per the experimental model inside WOW (i.e., E refers to the East wall). The figures show a good agreement between the two modeling methods. In the case of wind acting at 0º direction, the roof and floor surfaces experience higher suction near the windward region where the wind separation occurs. The floor surface experiences higher suction around the stilts, and it is lower at the midspan. The agreement is better in the side walls. The windward wall of the CFD model experiences higher pressure at the middle than that for the WOW model. The difference does not exceed 7%. In case of 90º wind direction, the resulting C_{pmean} matches well on the roof, windward

wall, and floor surfaces. However, the floor surface of the CFD model experiences higher suction near the intermediate column. In oblique wind direction, CFD results agree with the experimental results showing that higher suction occurs on the floor surface near the silts.

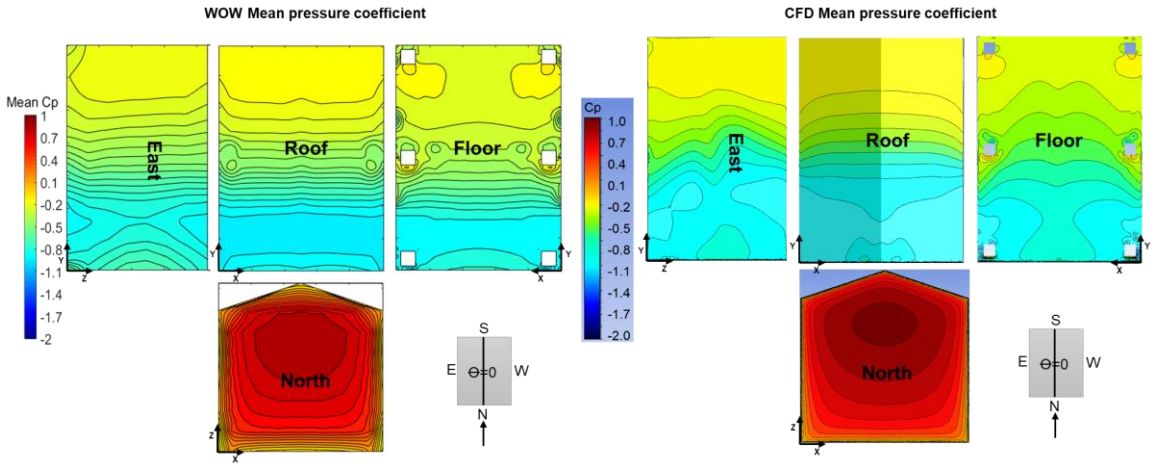

Figure 4.6 Local C_{pmean} of 2S-2.1 case CFD vs. WOW-0º wind direction

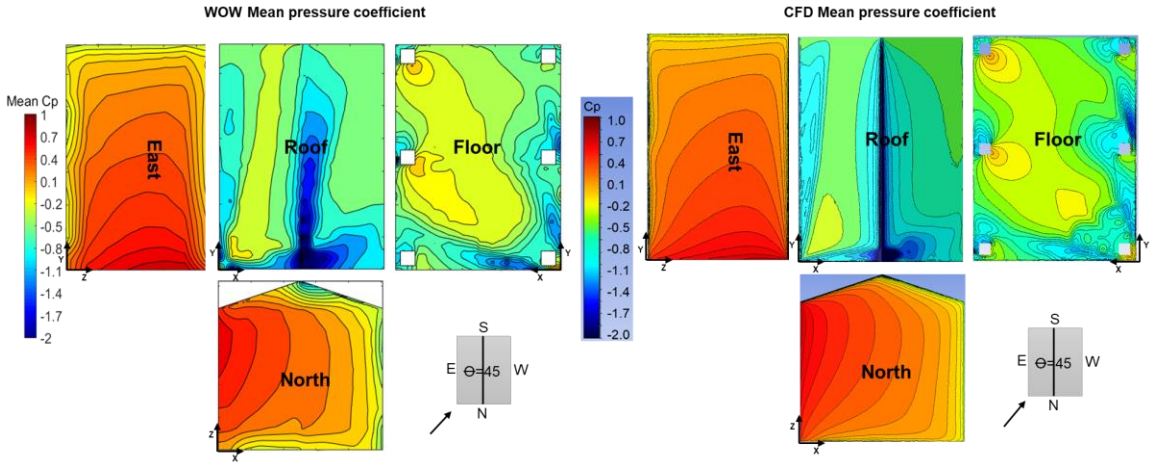

Figure 4.7 Local C_{pmean} of 2S-2.1 case CFD vs. WOW-45º wind direction

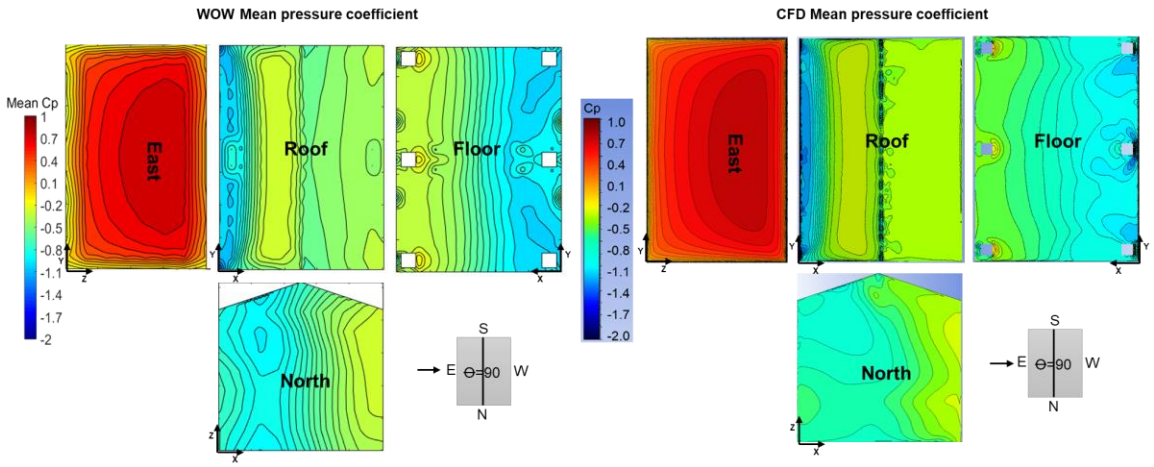

Figure 4.8 Local C_{pmean} of 2S-2.1 case CFD vs. WOW-90º wind direction

As shown in Figure 4.9, several slices are taken to present a more detailed comparison between the two methods. Figures 4.10 and 4.11 show the C_{pmean} plot variation with the model length for the 2S-2.1 case. Those figures show the agreement between the experimental and numerical results. For the wind moving along the Y-direction (0 wind direction), Figure 4.10 shows that the agreement is good, especially for the windward wall, sidewall, and floor surfaces. For wind moving along the X-direction (0 wind direction), Figure 4.11 shows a high suction region beside the intermediate column, which is also observed in Figure 4.8. Generally, the figures show that the difference between the two methods does not exceed 10%.

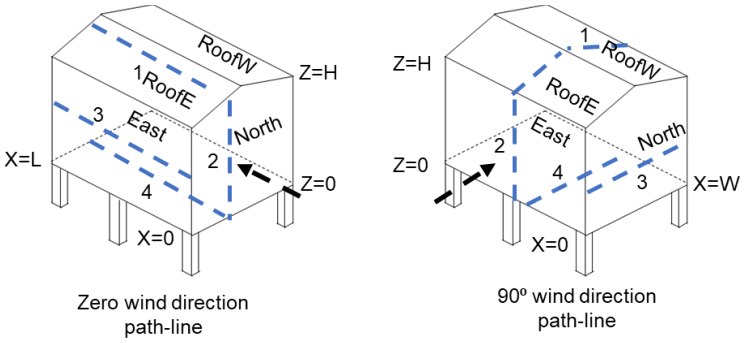

Figure 4.9 Full-scale elevated house path-lines for different wind flow directions

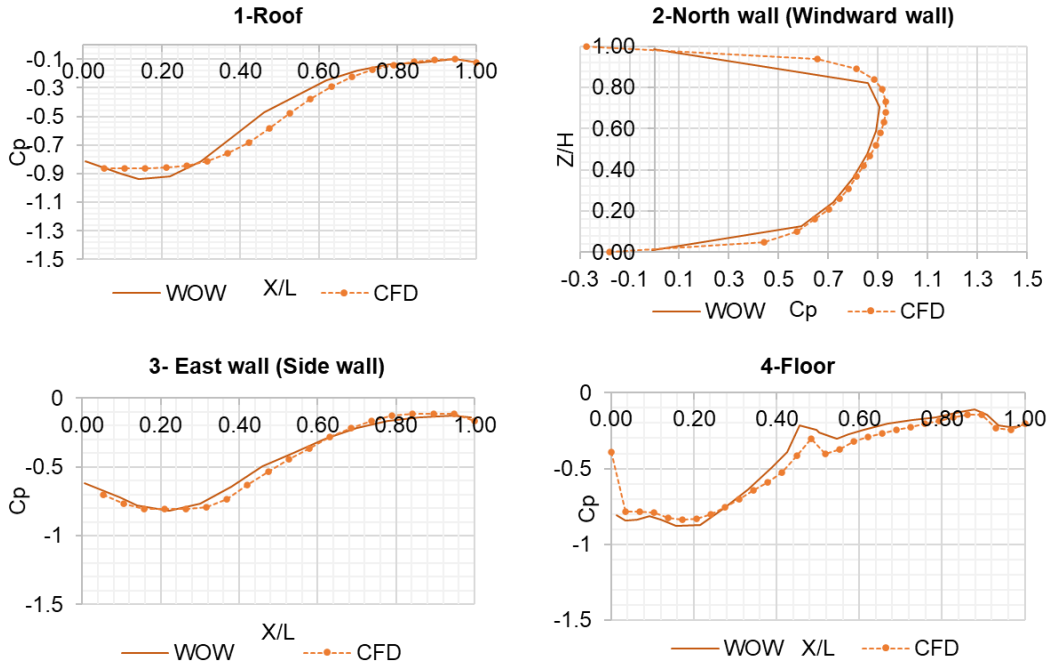

Figure 4.10 C_{pmean} variations along different lines of 2S-2.1 case CFD vs. WOW 0º wind direction

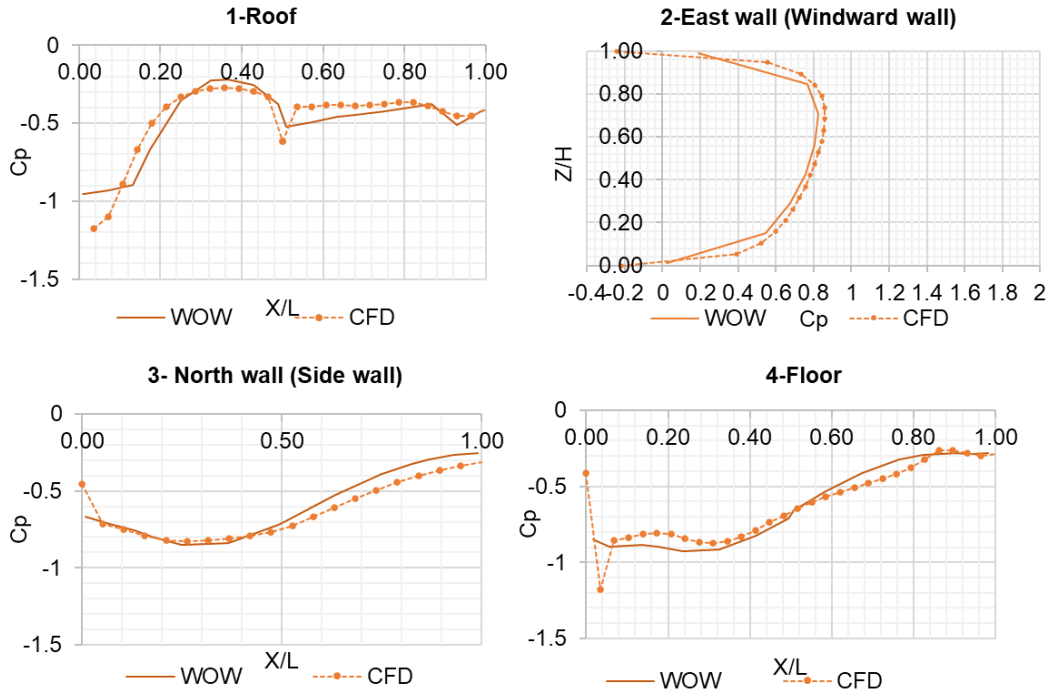

Figure 4.11 C_{pmean} variations along different lines of 2S-2.1 case CFD vs. WOW 90º wind direction

Finally, as shown in Figure 4.12, a comparison is presented for each surface for the average pressure coefficient (C_p) with WOW results. CFD positive pressure coefficient is around 7% higher than WOW for the windward wall. There is a 3% difference at the East wall and roof surfaces. CFD values are 6% higher for the floor surface. The deviation between CFD and WOW is very small and acceptable. This agreement takes us forward to the next steps of conducting the parametric study using the same boundary conditions identified for the validated model.

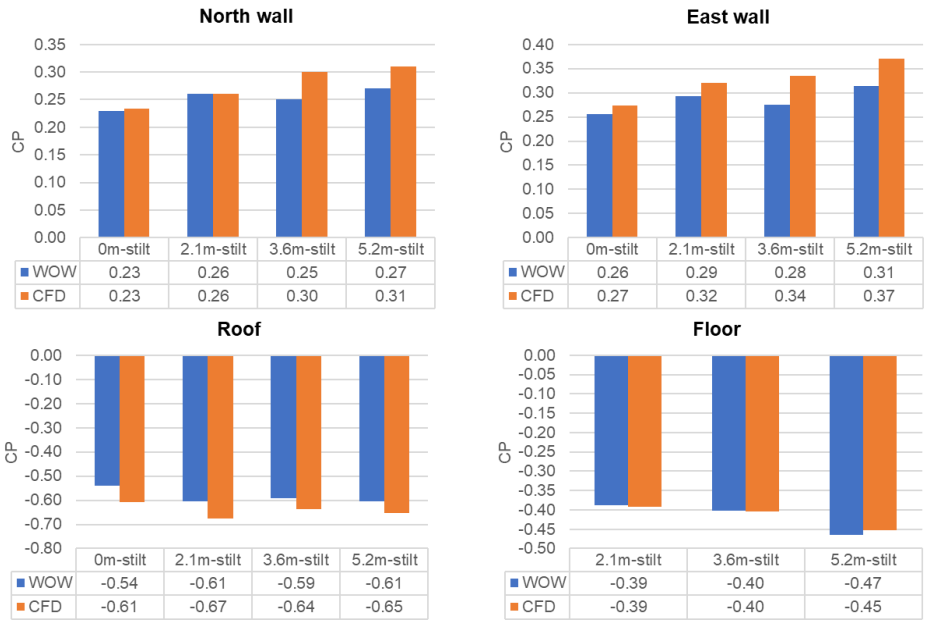

Figure 4.12 Mean pressure coefficient of each surface of 2S-2.1 case CFD vs. WOW 0º wind direction

4.6 Flow Streamlines and the Resulting Wind Pressure Coefficients

4.6.1 Effect of increasing the stilt height

In this section, the results of the simulated one-story and two-story gable roof models, with different stilt heights ranging between 0m to 5.2m with 0.6m increment, are explained. First, the wind flow streamlines are presented to help understand the flow characteristics and the consequent wind loads. A midspan slice is taken along the ridgeline, as mentioned in Figure 4.13. Figure 4.14a shows the flow streamlines of various cases under 0º wind direction. The effect of house elevation can be seen by comparing the 1S-0 and 1S-5.2 cases. As the

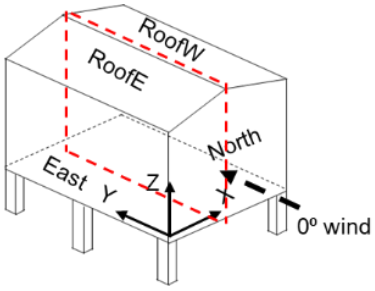

Figure 4.13 Midspan section of the simulated model

model elevation increases, the stagnation point occurs at a higher elevation on the windward wall. This causes differences in the pressure distribution on the windward wall. The air circulation in the structure wake moves slightly down in the elevated case (1S-5.2), under 0º wind direction, and a separated flow forms on the floor surface. And, in the case of 90º wind direction, the wake moves down until it merges with the separated flow formed below the floor, as shown in Figure 4.14b in the case 1S-5.2. These changes in wake and flow separation zones result in higher wall suctions than the suction found for the on-ground case. These findings agree with the observations discussed by Amini and Memari [34]. Under 0º wind direction, the flow separation formed above the model roof is larger in the elevated case (1S-5.2). Evidently, this is attributed to the roof height since a similar separation zone size is also observed in the two-story on-ground case (2S-0). Also, in Figure 4.14a, the comparison between 2S-0 and 1S-2.1 shows two different models with the same mean roof height from the ground. Above the model roof, the separation zone is similar in the two cases.

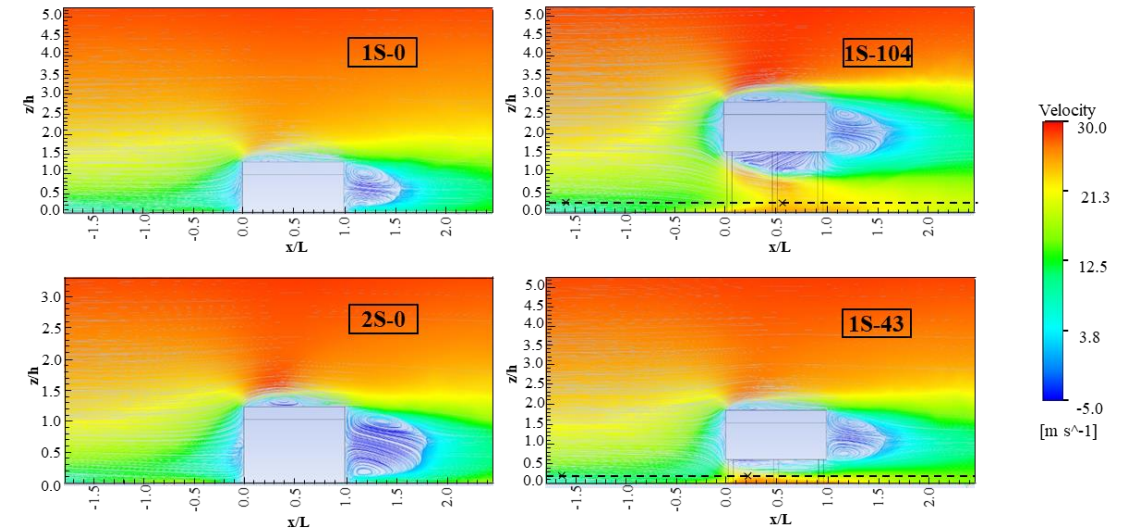

(a)

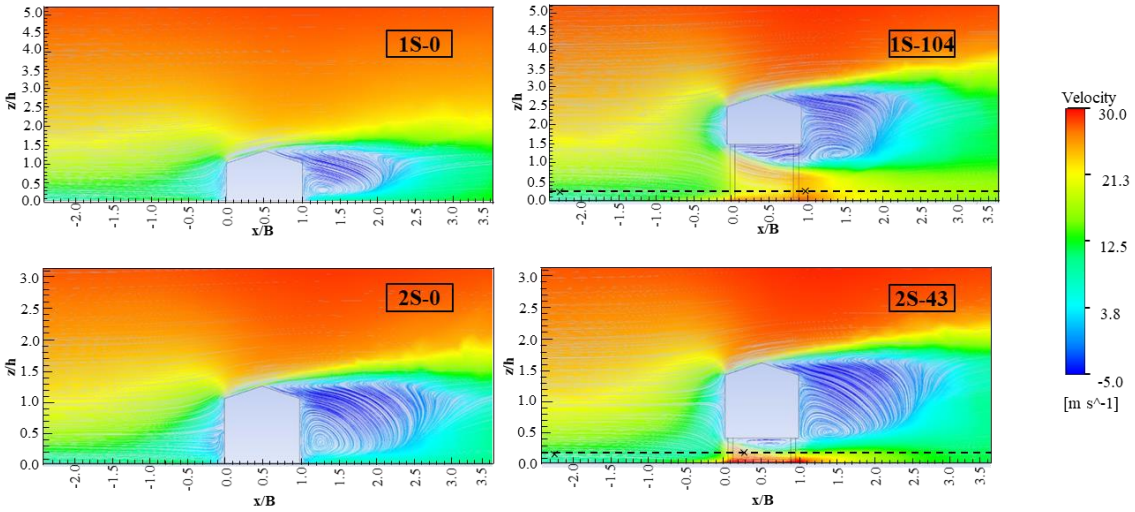

(b)

Figure 4.14 Airflow streamlines at midspan section of the CFD model (a) 0º wind direction, and (b) 90º wind direction.

Below the floor surface, air circulation occurs in the smaller elevated case, Figure 4.14a (1S-2.1), causing local high suction. However, in the large stilt case (1S-5.2), the circulation happens away from the building, and the flow separation on the floor surface is enlarged, resulting in a less concentrated suction. In Figure 4.14b, the vortex formed, under

90º wind direction, is more critical and causes higher suction on the floor. The most important observation is the wind speed increase beneath the building floor. This observation justifies the reoccurring damages observed for the floor in elevated houses during extreme wind events. For instance, in the lower elevated case (1S-2.1), Figure 4.14a shows that the velocity, at the marked locations 0.75m above the ground level, increases from 12.3 m/s near the inlet and reaches 22.5m/s (80% increase) below the model. In the higher elevated case, Figure 14.4a (1S-5.2), the velocity below the model at the marked location reaches 17.2m/s (39% increase). The velocity increase beneath the floor surface is more critical in the two-story case due to the larger blocked area of the two-story walls, as shown in Figure 14.4b. The velocity reaches 23.5 m/s (91% increase) and 25.2 m/s (104% increase) in the cases 1S-104 and 2S-43, respectively.

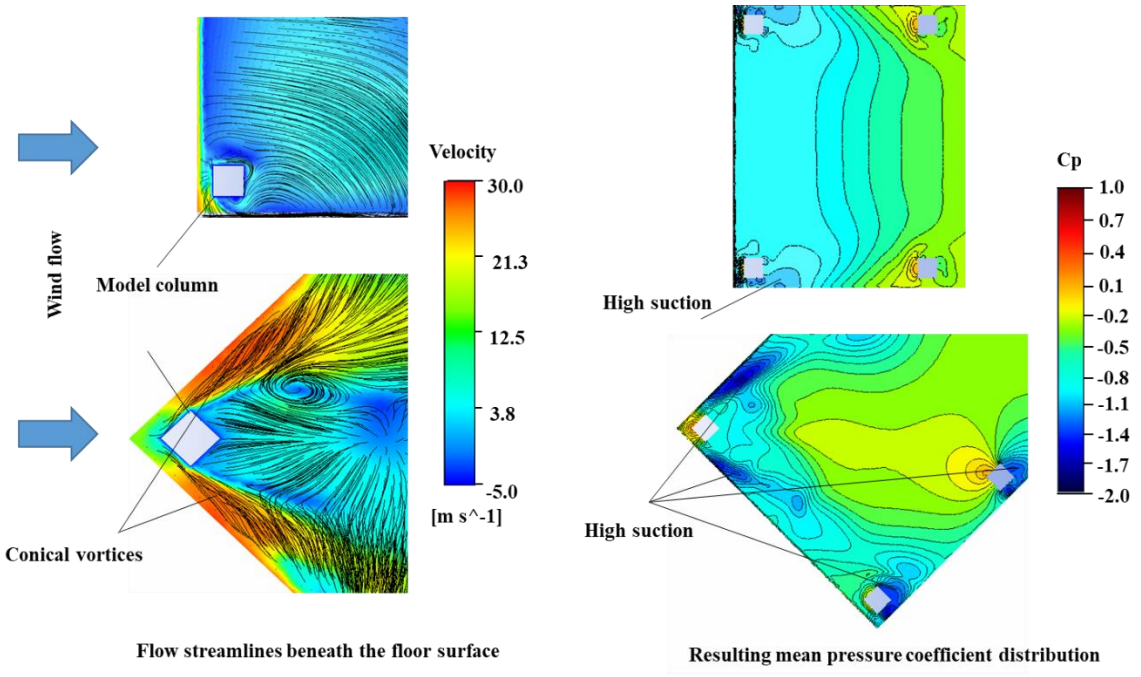

Figure 4.15 A plan view of the 3D streamlines around the model stilt of 1S-2.1 case and the resulting C_{pmean}

Figure 4.15 shows the flow separation at the edge of the floor surface in both wind directions 0º and 45º. This flow separation causes higher suction along the edges. It is worth mentioning that, in case of wind acting in an oblique direction, a higher suction region appears around the stilts. Figure 4.15shows the plan view of the flow streamlines below the model floor surface with conical vortices formed in case of oblique wind direction with higher wind speeds than 0º wind case. These vortices are the main reason for the suction regions occurring along the sides of the stilts.

4.6.2 Effect of increasing the floor aspect ratio

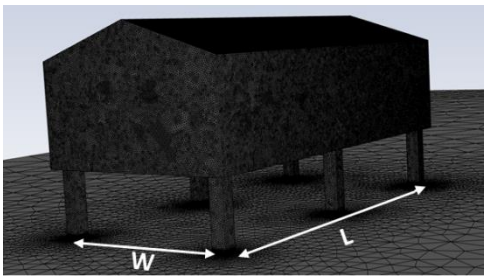

Figure 4.16 1S-2.1 elevated house after increasing the floor aspect ratio

This section covers the resulting flow streamlines and pressure coefficients while changing the floor aspect ratio. The contour line plots provided in this section are for four different aspect ratios (A=1, 1.5, 2, and 2.5) and the same stilt height (St=2.1 m). The floor aspect ratio (A) is changed by increasing the building length (L), as shown in Figure 4.16. By increasing A, the vortices' size at the wake increases and become one large vortex, as shown in Figure 4.17. This is expected to cause an increase in the resulting suction on the leeward wall. Figure 4.17 shows that the distance prior to flow reattachment on the roof surface slightly increases as the aspect ratio increases. This increase is negligible as it does not cause much difference in the high suction region, as shown in Figure 4.22. Below the model floor, for A=1, the flow is reattached at the end of the floor surface (i.e., L=W). When A=1.5, the flow is reattached at the middle (i.e., L=0.75W). Thus, as the floor aspect ratio increases, the distance of the flow separation on the floor decreases.

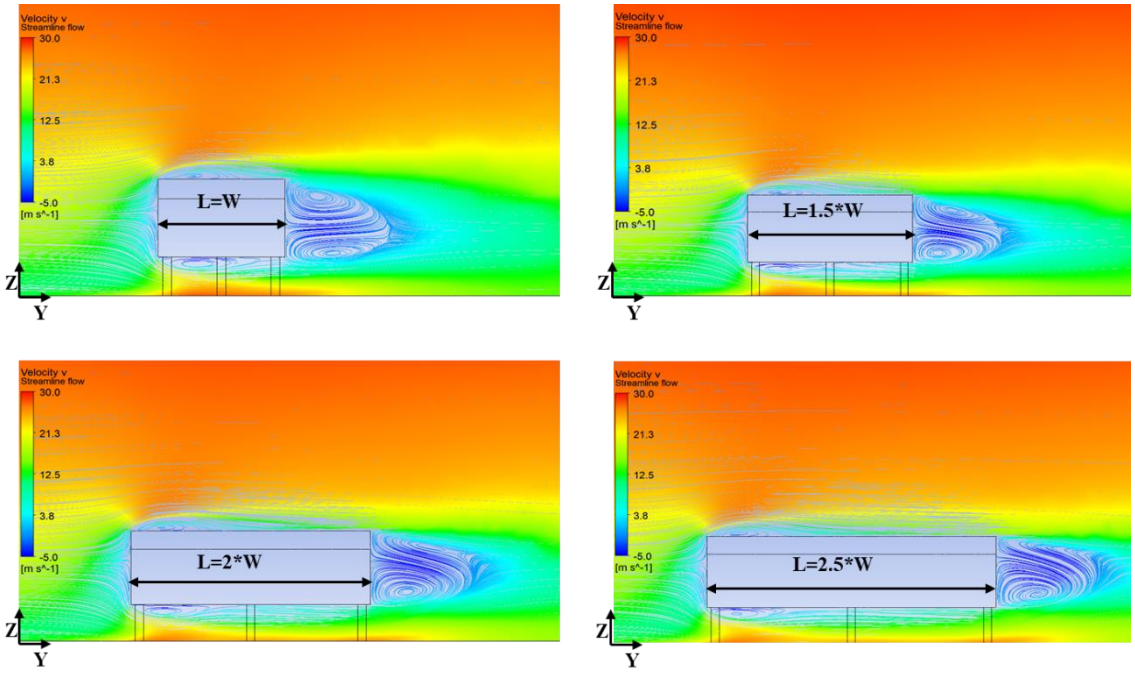

Figure 4.17 Airflow streamlines at the midsection of the computational domain for different stilt heights under 0º wind direction

The resulting mean pressure coefficients can be investigated from Figures 4.18 to 4.20, for the three wind directions 0º, 45º, and 90º. As shown in Figure 4.18, by comparing the two floor aspect ratio cases (A=1 and A=2.5), the high suction region occurs along the same length in the two cases. In the large aspect ratio case (2.5), the high suction region is located at the first quarter of the model length (L), similar to the C_{pmean} distribution on the walls and roof surface, for wind acting at 0º direction. It is also noticed that the C_{pmean} are not much affected by the floor aspect ratio increase. However, by checking Figure 4.20 for the 90º wind direction, the suction occurring around the columns is higher in case of A=2.5. The increase of high suction region, for A=2.5, is noticeable near the intermediate column. The roof surface windward region experiences higher suction in case of A=2.5. The same observations occur in the suction values, for the 45º wind case. The current study tests only

the change in floor aspect ratio without increasing the number of stilts. Therefore, in the future, it is recommended to investigate more cases with different aspect ratios and stilt patterns.

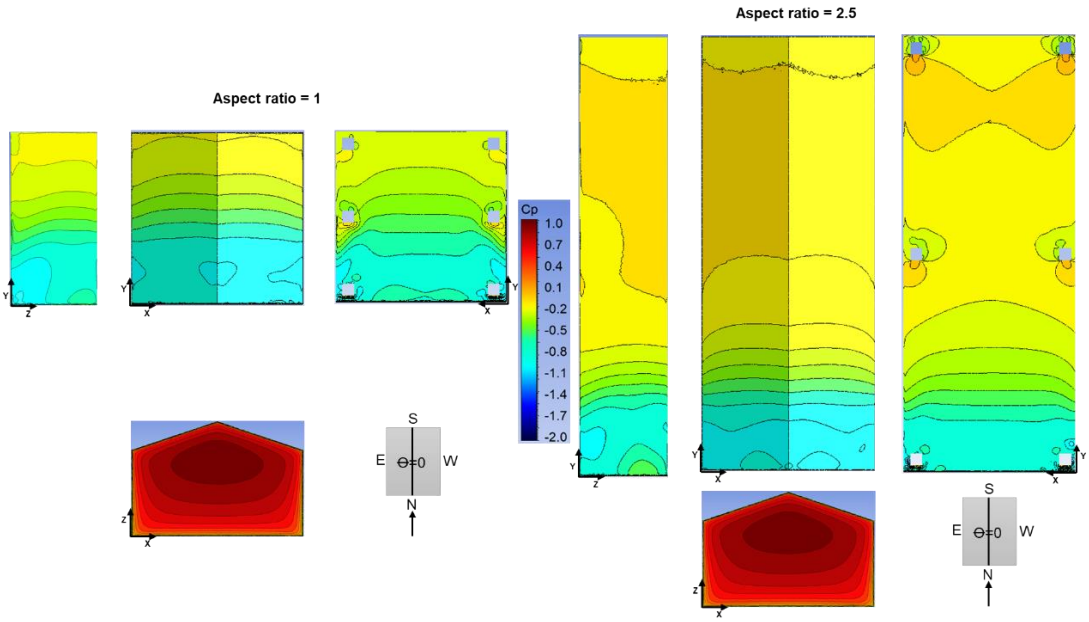

Figure 4.18 Mean pressure coefficient of 1S-2.1 case with A=1&2.5 and 0º wind direction

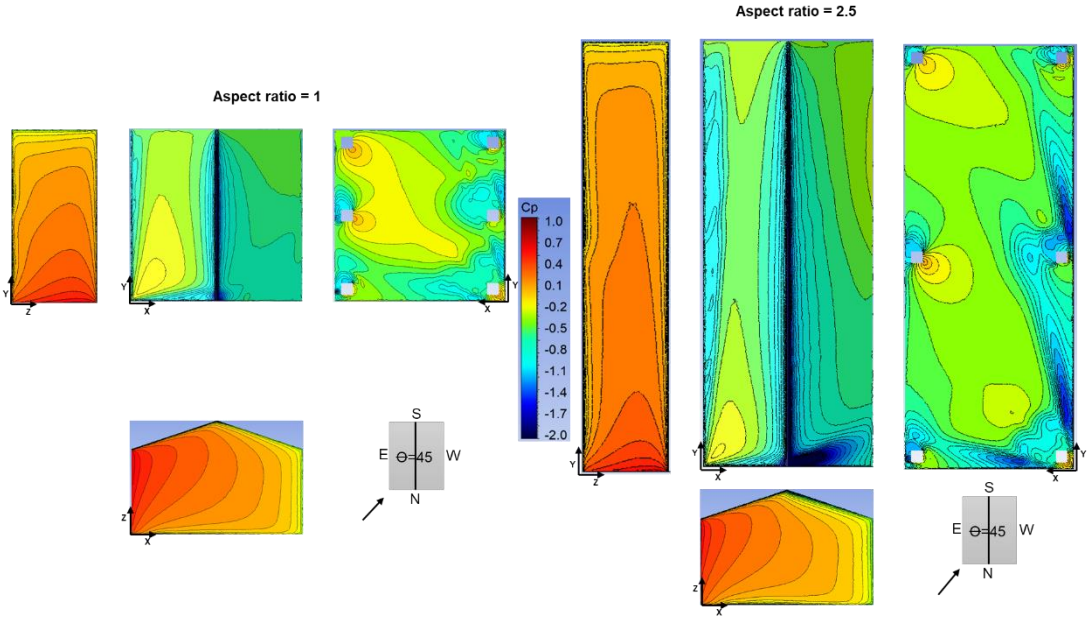

Figure 4.19 Mean pressure coefficient of 1S-2.1 case with A=1&2.5 and 45º wind direction

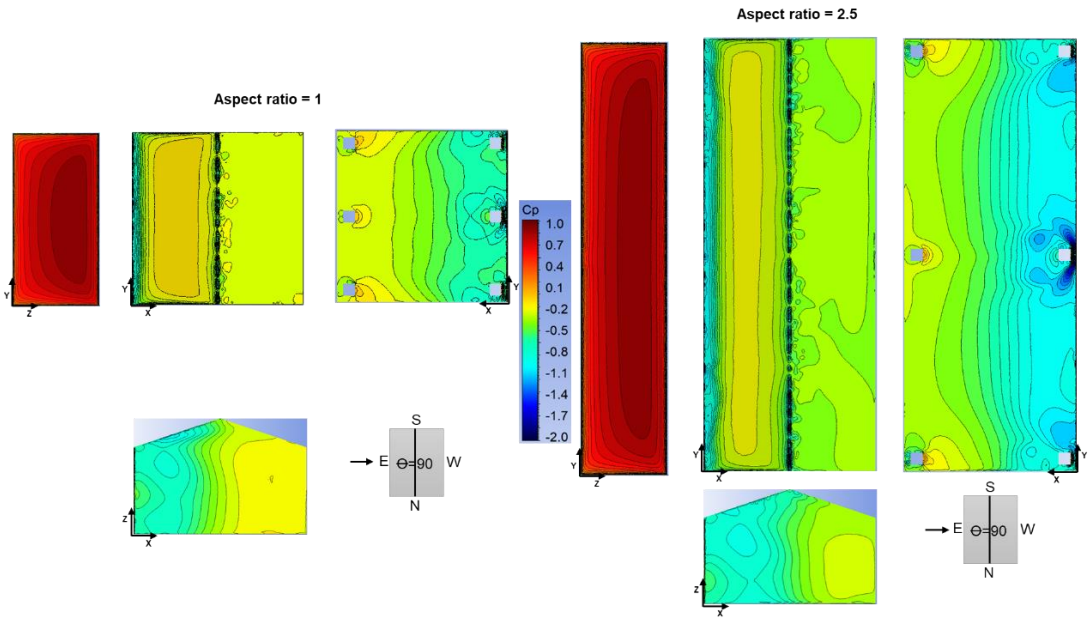

Figure 4.20 Mean pressure coefficient of 1S-2.1 case with A=1&2.5 and 90º wind direction

4.7 Total Wind Forces and Overturning Moment

For each surface of the one-story models, the wind force is calculated then normalized with respect to the wind force of its counterpart on-ground case. Then, the relationship of the resulting force ratio with the stilt height is drawn, as shown in Figure 4.21. Similarly, the normalized force relationship with the floor aspect ratio is drawn, as shown in Figure 4.22. As illustrated in Figure 4.9, for wind acting at zero direction, it hits the North wall. In that case, the wind force on the North wall increases rapidly with the stilt height; for every 0.6m stilt height, the total force increases by around 10% till the force doubles when the stilt height is 4.8m. And this is also observed on the East wall for 90º wind direction. At the oblique direction, the force ratio becomes triple for the 5.2m stilt case. However, when these walls are aligned with the wind direction, they don't experience a noticeable change. For the roof surface, at 45º and 90º wind directions, after elevating the house 0.6m upward, the force value drops to 80%, then it increases gradually to be higher by 15% than

the on-ground case. At 0º wind directions, after elevating the house 0.6m, the force on the roof surface drops to 95%, then it increases till it becomes higher by 40% than the on-ground case. For the floor surface, the wind force is normalized with respect to the 0.6m stilt case. The shaded region of the graph, from 0 to 0.6m, has no data because this surface appears from the 0.6m stilt case. In case of 45º wind direction, the total vertical force increases by 35% for the 5.2m stilt case. In the other two wind directions, the total force decreases, compared to the 0.6m stilt, till the 2.1 m case, then it increases till it becomes 10% higher than the smallest stilt case. This observation indicates that the 45º wind case is responsible for the increase of the negative pressure region on the floor surface

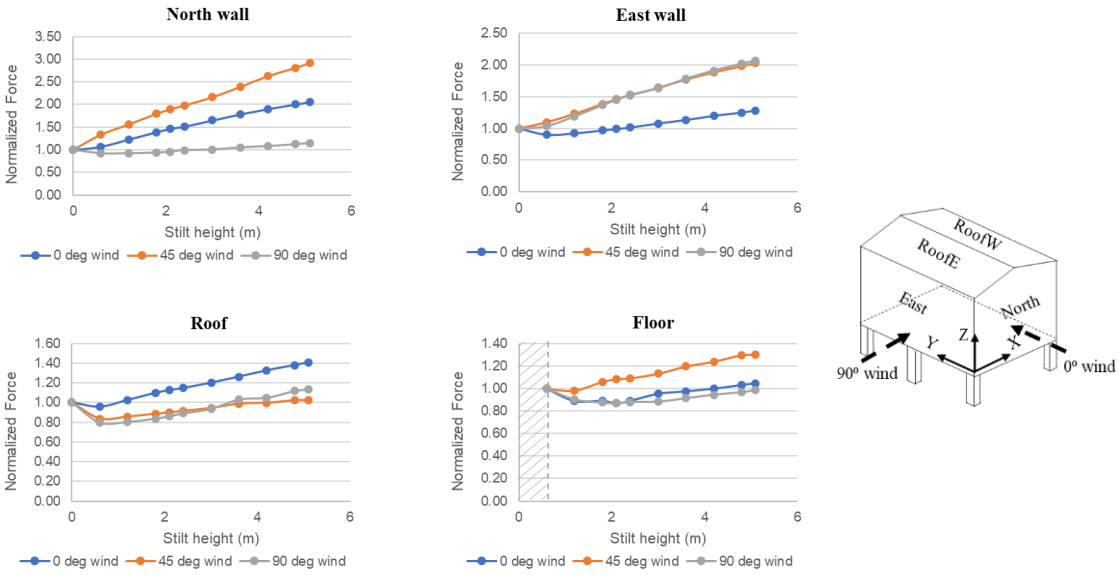

Figure 4.21 Relation between the average pressure coefficient of each model surface and the stilt height

The force increase is also noticed by increasing the model aspect ratio. By normalizing the resulting force on each face using the model with A=1 as a reference, a significant force ratio increase occurs, especially in the floor and roof surfaces. The building windward walls

experience a noticeable increase in the positive wind force (e.g., North wall for 0º wind direction) and reach up to 40% in case of A=2.5. This increase is higher for the East wall due to the wall area increase. At 90º wind direction, there is around 80% increase in the wind for every 0.25 increase in the floor aspect ratio. For the roof and floor surface, the vertical force in case of A=2.5 is five times the case A=1. The zero wind direction graph clearly shows the slight change of the acting wind force on the sidewalls, roof, and floor, as observed from the contour plots.

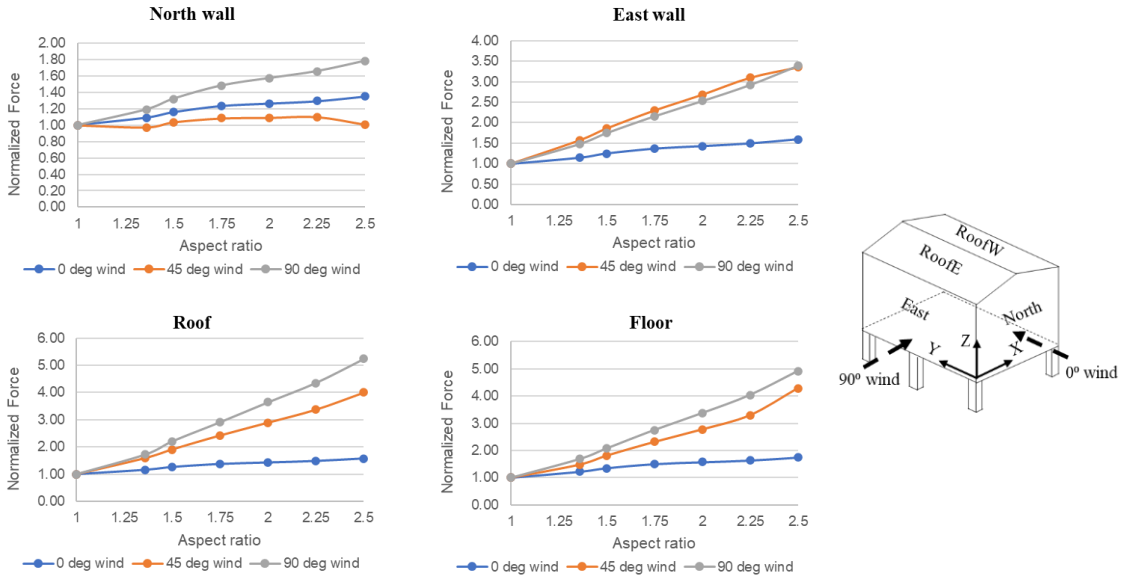

Figure 4.22 Relation between the average pressure coefficient of each model surface and the floor aspect ratio

Investigating the total resulting forces on the building foundation is an essential objective of the current study. This section presents the effect of changing the stilt height and floor aspect ratio on the total uplift, shear force, and overturning moments. Figures 4.23 and 4.24 show the total force and overturning moment acting on the model foundations. The normalized forces are calculated by dividing the stilt case total force over

the on-ground case total force. The force direction is named according to the building axis shown in Figure 2.1. The following graphs present only the forces at the longitudinal direction of the wind flow or the vertical direction. The lateral wind forces are very small (e.g., F_x in case of wind acting at zero direction), so the normalized force appears in the graph to be zero. From Figure 4.23, by increasing the model stilts, there is a noticeable increase of the total shear forces F_x and F_y in case of wind acting at angles 90º and 0º, respectively. And the total force in case of 5.2m stilt reaches 2.5 times the on-ground case. For the vertical force, the mean force F_z is always acting upward. This means the uplift force on the roof surface is larger than the force acting on the floor surface. Figure 4.23 shows lower values of vertical forces in the elevated cases due to the presence of a new force acting downward on the floor surface. In the largest stilt case, the ratio turns negative, in case of 0º wind direction, because the force acting on the floor surface is larger than that for the roof surface. The 4^{th} and 5^{th} graphs show that the overturning moment resulting from the wind flow drops at 0.6m stilt case then increases tremendously. The 0º wind case which hits the North wall causes a 450% increase in the resulting moment on the 5.2m stilt case. For the 90º wind case, the flow hits the East and roof surfaces causing an 800% increase in the moment (M_y). It is worth mentioning that the percentage of increase is affected by the surface area increase, which also means an increased moment arm. A similar observation can be seen in Figure 4.24. However, the effect of changing the floor aspect ratio on the moment is not as significant as the stilt height effect. For instance, M_y increases by 250% in case of A=2.5. However, the vertical force increases with the aspect ratio increase to reach 350% in case of A=2.5. Therefore, the resulting increase of the shear and overturning moment on the building foundation, due to stilt height increase, is

substantial and should be considered in the future design of elevated house. In addition, the increase of the vertical force, acting upward, due to the aspect ratio increase is considerable as well. As the surface area increase has a big share in the mean force increase, more investigation is needed in the future on large floor aspect ratio cases. For this reason, the following chapter includes a more extensive study of a large floor aspect ratio case to investigate also the peak pressure coefficients.

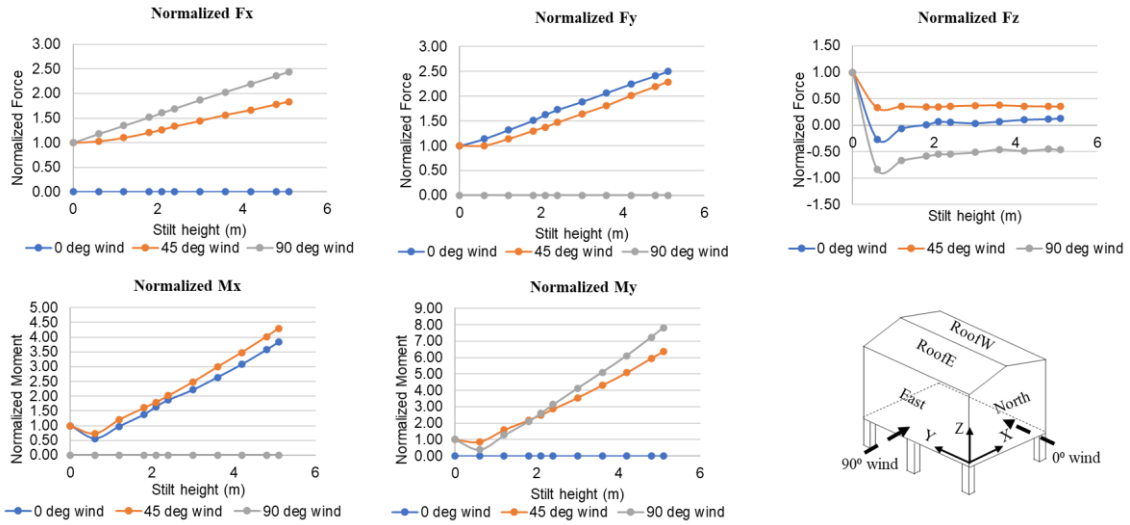

Figure 4.23 Relation between normalized total wind forces on the foundation and the stilt height

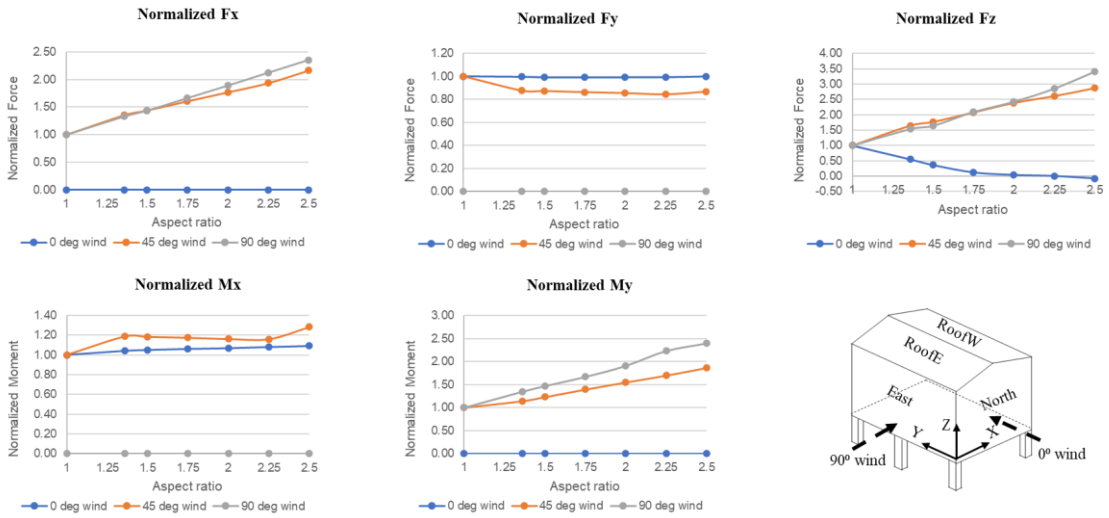

Figure 4.24 Relation between normalized total wind forces on the foundation and the floor aspect ratio

4.8 Investigating the Effect of Adding Stairs on an Elevated House

This section investigates the effect of adding external staires beside a single-story elevated house. CFD simulation is conducted to evaluate the effect of external stairs on the wind flow and the resulting wind loads. This numerical simulation is done on a full-scale 2.1 m elevated house with the same dimensions, roof angle, and boundary conditions as the parametric study. The computational domain dimensions and the mesh size are taken the same. However, the mesh size is coarsened along the stairs due to the complicity of its geometry. The same solver setting is used in this simulation as well. Figure 4.25 shows the model configuration simulated and tested at three wind directions; 0º, 45º, and 90º.

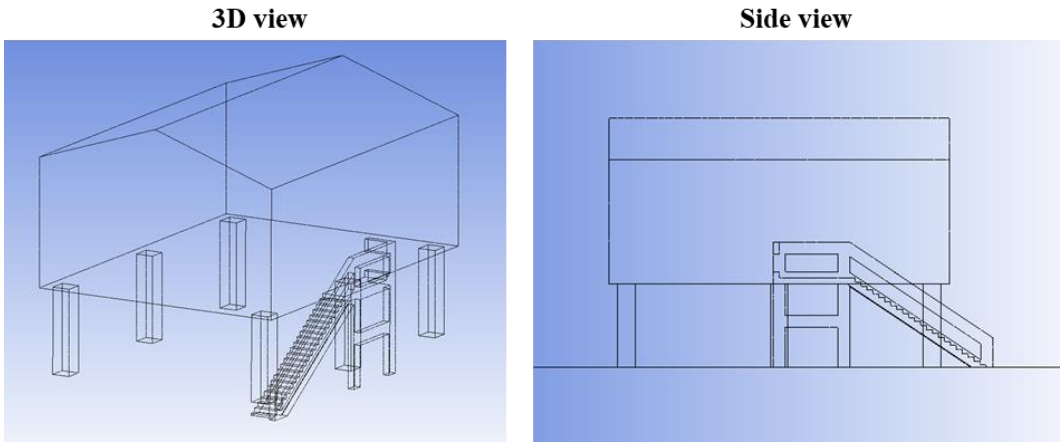

Figure 4.25 Gable roof house drawing elevated by 2.1 m with stairs

As shown in Figure 4.26, some deviations appear in the mean pressure coefficient distribution on the right figure due to the presence of the stairs. There is a slight reduction of the C_{pmean} in case of the house with stairs. This difference is noticeable only for the floor surface; the pressure coefficient is much lower, especially at the leeward part. The same reduction can be seen in the other two wind cases in Figures 4.27 and 4.28. Both roof and floor surfaces experience lower negative pressure. These observations reveal that there is no need to add the stairs in the experimental studies as it does not cause a noticeable effect and does not increase the wind loads on the house.

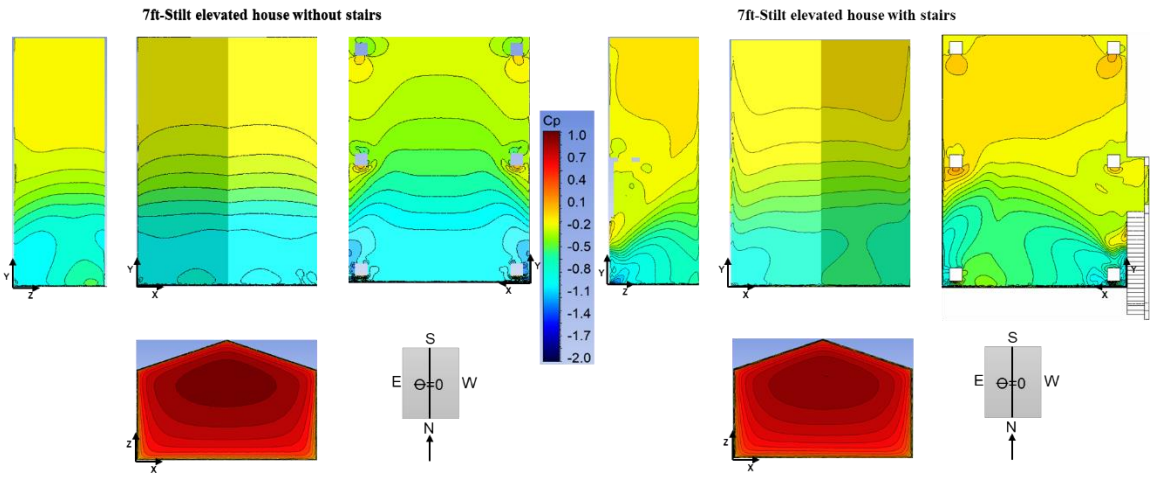

Figure 4.26 Mean pressure coefficient of S1-2.1 case with and without stairs under 0º wind direction

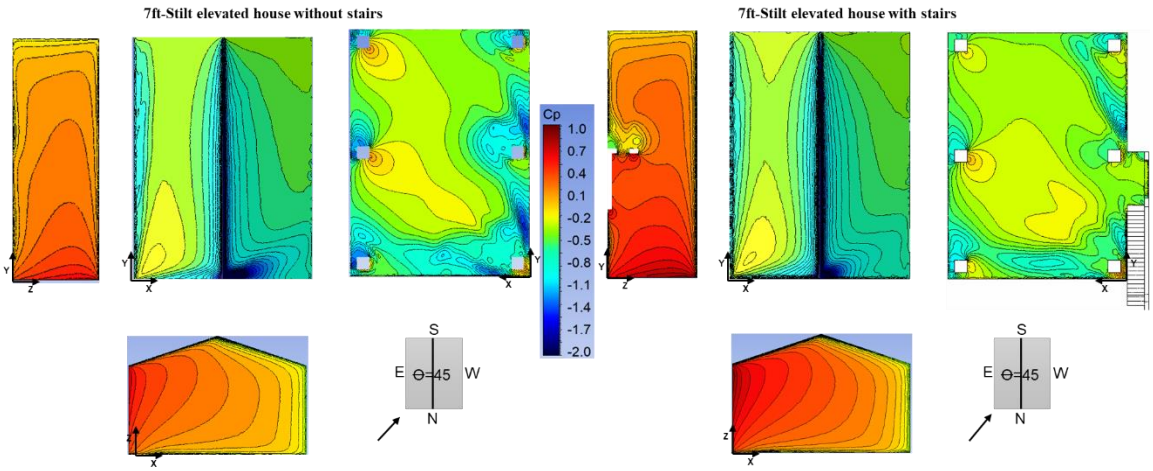

Figure 4.27 Mean pressure coefficient of S1-2.1 case with and without stairs under 45º wind direction

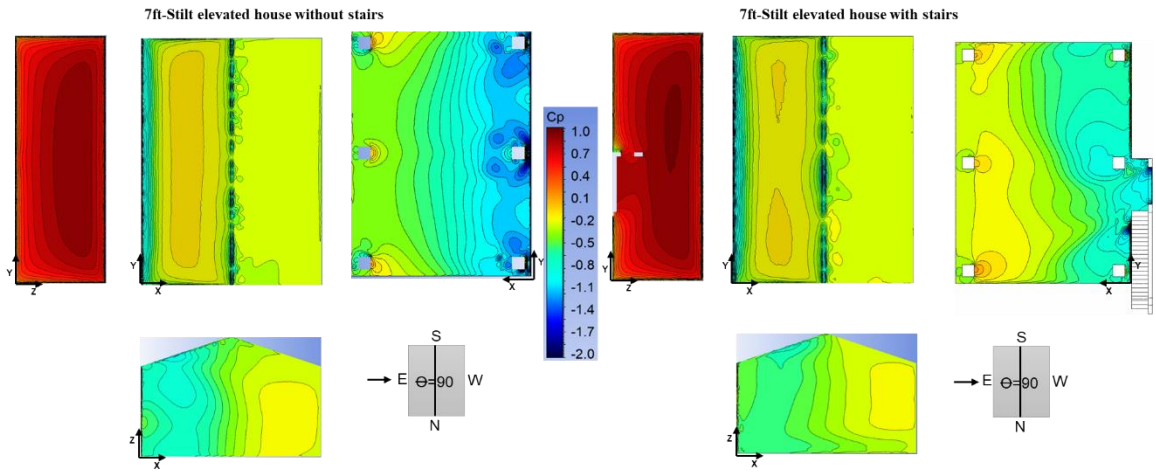

Figure 4.28 Mean pressure coefficient of S1-2.1 case with and without stairs under 90º wind direction

By comparing the average pressure coefficients (C_p), Figure 4.29 shows that there is not much difference between the two cases. For 0º and 45º wind directions, after adding external stairs, the negative C_p value on the building roof and walls is lower by around 7% and 5%, respectively. However, the positive C_p value on the windward wall is higher by 7%. After adding stairs, the C_p considerably decreased by 35%, as concluded from the contour plots. Table 4.3 shows the wind force acting on the elevated house in case of with or without stairs. It reveals that the total force acting on the elevated house (including wind load on the stairs) did not experience a noticeable change. The force share of the stairs is 5%, 15%, and 13% for 0º, 45º, and 90º, respectively. These are considerable values that should be considered in the future design of stairs.

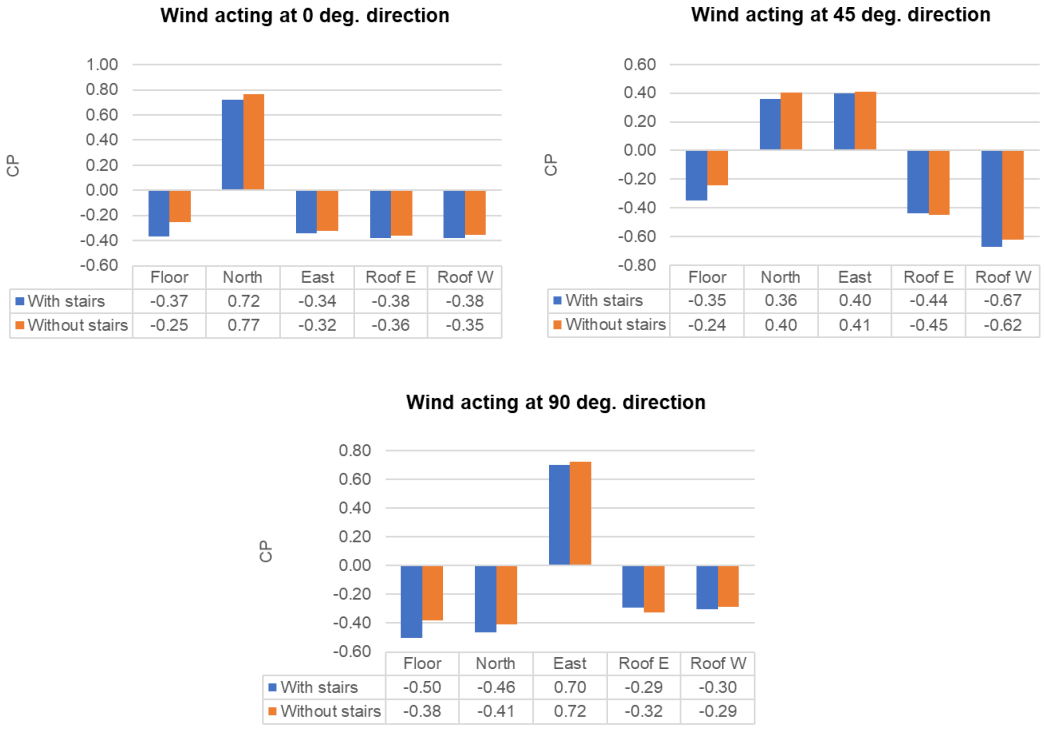

Figure 4.29 Mean pressure coefficient of each surface of 1S-2.1 case without stairs vs. with stairs

Table 4.3 Total force acting on the elevated house and external stairs

	Global forces (Newton)											
	without stairs			with stairs								
				Model			Stairs			Total		
	Fx	Fy	Fz	Fx	Fy	Fz	Fx	Fy	Fz	Fx	Fy	Fz
0	-10	7855	368	51	7461	1761	353	392	-239	404	7853	1522
45	-9913	6712	3704	-8460	5920	4926	-1114	978	-2	-9574	6898	4925
90	-10250	37	-3297	-9055	-57	-1338	-1137	-51	3	-10192	-109	-1335

4.9 Conclusion

The chapter presents a parametric study performed using CFD modeling on a full-scale (prototype) on-ground and elevated houses. RNG k-ε turbulent model is used to solve the governing equations inside the computational domain. First, the validation study shows a

good performance of the RANS model compared to the experimental work results for the two-story case. Using the same model parameters, a parametric study is conducted to investigate the characteristics of wind flow surrounding the building for different stilt heights and floor aspect ratios.

The flow streamlines inside the computational domain show that the flow separation region increases as the stilt height increases. However, the flow separation region decreases by increasing the model aspect ratio. In the small stilt cases, the wind speed increases beneath the building floor due to venture effect through the air gap. A flow circulation of air took place between the intermediate columns. This clarifies the reason behind the high negative pressure around the model stilts. The resulting local mean pressure coefficients are similar for different floor aspect ratios of the elevated house in case of wind acting parallel to the roof ridge. However, for 45º and 90º wind directions, the suction occurring in the roof surface and around the stilts in the floor surface is significant when the aspect ratio is large.

Through this chapter, the effect of stilt height and floor aspect ratio on the total forces acting on the foundation is studied as well. The total shear force acting on the foundation increases significantly as the stilt height increases. The total vertical force dropped by elevating the house due to the presence of a new force on the floor. By increasing the floor aspect ratio, the overturning moment and the vertical force increases significantly. The increase of the surface area contributes to this increase. These forces need to be considered during the design of foundation.

This study reveals several recommendations which need to be considered in future work. Higher wind velocity is noticed beneath the house floor of the (1.8m -2.4m) stilt

cases. These stilt heights are widely used and need to be monitored precisely to avoid the occurrence of several damages. The observed increase in the pressure coefficients emphasizes the need to study changing the building floor aspect ratio. The resulting increase of the shear forces and the overturning moments, due to stilt height increase, acting on the building foundations is significant and should be taken into consideration in the foundation design. The increase of the total vertical force, for large aspect ratio, acting on the foundations is noticeable and should be considered. The commonly used configuration of stairs does not cause a noticeable effect on the resulting pressure, and it can be excluded from experimental testing to reduce time and cost. The shown results need more investigation showing peak pressures and instantaneous wind streamlines. Therefore, it is recommended to simulate the transient flow using Large Eddy Simulation (LES) to better understand the flow characteristics. The next chapter shows a numerical simulation using LES of an elevated house with a larger aspect ratio and standing on more stilts.

5. CHAPTER V

LARGE-EDDY SIMULATION OF WIND FLOW THROUGH ELEVATED HOUSES

This chapter discusses the aerodynamics of a large-scale elevated gable-roof house using Large Eddy Simulation (LES) modeling. The LES method is a widely used in the field of Computational Fluid Dynamics (CFD), which has shown efficiency and accuracy of simulating wind flows through bluff bodies in the literature [41]–[44]. It allows simulating time-dependent flow and calculating instantaneous velocity and peak pressures over the bluff bodies surfaces. Using LES method, the wind flow is separated into small and large eddies. The LES turbulence model can simulate small scales (subgrid) and solve large scales accurately. This simulation can generate the separation and recirculation regions better than the Reynold Average Navier Stokes (RANS) simulation [73]. The LES method requires more time to solve the flow quantities at all the grid points.The filtering feature (averaging over the space) allows obtaining the instantaneous mean, peak values, and wind fluctuation. This is the main advantage of using LES over the RANS method. It is worth mentioning that the LES method does filtration of the peak values to reduce the computation time.

In literature, Xing et al. studied the wind flow through a gable roof low rise building [62]. The study showed better agreement and more efficiency in the LES model, compared to a 1:20 scaled wind tunnel model, than RANS model. The LES model provides better performance than the RANS model in showing local pressure coefficients especially for oblique wind angle. Aly et al. used the LES simulation to study the wind effect on low-rise buildings and compared the results with full-scale field measurements [74]. The

comparison showed a great performance of LES model in reproducing peak pressure coefficients. Amini et al. conducted a numerical simulation using LES to study the effect of increasing the number of stilts from four to nine [61]. The authors used the one-story model presented in chapter two for their simulations. The numerical model was validated by comparing the results with the WOW experimental results. However, the defined turbulence intensity does not match the modified one for the WOW after applying PTS (Partial Turbulence Simulation). Amini et al. showed an increase in wind flow speed below the model floor and observed a high suction region near the edges and around the stilts regardless of the wind direction. The authors recommended performing more numerical studies to better understand the aerodynamics and studying more patterns of stilt distribution [61].

The parametric study discussed in chapter four of this diseertation shows an increase in total wind forces due to the increase in the floor aspect ratio. However, the numerical study provided in chapter four focused only on assessing mean wind forces and mean pressure distribution using RANS modeling. In this chapter, to arrive at a conclusion regarding the peak wind loads on elevated structures with a large floor aspect ratio, another numerical study is performed using LES. First, a validation study is conducted with a floor aspect ratio of 1.36 (A_1.36 case), as shown in Figure 5.1. Second, a new case study is simulated with a floor aspect ratio of 2 (A_2 case). Only one stilt height case is adopted in the current study (2.15m). This stilt height is one of the group houses that experience severe damages during hurricane events, according to Ibrahim et al. [75]. This study contributes to understanding the transient flow through an elevated house and investigating the effect of increasing the aspect ratio and the number of stilts on the flow shape and the resulting peak

pressures. More importantly, the numerical simulation carried out in this study provides important insights on the suitable modeling parameters for LES simulations of an elevated building. The chapter starts by presenting the model configuration and dimensions. Then, the computational domain dimensions, mesh size, and the adopted equations are explained in sections 5.2 and 5.3. A comparison study is included in section 5.4 to validate the CFD model using the results obtained experimentally from the WOW testing. The resulting flow streamlines and the mean wind velocity are presented in section 5.5. In addition, the resulting wind pressure coefficients and wind forces of the new case study are presented in section 5.5.

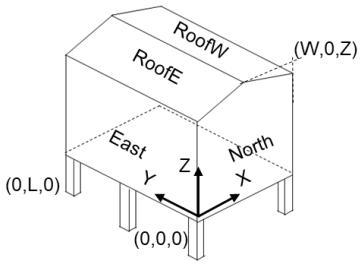

Figure 5.1 Elevated house schematic and the global axis

5.1 Model Description

The numerical modelling is conducted using a 1:5 length scale. The configuration of the validation model (A_1.36) is the same as the one-story elevated model tested at the WOW and explained in chapter three. As shown in Figure 5.2, the model is 1.75 m long and 1.28 m wide with a gable roof angle of 18º. The model stands on six stilts to raise the model by 43 cm above the ground level. The model configuration is explained in detail in section 3.1. The CFD simulation is conducted for three wind directions; 0º, 45º, and 90 (i.e., 0º wind direction parallel to the roof ridge). Next, the same data setup, scale, and boundary

conditions are used to simulate the case study model (A_2), as shown in Figure 5.2, using LES simulation. The scaled model dimensions are 1.5 m width x 3 m length with a gable roof angle of 18º. For the case A_2, the number of stilts is increased to 12 to assess the resulting effect on the pressure distribution along the floor surface.

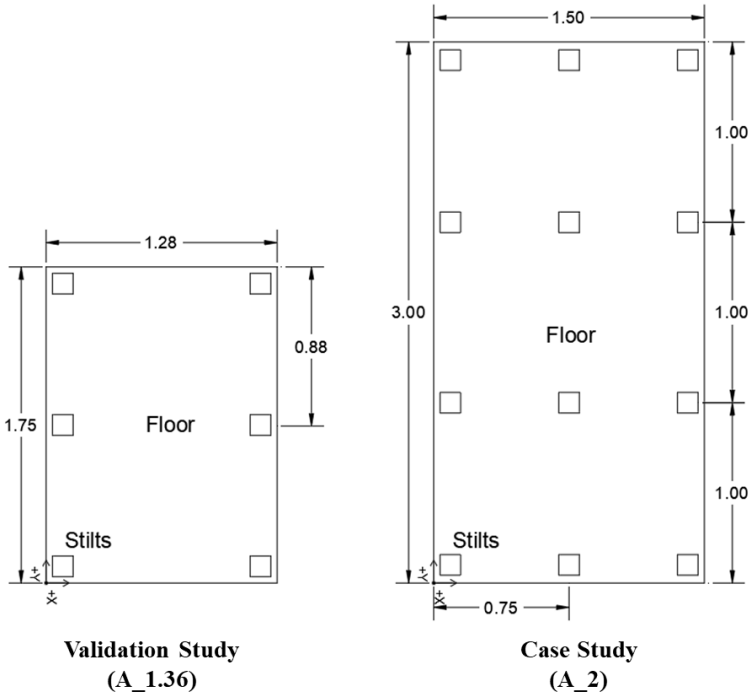

Figure 5.2 Floor surface of the elevated model scale (1-5) dimensions in (m)

To ensure the quality of the computational model, the simulation is conducted through three steps; (1) simulation of the Atmospheric Boundary Layer (ABL) before adding the model to compare the wind profile and turbulence characteristics with the WOW replicas, (2) simulation of the validation model (A_1.36) to compare the resulting pressure coefficient and distribution with the experimental results (Figure 5.3 a), (3) simulation of the new case study (A_2) (Figure 5.3 b). ANSYS fluent software is used to conduct the

LES numerical simulation at the three stages to simulate the velocity fluctuation with time and the resulting pressure-time history.

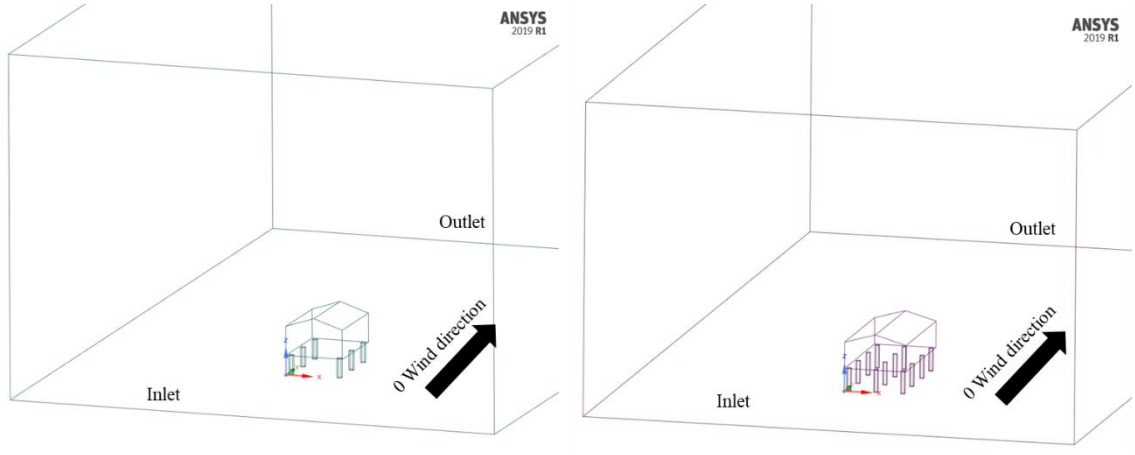

(a) (b)

Figure 5.3 3D computational domain (a) validation model, and (b) case study model

5.2 Governing Equations

Using ANSYS Fluent v19, the fundamental fluid equations are applied as explained in chapter four, section 4.2. Turbulent flow includes a wide range of length and time scales. The large eddies are more challenging to solve than the small eddies, which tend to be more isotropic. Using LES in Fluent, the filtration separates large eddies and solves them directly using the governing equation. The effect of the small eddies is taken into consideration using the grid model. These features allow LES to be a better tool for simulating the complex ABL flow and wind effect on structures.

After applying the filtration on the Navier-Stokes equation, the governing equation is as shown in Equation (5.1). Where, fluid velocity, pressure, time, location, and dynamic viscosity variables are donated by u, p, t, x, and μ, respectively.

$$\rho\left(\frac{\partial \bar{u}_i}{\partial t}+\frac{\partial(\bar{u}_i\bar{u}_j)}{\partial x_j}\right)=-\frac{\partial \bar{P}}{\partial x_i}+\mu\frac{\partial}{\partial x_j}\left(\frac{\partial \bar{u}_i}{\partial x_j}\right)-\frac{\partial \tau_{ij}}{\partial x_j} \quad (5.1)$$

The subgrid Reynolds stress τ_{ij}, defined in Equation (5.2), is modeled using sub grid scale model (SGS).

$$\tau_{ij} = \rho(\overline{u_i u_j} - \overline{u_i}\,\overline{u_j}) \tag{5.2}$$

For the current study, Wall-Adapting Local Eddy (WALE) viscosity model is used to resolve the SGS part [76]. The WALE model is more practical than other SGS models as it modifies the SGS viscosity near the wall structure to account for the wall damping effect [76], [82]. The WALE model is proven to work better than Dynamic Smagorinsky Model (DSM) model to simulate ABL when compared to experimental results and Direct Numerical Simulation (DNS) [78], [79]. However, it needs local mesh refinement near the model surface to precisely simulate the effect of walls in damping the flow [78]. Another advantage of the WALE model is that it does not require any explicit filtering [77]; therefore, it depends only on the locally provided information of the flow and walls to get the eddy viscosity [78]–[81].

In this model, turbulent eddy viscosity ν_t is used to model the small-scale turbulence, and it can be calculated using Equation (5.3).

$$\nu_t = (C_w\,\Delta)^2\,\frac{\left(\mathcal{s}^*_{ij}\,\mathcal{s}^*_{ij}\right)^{3/2}}{\left(\bar{S}_{ij}\bar{S}_{ij}\right)^{5/2} + \left(\mathcal{s}^*_{ij}\,\mathcal{s}^*_{ij}\right)^{5/4}} \tag{5.3}$$

Δ is the subgrid length scale, and C_w is a constant taken as 0.5.

The velocity gradient tensor $\mathcal{s}^*_{ij} = \frac{1}{2}\left(\bar{g}^2_{ij} + \bar{g}^2_{ij}\right) - \frac{1}{3}\delta_{ij}\bar{g}^2_{kk}$, and $\bar{g}_{ij} = \frac{\partial \overline{u}_i}{\partial x_i}$ (5.4)

The rate of strain tensor for the resolved scale $\bar{S}_{ij}$ is defined using Equation (5.5).

$$\bar{S}_{ij} = \frac{1}{2}\left(\frac{\partial \overline{u}_i}{\partial x_j} + \frac{\partial \overline{u}_j}{\partial x_i}\right) \tag{5.5}$$

5.3 Computational Domain and Solver Settings

The simulation is conducted in three-dimensional, considering an incompressible fully turbulent flow. To yield accurate results, no symmetrical reduction is applied to count for the air fluctuation in all directions. The domain dimensions are chosen to avoid any external effect through the domain walls [68]. As shown in Figure 5.4, the distance between the tested model and the inlet is taken as 5H, where H is the total height of the building. The height above the model is taken as 5H. The length behind the building till the outlet is taken 15H. The adopted dimensions allow the blockage to be less than 5% [69].

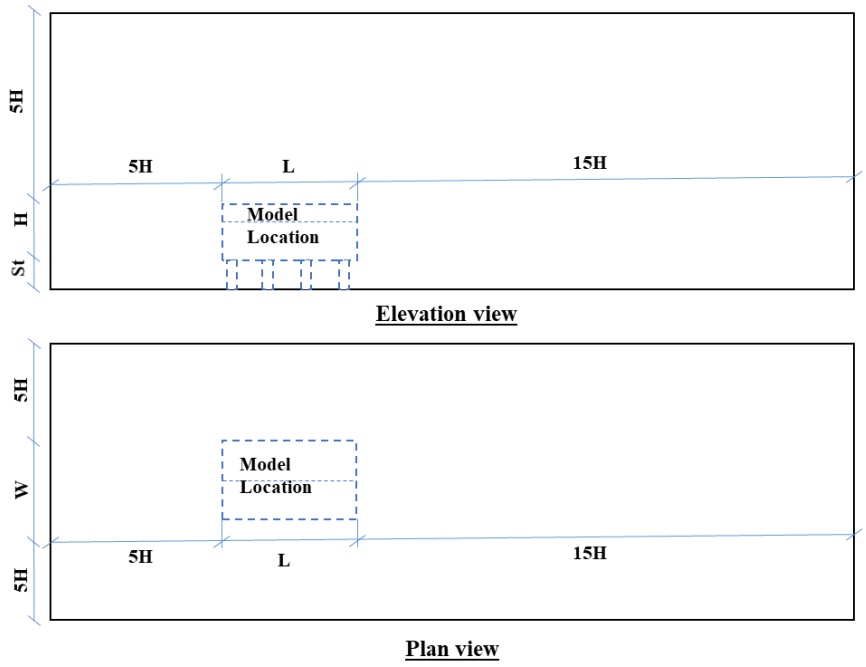

Figure 5.4 Computational domain dimensions

5.3.1 Domain meshing

All the boundary conditions should be carefully selected to describe the open terrain ABL. Reynolds-Averaged Navier–Stokes (RANS) simulation and RNG k-ε turbulent model are used to define the flow characteristics for the free stream LES model without adding the house. The domain is divided into layers in the vertical direction to adequately simulate the ABL. For the free stream RANS model, the domain is divided into around two million tetrahedral cells. The first layer's height is around 1mm, which kept the dimensionless wall distance (Y+) between 50 and 100. In the next step of defining the boundary conditions of the LES, Y+ is kept lower than 5 to resolve the viscous sublayer [61], [74].

For the computational domain with the elevated model, a structured tetrahedral grid is used to mesh the domain. Mesh sensitivity analysis is conducted on the validation case, between five different mesh sizes, starting from coarse mesh (1426121 cells) and reaching fine mesh (12395389 cells). Figure 5.5 shows the resulting average mean pressure coefficient for each mesh size. The objective is to ensure that the resulting data are independent of increasing the number of cells. The sensitivity study is applied using the 0º wind direction. As shown in Figure 5.5, starting from the medium mesh size (3651526 cells), the differences are negligible (below 1%) and the results are not affected by the mesh size. Therefore, considering the accuracy and the computational cost, the medium size mesh is chosen for the current simulation.

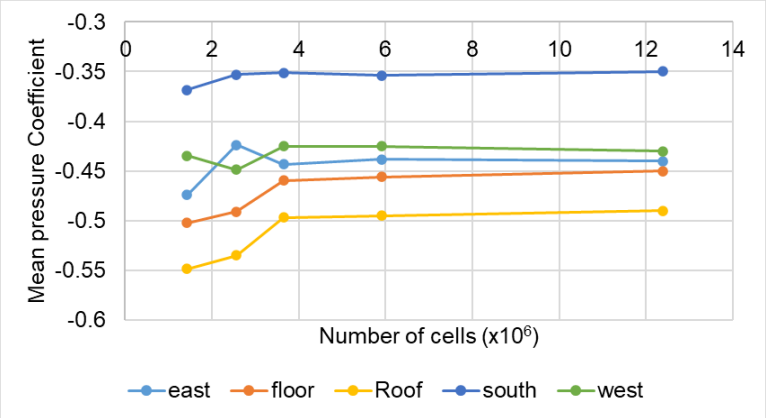

Figure 5.5 Mesh Sensitivity Analysis

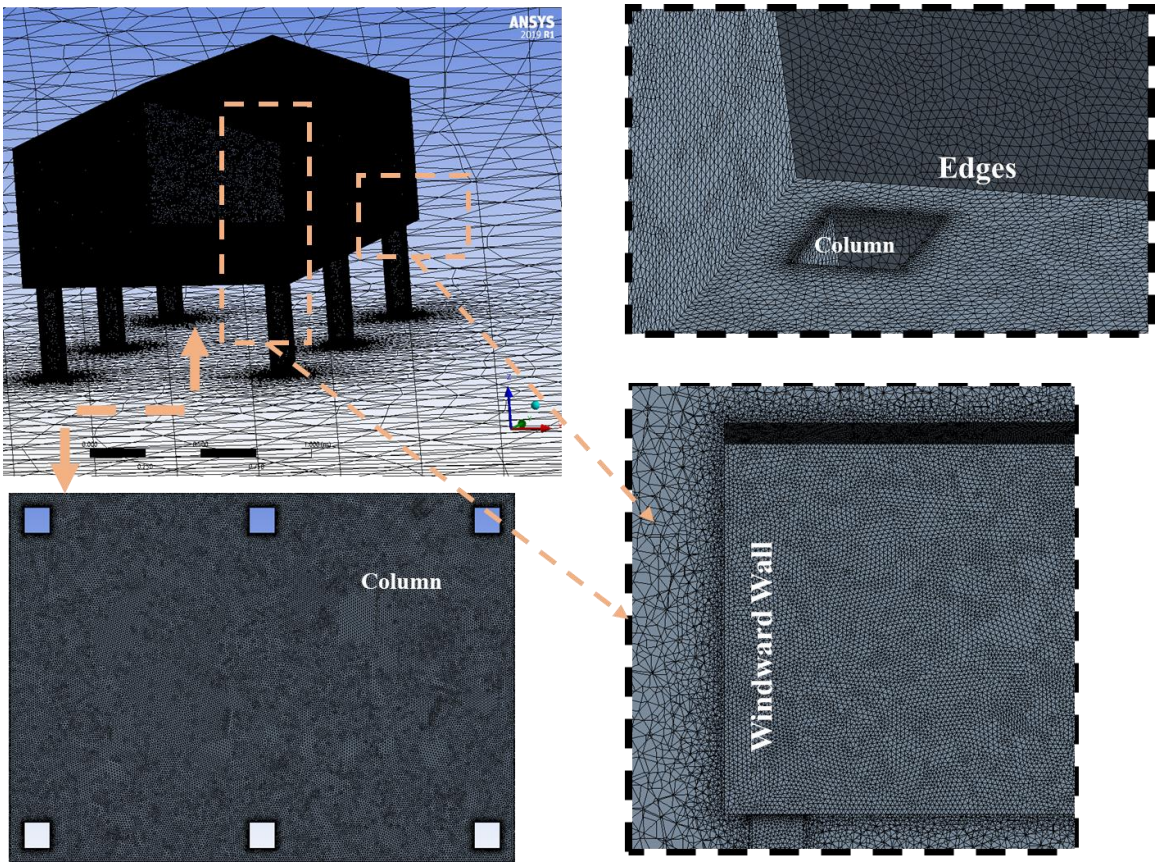

Figure 5.6 Computational domain mesh

For the chosen mesh size, a structured tetrahedral grid is constructed using small cell H/48 over the walls, and the rate of cell size increase does not exceed 1.2 [41], [68]. To use the WALE LES model, it is essential to use a fine mesh near the model walls to precisely resolve the near walls' viscous layers [78], [79], [81]. As shown in Figure 5.6, the mesh is refined using H/64 minimum size near the walls, along the stilt edges, and along the model edges to monitor the air flow around the model stilts.

5.3.2 Boundary conditions

The first step is defining the preliminary RANS model. Using the appropriate friction velocity (u^*), von Karman constant (κ=0.4), and roughness length (z_0 =0.016m), the ABL mean wind velocity U and the model turbulence are defined in the RANS model using the same criteria explained in chapter four (Section 4.4, Equations 4.9 – 4.13). All the outer walls are defined as slip walls, and the ground surface is defined as a rough wall using the roughness length as the prototype (z_0=0.016m). The roughness length is defined using input values; roughness height (C_s), roughness constant (K_s=0.5), and calculated using Equation (4.13) [54].

The next step is to define the resulting ABL using RANS model as a boundary condition of the LES WALE model to simulate the freestream of air without adding the elevated model. All other boundaries (i.e., walls, ground roughness, air flow parameters) are kept the same. In the LES model, the vortex method is used to define the flow fluctuation through the model [83], [84]. This method adds a perturbation to the mean wind profile at the inlet 2D plane. It is defined by setting up the number of vortices (N) entering the field through the inlet area (A). Then, each particle (i) is assumed to carry an amount of vorticity defined by its circulation (Γi) and spatial distribution (η). These parameters are calculated

using Equations (5.6 and 5.7). And the size of a local vortex is controlled by the parameter (σ), which is calculated using the defined k and ε parameters taken from the defined ABL, as shown in Equation (5.8).

$$\Gamma_i(x,y) = \sqrt[4]{\frac{\pi\, A\, k(x,y)}{3N[2\ln(3)-3\ln(2)}} \tag{5.6}$$

$$\eta(\vec{x}) = \frac{1}{2\pi\sigma^2}(2e^{-\frac{|x|^2}{2\sigma^2}} - 1)\, 2e^{-\frac{|x|^2}{2\sigma^2}} \tag{5.7}$$

$$\sigma = \frac{ck^{3/2}}{2\varepsilon} \tag{5.8}$$

where, c is a constant taken as 0.16, and σ is also controlled by the local mesh size. This method has shown more successful agreement with full-scale mean and peak pressure data than the scaled wind tunnel test, as noticed by Aly et.al. [74].

5.3.3 Solver setting

ANSYS Fluent is used to perform the numerical simulation. Naiver Stokes and continuity equations are solved using the control volume method. The equations of the transient formulation are discretized using a second-order implicit scheme. In the implicit scheme, the model parameters are dependent on each other, unlike the explicit solution. Using an implicit scheme makes it harder to reach the target accuracy of the model and needs a smaller time step, which adds more computational cost. However, this solution is more stable than the explicit method [85], [86]. In order to provide an accurate simulation while depending on the locally defined parameters, WALE subgrid model is used in the current study [78]–[81]. This scheme was used by Aly et al. to simulate low-ride building and showed accuracy in the mean and peak pressures compared to experimental results [74].

The transient simulation uses time step (Δt) 0.0004 sec to keep the Courant number (Equation 5.9) less than 1. The LES model parameters are summarized in Table 5.1.

$$Courant\ Number = U\frac{\Delta t}{\Delta x} \tag{5.9}$$

Table 5.1 Numerical simulation parameters

Property	**Setting**
Solver	Pressure Based Transient
Viscous model	LES
Inflow fluctuation	Vortex method
SGS	WALE
Minimum cell size	H/64
Rate of cell size increase	<1.2
Y^+	<5
Velocity at the inlet	RANS model
Domain ground	0.0016m roughness
Model walls	wall
Pressure velocity coupling	SIMPLE
Momentum	bounded differencing scheme
Pressure	Second-order
Transient scheme	Bounded second-order implicit
Simulation time	10 seconds
Time step Δt	0.0004 second
Courant Number	<0.75
Convergance Criteria	10^{-5} to 10^{-7}
Pressure Under Relaxation Factor	0.3

The resulting velocity and pressure time history are recorded using frequencies 2500 and 500 HZ, respectively. Figure 5.7 shows the resulting mean wind profile inside the computational domain, at the model location, compared to the recorded mean wind speed inside WOW facility, where U_{ref} is the mean wind speed at the reference height (Z_{ref}= 2m). Iu is the turbulence intensity after applying PTS, as explained in chapter two (Section 2.3). The agreement between WOW and CFD wind profiles is a good indication of a successful

simulation. However, a validation study to compare mean and peak pressure coefficients is needed to examine the accuracy of the results.

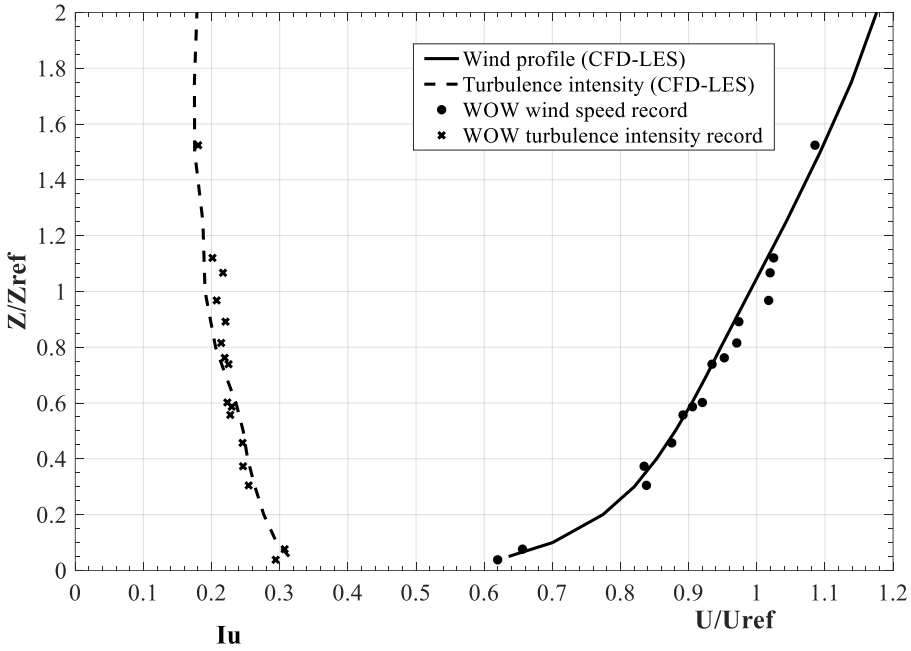

Figure 5.7 Mean wind speed and turbulence intensity profile comparison

5.4 Validation Study

A validation study is conducted using the meshing criteria, boundary conditions, and solver settings discussed in section 5.3. The one-story 2.15 m elevated model tested at the WOW EF (full scale) is adopted for this study. The model is simulated using a scale of (1:5), the length scale used for the WOW experimental test. The model configuration and dimensions are the same as the experimentally tested model shown in Figure 5.8.

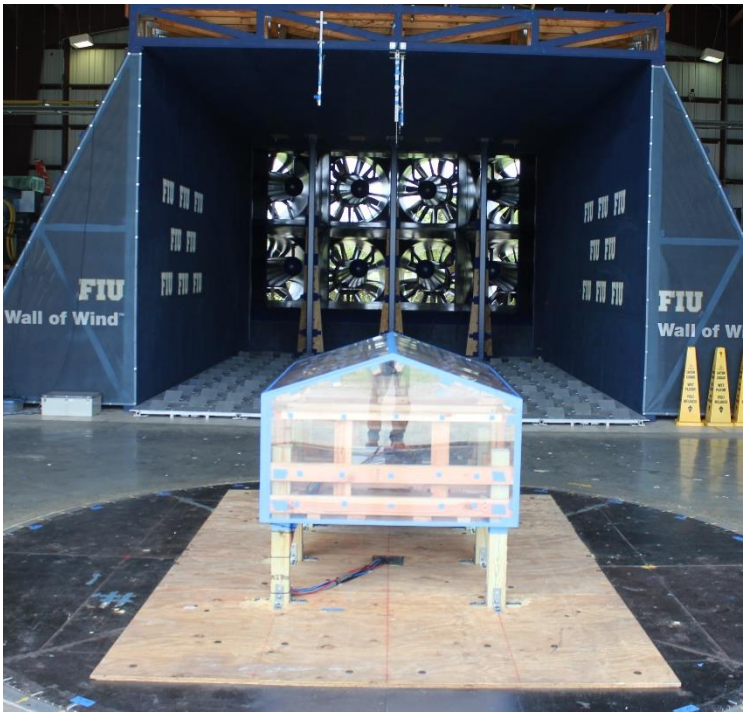

Figure 5.8 One-story 2.15 m elevated model inside WOW

The simulation is carried out for three different wind directions (0º, 45º, and 90º) for 10 seconds each. After finishing the simulation, the mean and peak pressure coefficients (C_{pmean} and C_{pmin}) are calculated from the recorded time history [87]. Figure 5.9 compares the C_{pmean}, over the floor surface, from the CFD model with their counterparts from WOW testing. A slice is taken parallel to the wind direction, for the 0º and 90º wind cases, and at the longitudinal and transverse directions for the 45º wind case, to provide a more detailed comparison along the model surfaces. Figure 5.10 shows the C_{pmean} variation along the section line. The figure includes a schematic drawing to show the section line using a dashed line, and the direction is indicated using arrows. These section lines start with the windward wall, roof, leeward wall, and finally, the floor surface. In the graph, the distance of each pathline is normalized using its total distance.

Figures 5.9 and 5.10 show a good agreement with the WOW results. In the 0º wind direction, the deviation is around 5% and located at the central area of the roof and floor surface where the pressure gradient occurs. For the 45º wind direction, CFD C_{pmean} is slightly higher, especially on the floor surface which shows 10% higher C_{pmean}. However, both show the same pressure gradient. The agreement in the 90º wind case is much better; the floor high suction regions are well simulated using CFD. In General, using the LES, the agreement in the C_{pmean} is better than the RANS model presented in chapter four.

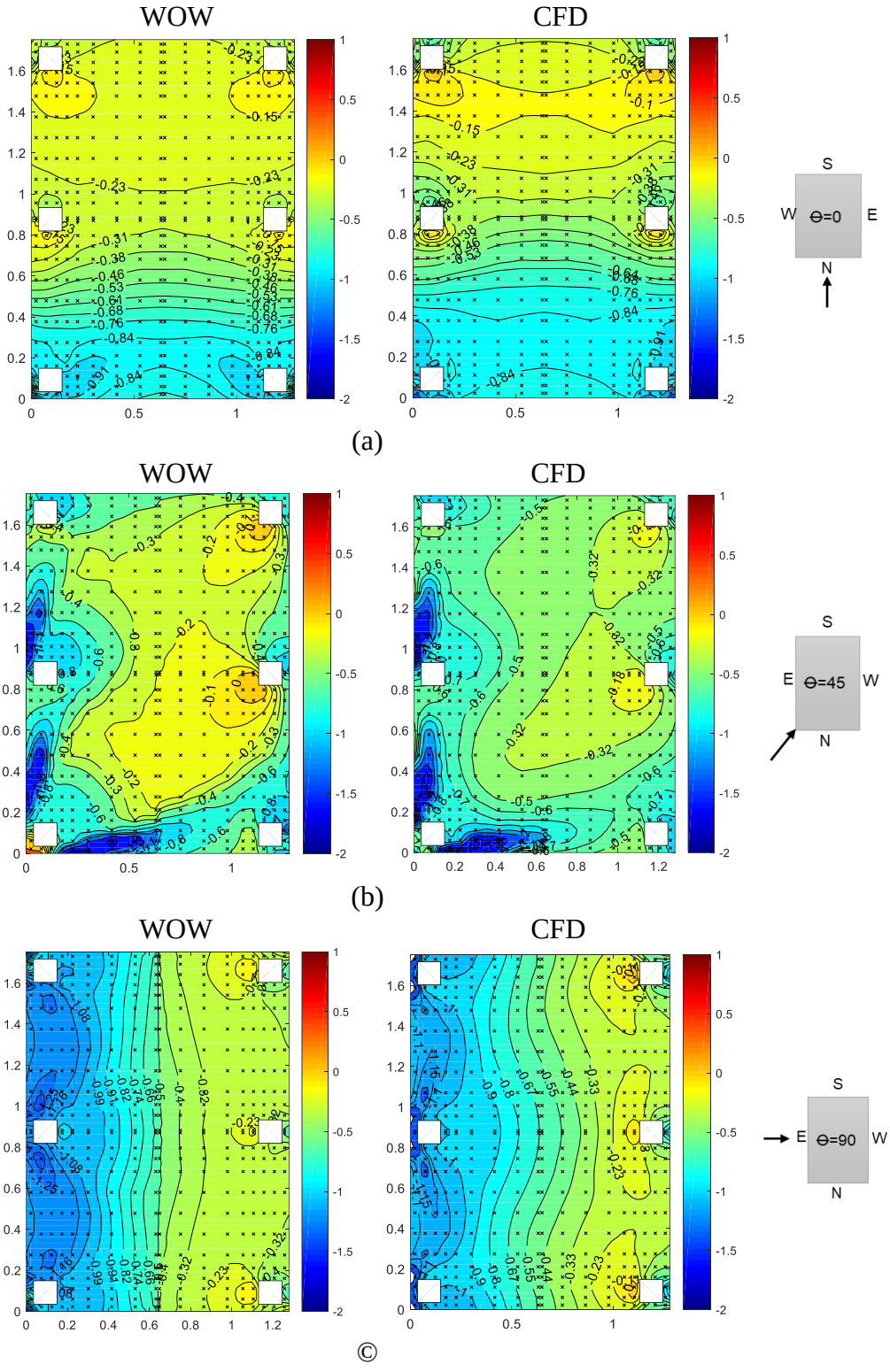

Figure 5.9 Local C_{pmean} comparison between CFD and LES on the floor surface (a) 0º wind direction, (b) 45º wind direction, and (c) 90º wind direction

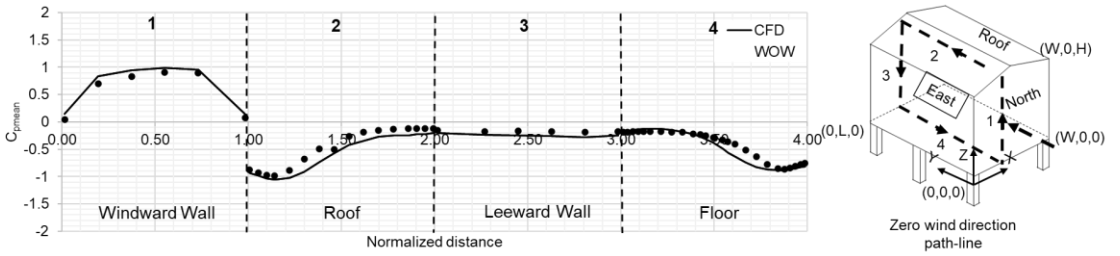

(a)

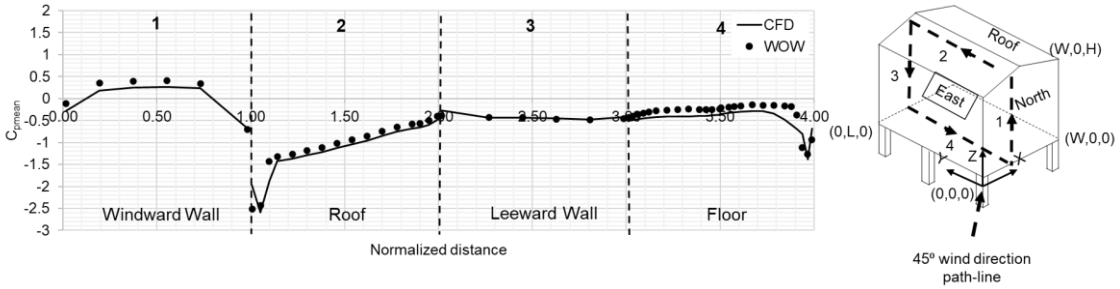

(b)

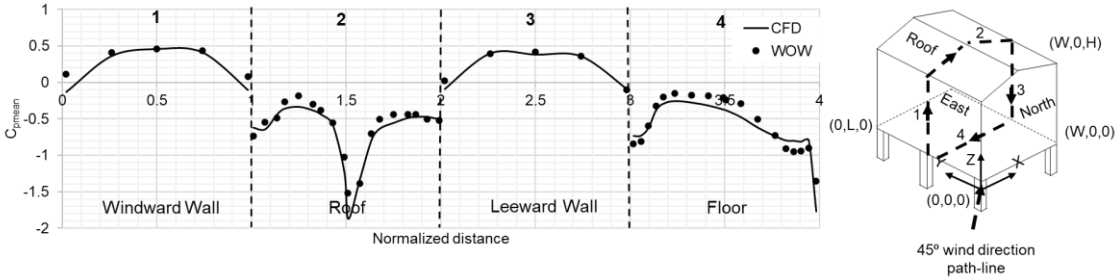

©

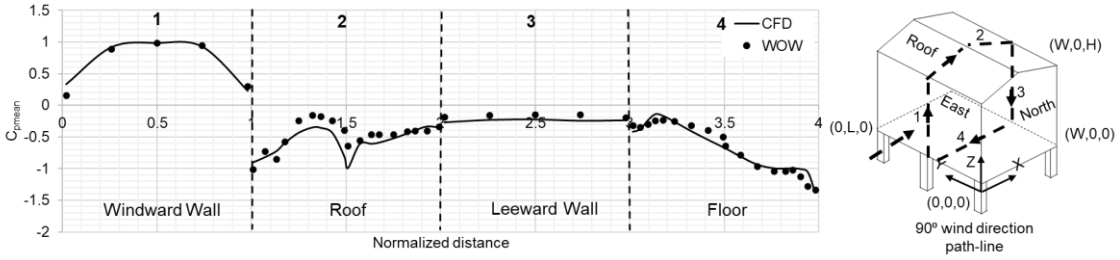

(d)

Figure 5.10 CFD and WOW resulting C_{pmean} along the section lines (a) 0º wind direction, (b) 45º wind direction longitudinal section line, (c) 45º wind direction transverse section line, and (d) 90º wind direction

Figures 5.11 and 5.12 show the resulting peak C_{pmin} extracted from the CFD output time series. For the C_{pmin} values, more deviations are noticed. The contour pattern is similar in CFD and WOW cases. However, the CFD model shows higher C_{pmin} values on the floor surface near the windward edges. The reason behind this is believed to be the usage of the vortex method to define the flow turbulence. This was also noticed by Aly et.al., who discovered a 12% deviation in the resulting peak pressure compared to full-scale field measurements [74]. In case of 0º wind direction, in the experimental and numerical cases, the C_{pmin} reaches -2.1 through the windward region of the floor surface and -2.6 near the stilts. However, the numerical model shows a larger region of the high suction than that for the WOW results. The plot in Figure 5.12a shows that the higher suction occurs at the leeward wall and floor surface. Although, the agreement on the roof and windward surface is very good. This difference is also noticed in the 90º wind case. However, the agreement near the stilt is good and can also be observed in Figure 5.12d. The major difference is along the mid-span, where the C_{pmin} reaches -2.7 in the CFD model and -2.1 in the WOW model, as observed in Figure 5.11d.

The best agreement occurs in the 45º wind case. CFD model successfully simulated the high suction regions similar to the WOW. But, around the top right stilt, the C_{pmin} in the CFD model is -1, which is higher than the WOW model (-0.6). The shown agreement in the C_{pmin} is considered fairly sufficient to study the new case model.

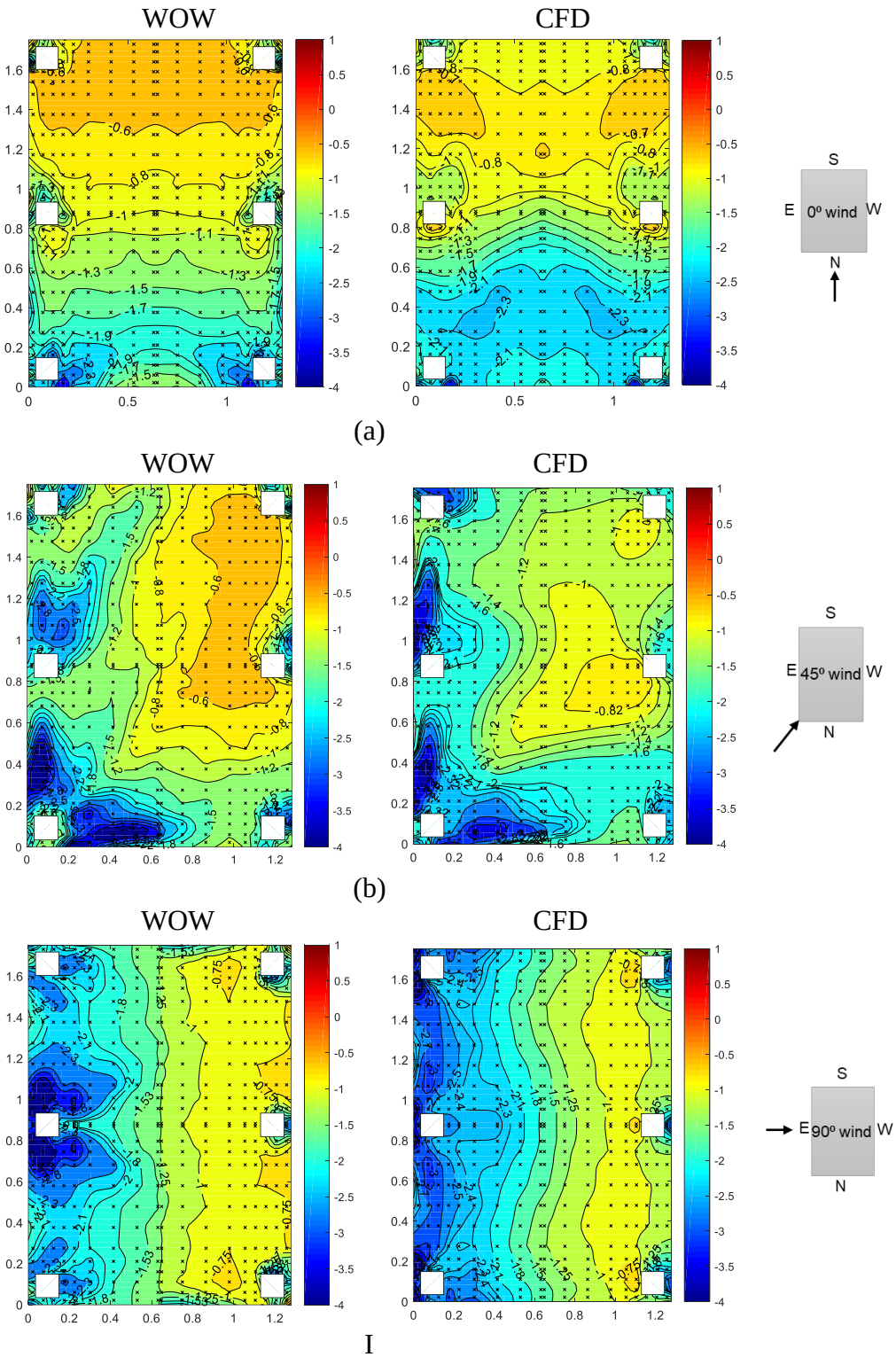

Figure 5.11 Local C_{pmin} comparison between CFD and LES on the floor surface (a) 0º wind direction, (b) 45º wind direction, and (c) 90º wind direction

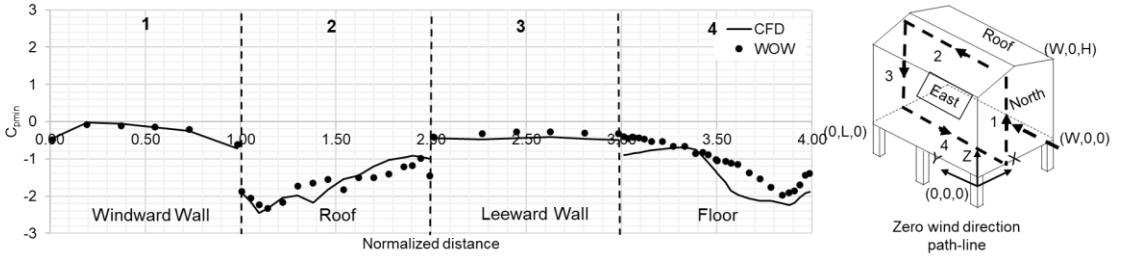

(a)

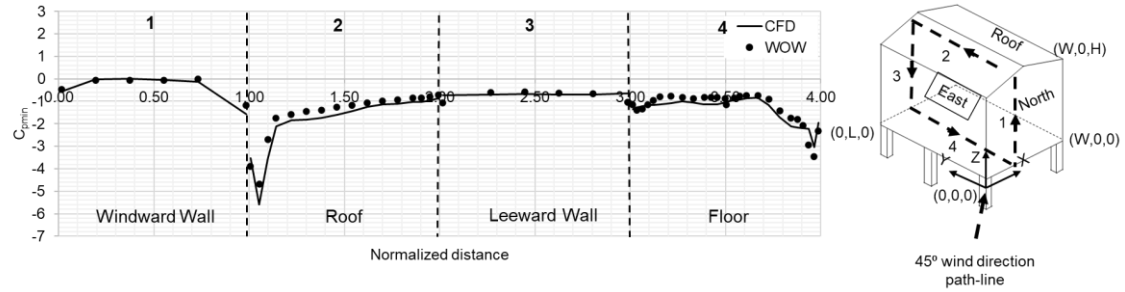

(b)

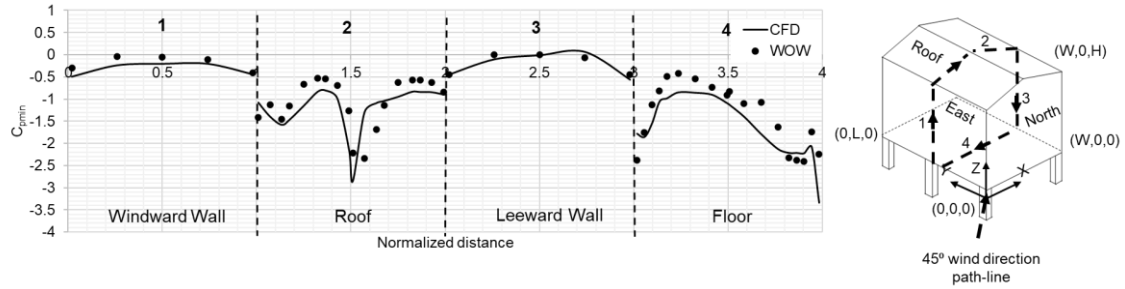

I

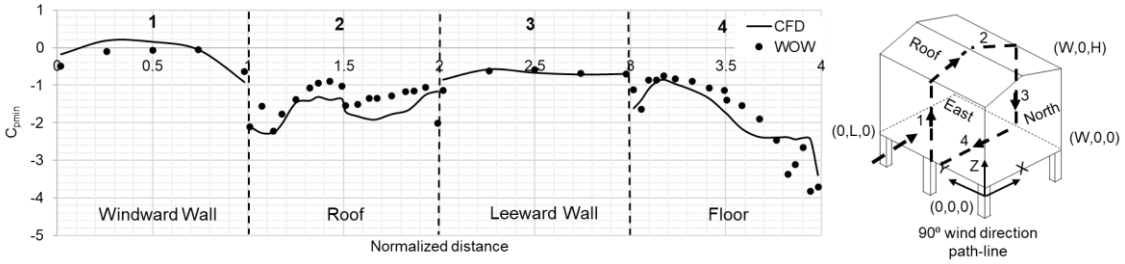

(d)

Figure 5.12 CFD and WOW resulting C_{pmin} along the section lines (a) 0º wind direction, (b) 45º wind direction longitudinal section line, (c) 45º wind direction transverse section line, and (d) 90º wind direction

5.5 Results and Discussion

The observed agreement of the validation study encourages the author to present the flow field properties and examine the new case study. The model scale, meshing criteria, boundary conditions and solver equations, which successfully work with the validation model, is used again to simulate the A_2 case standing on 12 stilts, as shown in Figures (5.2 and 5.3b). This section discusses the wind flow characteristics and the resulting pressure coefficients. First, the instantaneous flow streamlines are shown for the three wind directions. The mean velocity over the domain is presented to examine the effect of increasing the model floor aspect ratio. In addition, the influence of increasing the number of stilts on the wind velocity through the gap is also evaluated. Next, the mean and peak pressure coefficients are included to investigate how the new stilt pattern affects the resulting suction on the floor surface. Finally, the resulting total forces are discussed too.

5.5.1 Flow streamlines and wind profile

In chapter four, the resulting streamlines, averaged over time, revealed the significant effect of the air gap, the formed vortices in oblique wind directions, the wind flow increase through the gap, and the resulting high suction on the floor surface. Therefore, looking at the simulated cases' streamlines could verify or add to the previous findings. For instance, Figures 5.13 and 5.14 show the streamlines at the 5^{th} second of the flow simulation of the A_1.36 and A_2 cases, respectively. The figures show how the air flow speed is affected by its movement through a narrow passage. In the two aspect ratio cases and all wind directions, the velocity increases to more than 30m/s. The velocity increase is affected by the number of stilts. For instance, the 0^{o} wind flow in Figure 5.14 shows the decrease of the wind speed through most regions below the model due to the presence of more stilts

obstructing the flow and causing more flow turbulence. The figures also reveal the flow circulation in the downstream flow, passing the model stilts in all wind cases. The velocity dropped dramatically along the circulation to be -5m/s. The high-velocity gradient causes high suction on the flow surface, as observed in Figures 5.9 and 5.11. The velocity gradient is found to be higher in the oblique wind direction (Figure 5.13, 45º wind), which causes higher suction around the stilts, as noticed in Figure 5.11b.

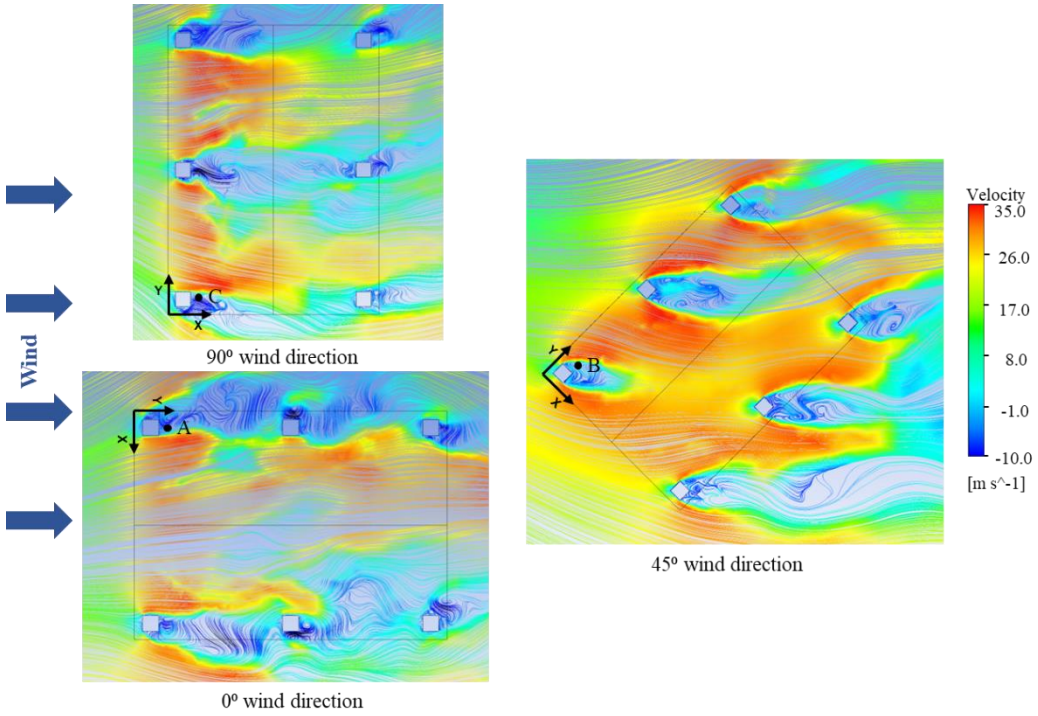

Figure 5.13 Flow streamlines below the floor surface for three wind directions A_1.36

These observations agree well with the findings of chapter four and the results reported by Amini et al. while testing the effect of increasing the number of stilts [61]. However, the turbulence observed in the current study is greater than the Amini et.al. results. The reason behind that is the defined flow turbulence, in the current study, which is the same

as the corrected profile after applying PTS to get comparable pressure coefficients that match WOW.

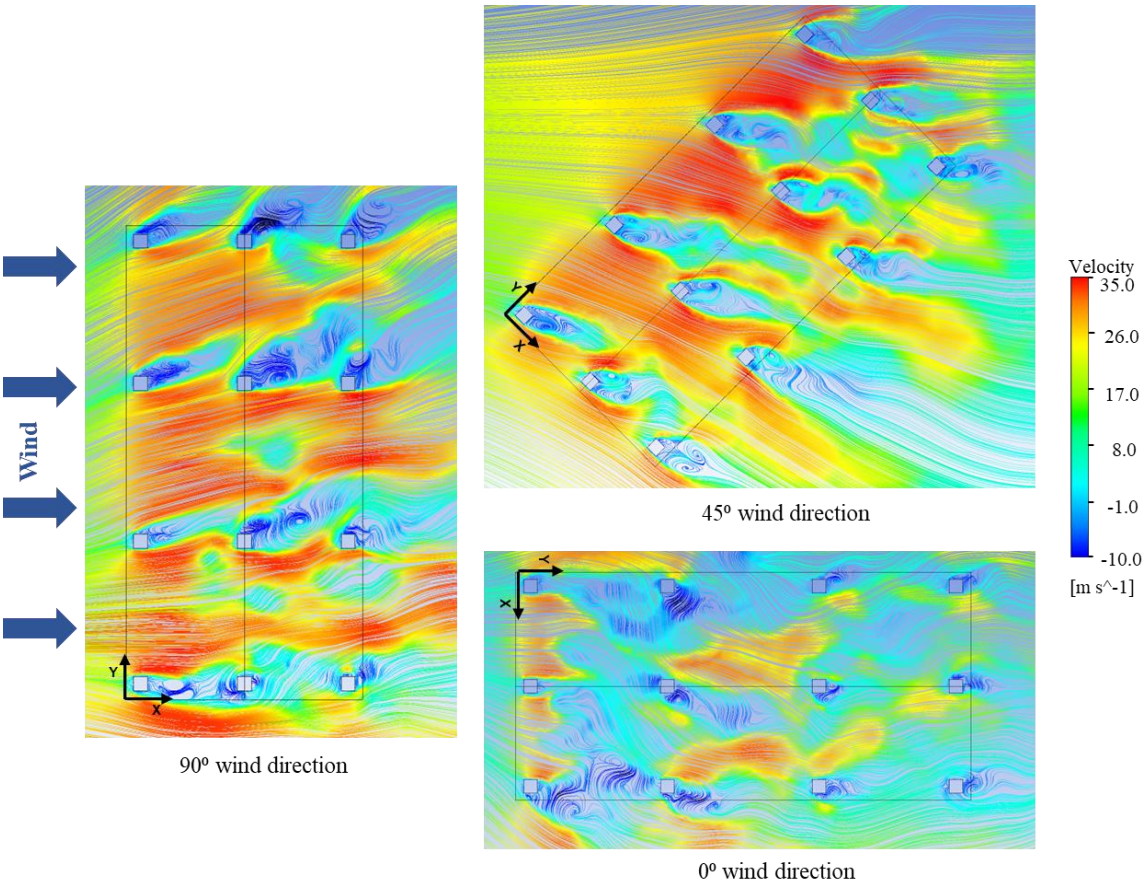

Figure 5.14 Flow streamlines below the floor surface for three wind directions A_2

The air circulation observed in figures 5.13 and 5.14 can be justified by monitoring the wind velocity near the stilts and verifying the formation of vortices. The vortex shedding frequency can be determined using the non-dimensional Strouhal number (St), as shown in Equation (5.10).

$$St = \frac{f\,D}{U} \tag{5.10}$$

where, f is the shedding frequency, D is the bluff-body size, and U is the flow velocity.

For the marked points A, B, and C (Figure 5.13), the velocity-time history is recorded below the floor surface of the A_1.36 case for the 0º, 45º, and 90º wind directions, respectively. These points are chosen where the air circulation is observed. The Power Spectral Density (PSD) curve is drawn from the recorded velocity fluctuation, as shown in Figure 5.15. The figure reveals the occurrence of vortex shedding at a frequency of 1 Hz for the 0º and 90º wind cases. For the 45º wind case, the shedding frequency is 2 Hz because the used velocity in the PSD is at local x, y directions, as shown in Figure 5.13. For the square column size (0.09m) with sharp edges, the St is assumed to be equal to 0.1. This justifies the formation of small vortices with size (D = stilt width) and moving at a very low speed of 0.5m/s. The natural frequency of this building in full scale (assuming its mass is 60 tons) ranges between 0.3 and 0.4 Hz, which is lower than the shedding frequency. This means that the shedding frequency passed the building vibration frequency, and the building acceleration may not increasing. However, because the elevated buildings are considered to be flexible (i.e., with the natural frequency less than 1 Hz), wind-induced dynamic effect may dominant the response of the structure. Thus, further in-depth studies focusing on assessing the vibration of elevated builings are necessary.

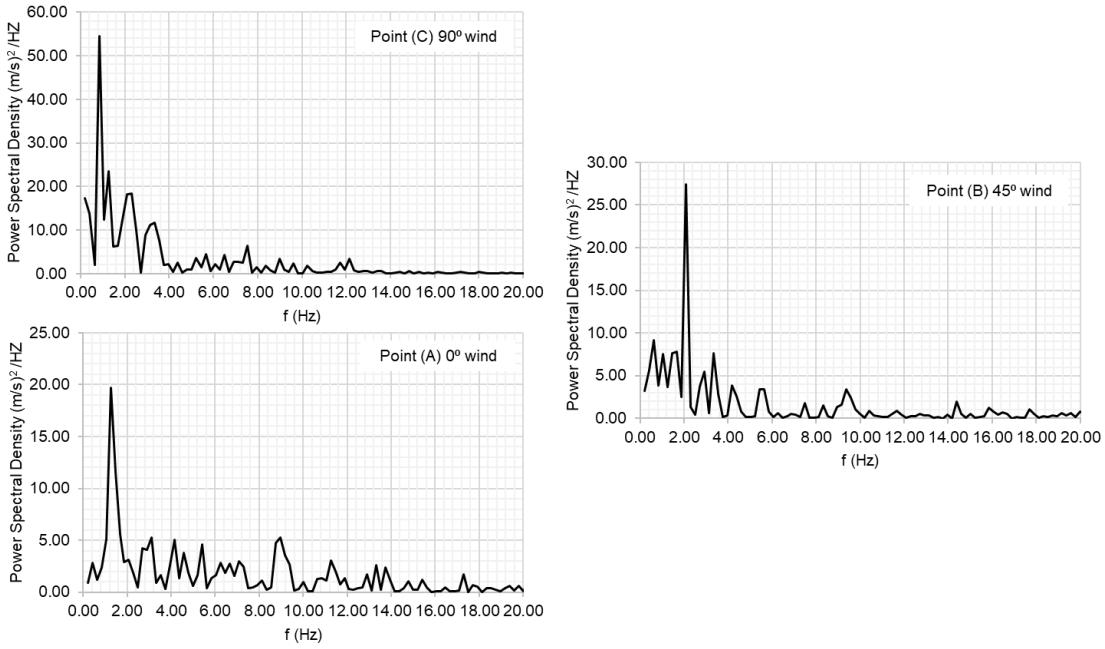

Figure 5.15 PSD curve for the velocity fluctuations for three wind directions A_1.36

Another observed phenomenon from the RANS model parametric study is the wind velocity increase through the air gap. This phenomenon is also observed in this chapter using the LES model. To examine the variable affecting the wind speed increase, a contour plot of the mean wind speed (U) at the mid-span section is extracted from the CFD simulation and presented in Figure 5.16 (a and b). In addition, the figure includes a plot of U variation with length at 0.2m height in the LES model (1m in full scale). In the plot, U is normalized using the mean wind speed at the inlet (U_{inlet}), and the distance is normalized using the model length along the wind direction. From the figures, at 1m in full-scale, the U_{inlet} is equal to 14m/s and after moving through the air gap, U reaches 27.8m/s, which is twice the inlet mean wind velocity. Then the mean velocity drops gradually to 80% U_{inlet} and returns to the average velocity after moving twice the building length in the 0º wind

case. The concentration of the high-velocity region at the first span is not much affected by the model length. Figure 5.17, for the A_1.36 case, reveals the same observation. However, the only case where the wind flow is obstructed by a large wall surface is the 90º wind direction of A_2 case. In this case, the wind velocity increase is 225% of the U_{inlet}. The plot in Figure 5.16a also shows that the wind speed is affected by the presence of stilts where the flow speeds by 20% then drops after passing the stilts.

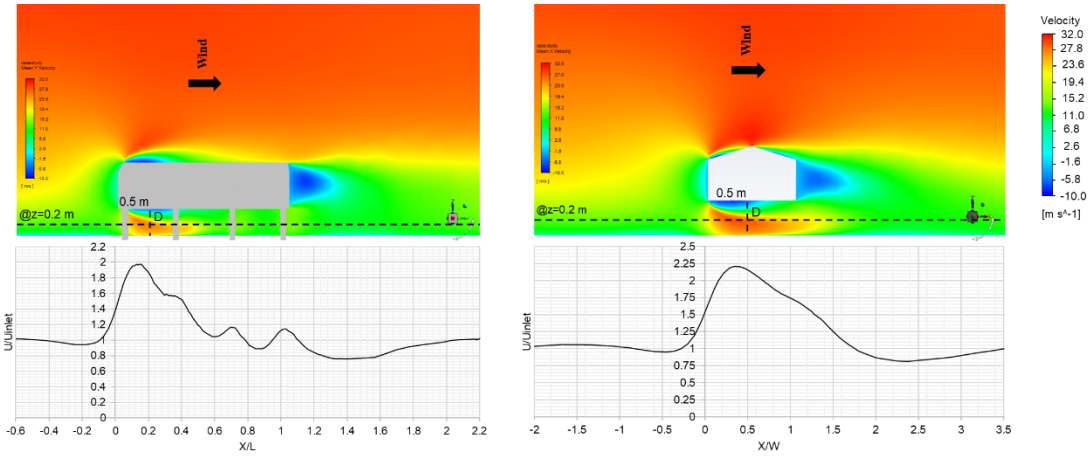

(a) (b)

Figure 5.16 Mean wind velocity variation for A_2 (a) 0º wind direction, and (b) 90º wind direction

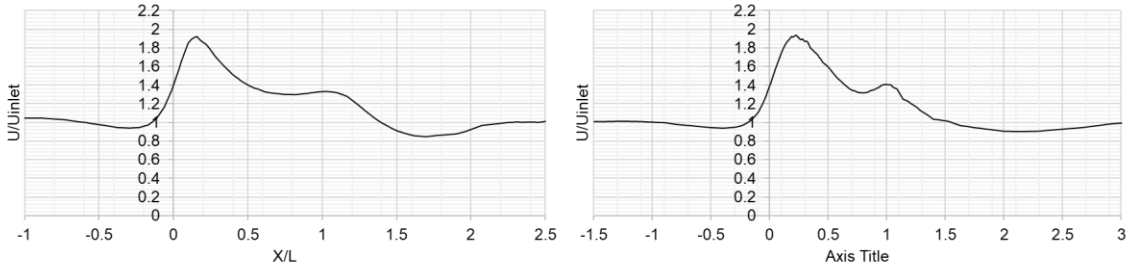

(a) (b)

Figure 5.17 Mean wind velocity variation for A_1.36 (a) 0º wind direction, and (b) 90º wind direction

Along the vertical direction, Figure 5.18 shows the mean wind speed (U_{gap}) variation with the gap height (Z_{gap}) (i.e., line D), as shown in Figure 5.16. These plots show a clear comparison for A_2 with the U_{inlet} for 0º and 90º wind cases. The figures show that the increase of the windward area adds a 15% increase to the mean wind speed below the house's floor surface. This observation is needed to emphasize the importance of clearing the empty ground area during strong wind events.

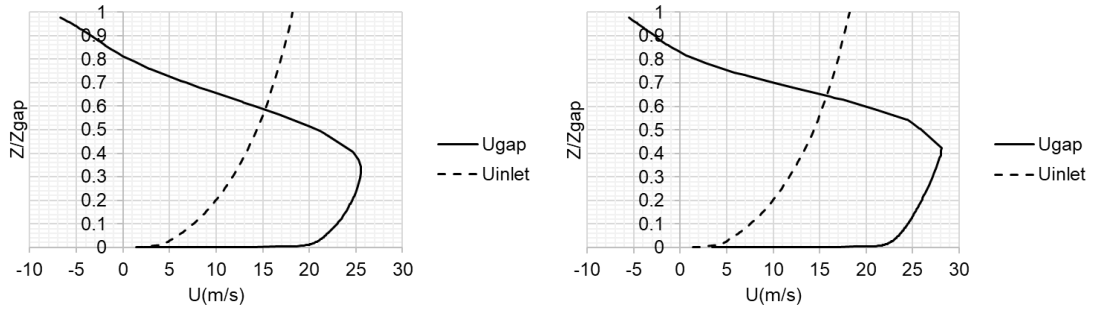

Figure 5.18 Mean wind velocity profile below the model floor compared to the inlet profile for A_2 (a) 0º wind direction, and (b) 90º wind direction

5.5.2 The resulting pressure coefficients of the new case study

From the 10 seconds simulation of the A_2 model, C_{pmean} and C_{pmin} are calculated and presented in this section. The C_{pmin} values are extracted from the resulting time history using the approach introduced by Sadek et al. [87]. Figure 5.19 presents the resulting coefficients on the floor surface for the 0º wind case. The figures reveal the presence of a new suction region (C_{pmin} = -1.1) between the intermediate stilt and the floor edge. This high suction region extends at the two sides of the stilt due to the velocity gradient noticed from the flow streamlines. In the C_{pmin} the suction region reaches -2.5, nearly the same

value observed in the A_1.36 model at the corners. For the leeward area, the C_{pmean} decreases gradually till it reaches the stilts. The suction tends to be zero at the upstream region of the stilts, and suction occurs again at the downstream region of each stilt (around -0.33). The gradual change in the C_{pmean} along the side edges is observed to be the same as for the A_1.36 case. The C_{pmin} over the third span is 20% higher in the A_2 case. However, it is nearly similar over the second span. Generally, the presence of stilts causes consequence separation and reattach of the flow. This is also concluded from the wind speed jumps noticed in Figure 5.16b. The same observation is noticed for the 45º and 90º wind cases in Figure 5.21. Every stilt added to the floor surface introduces high suction around it. And the C_{pmin} values are nearly similar.

Therefore, the comparison confirms that the suction mean or peak coefficients are not significantly affected by the floor aspect ratio. But the location and the area of high suction region are significantly affected by the stilt location. The less is the span length, the more is the high suction scatter. The high suction area distribution change is the reason behind the total suction force increase concluded in chapter four.

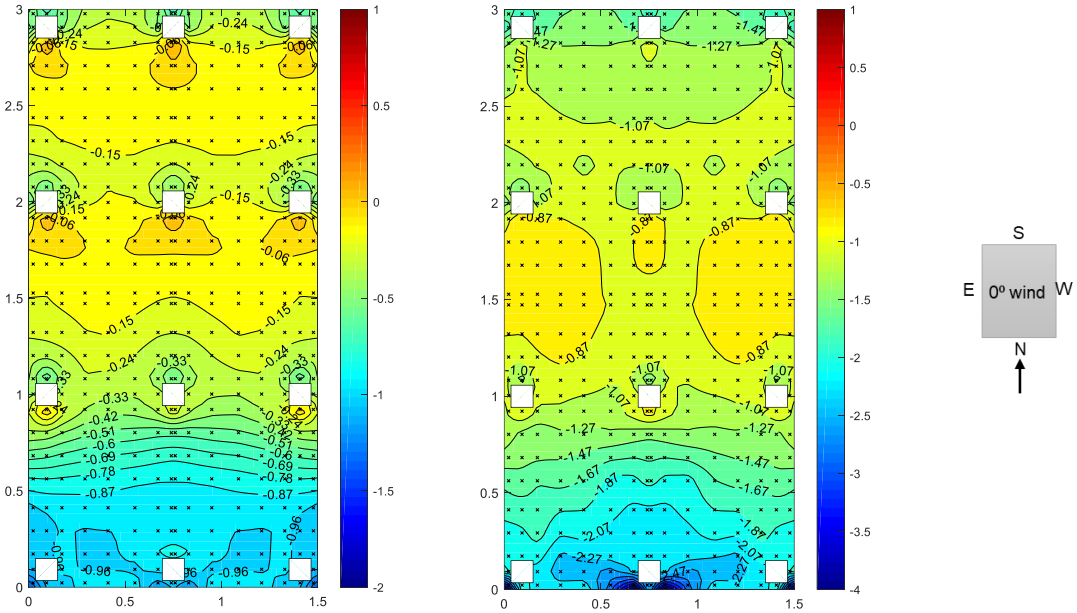

(a) (b)

Figure 5.19 Pressure coefficient distribution on the floor surface for 0º wind direction (a) C_{pmean}, and (b) C_{pmin}

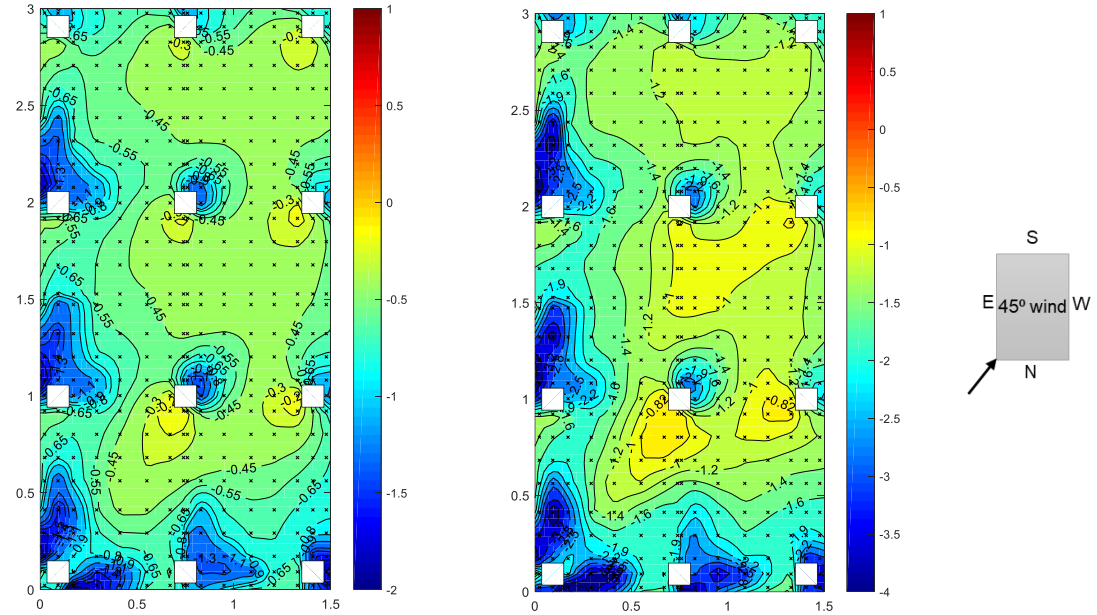

(a) (b)

Figure 5.20 Pressure coefficient distribution on the floor surface for 45º wind direction (a) C_{pmean}, and (b) C_{pmin}

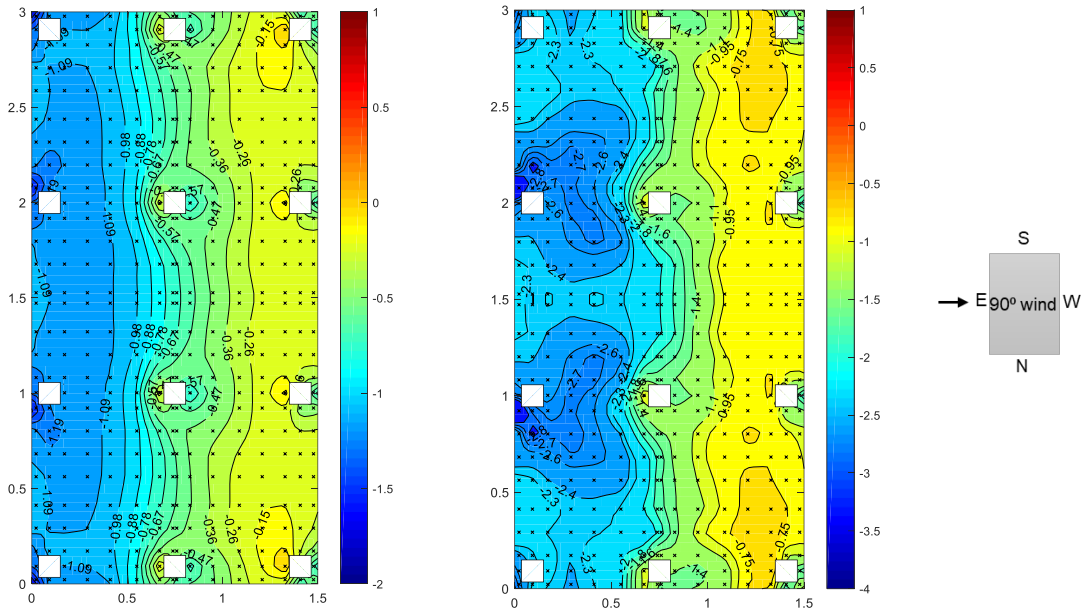

(a) (b)

Figure 5.20 Pressure coefficient distribution on the floor surface for 90º wind direction (a) C_{pmean}, and (b) C_{pmin}

5.5.3 Wind forces

As described in the previous chapters, the wind forces are strongly affected by the change in the elevated house configuration. Chapter four concludes a considerable increase in the vertical forces acting upward, which needs more investigation. For the Walls, roof, and floor, the average force coefficients time history over the face is extracted from the CFD simulation. From the extracted time history, mean and peak values of force coefficients are calculated. Then the percentage of the force coefficient increase (A_2 model divided by the A_1.36 model), per each surface, is calculated using Equation 5.11 and listed in table 5.2. The overall increase percentage of the shear and vertical forces are also calculated and shown in Table 5.3. The F_x and F_y stand for the shear forces in case of

90º and 0º wind directions, respectively. F_z stands for the total vertical force, whether positive ($F_z\uparrow$) or negative ($F_z\downarrow$).

$$CF_x\% = \frac{CF_{x,2} - CF_{x,1.36}}{CF_{x,1.36}} \; x \; 100 \tag{5.11}$$

$$F_x\ \%= \frac{F_{x,2} - F_{x,1.36}}{F_{x,1.36}} \; x \; 100 \tag{5.12}$$

In the 0º wind case, the mean force coefficients experience a slight decrease, after increasing the floor aspect ratio, which is considered a negligible change. No increase occurs in the larger aspect ratio case for the positive peak coefficients on the windward wall. 11% decrease occurs for the negative peak coefficients on the side walls of the A_2 case. The increase of force coefficients on the windward and leeward walls causes a 5% increase in the F_y, as shown in Table 5.3. The peak force coefficients on the roof and floor surfaces experience 4% and 2% increase, respectively. Due to the floor area increase, the total mean vertical force increases significantly by 173% upward. The worst cases for peak vertical force are; 41% increase upward or 63% increase downward.

For the 90º wind case, the wall surfaces do not experience a considerable increase in the force coefficients of the A_2 case. However, the negative peak forces coefficient decreases on the sidewall because the high suction region is only concentrated on the first span for all cases. A significant increase in the wall surface area causes a considerable increase in the total shear forces in case of 45º and 90º wind cases. For the floor surface, the observed increase in the high suction region around the new stilts, in the 90 wind case, causes 4% and 11% increase in the mean and negative peak force coefficients. The total mean vertical force on the foundation increases to be triple its value. This is observed too in case of oblique wind direction (45º).

The results shown in this section agree with chapter four findings. The increase in the vertical force is very significant for the larger floor aspect ratio. And by increasing the number of stilts, the increase becomes more considerable. The peak overturning moment, due to horizontal wind forces, besides the upward vertical force, are acting against the house stability.

Table 5.2 Mean and peak forces increase in the A_2 case compared to A_1.36 case per each surface

		Force coefficient increase over the surface			
	Wind direction	Roof	Floor	Wall (+ve)	Wall (-ve)
Mean	0	-3%	-2%	-2%	-2%
	45	0%	6%		
	90	9%	4%	1%	-3%
Peak (+ve)	0			0%	
	90			-4%	
Peak (-ve)	0	4%	2%		-11%
	45	13%	10%		
	90	8%	11%		-10%

Table 5.3 Mean and peak total shear and vertical forces increase in the A_2 case compared to the A_1.36 case

		Total force increase		
		F_x or F_y	$F_z\uparrow$	$F_z\downarrow$
Mean	0	5%	113%	
	45	19%	122%	
	90	14%		126%
Peak	0	3%	41%	63%
	45	42%	85%	107%
	90	60%	85%	55%

5.6 Conclusion

The LES model is chosen to investigate peak pressure coefficients numerically of different configurations of elevated structures. Preciously, LES has shown a great

performance in simulating low-rise buildings. This study investigates the instantaneous flow through the air gap and the resulting mean and peak pressure coefficients. Through a validation study, the boundary conditions have been precisely estimated to develop a similar flow as the experimental test at the WOW EF. The 2.15m one-story gable roof, presented in chapter three (1S-43), is adopted for the validation study using the same scale 1:5. Two different floor aspect ratios are compared; 1.36, and 2, standing on 9, and 12 stilts, respectively. The simulation is conducted for three wind directions; 0º, 45º, and 90º.

The validation study shows a good agreement in the resulting mean and peak pressure coefficients. The streamlines at five seconds show the increase of wind speed while entering the air gap. The wind speed drops down due to the presence of stilts and gets more turbulent. The flow streamlines present the formation of air circulation in the downstream region, due to the presence of stilts, for all the simulated wind directions. The PSD curve, drawn using the wind time history at the location of the air circulation, confirms the presence of vortex shedding.

This chapter demonstrates the mean wind speed over the domain along a mid-span section. The wind speed below the model floor is found to reach 200% of the wind speed at the same height in the inlet. It is also noticed that the windward area affects the wind speed increase; a 50% increase in the wall width adds a 25% increase in the wind speed. However, the increase of the model length along the wind direction does not affect the wind speed, but, it causes small speed jumps while passing through model stilts. This kind of observation is essential to be taken into consideration while designing a small structure, in the ground floor.

A comparison is conducted using the resulting mean and peak pressure coefficients of the A_1.36 and A_2 models. The increase of floor aspect ratio causes a slight increase in the suction area. However, the gradual change in the suction coefficients between the stilts and along the wind direction is similar in the two cases. For every new stilt, a new high suction region is introduced around each new stilt. This increase is believed to cause a considerable increase in the total vertical force after counting the floor area increase. The zoning scheme proposed in chapter three can be updated by adding new middle zones for every new stilt using the same pressure coefficient as the edge zone.

Compared to the A_1.36 case, the force coefficients on the walls are not significantly affected in the A_2 case. However, the resulting peak shear forces, for 45º and 90º wind cases, increase by 42% and 60%, respectively. A considerable increase is observed on the floor and roof surfaces. This increase in wind load on the floor underside cover and the structural system causes considerable damages during hurricane events. Besides the surface area increase, this increase leads to a total vertical force increase of 200%.

This chapter shows that LES is a successful tool to be used to observe the wind flow and the resulting peak pressure coefficients on elevated houses. However, more studies are required for the elevated houses to build a more dense aerodynamic database similar to that existing for on-ground low-rise buildings. For future work, it is recommended to study irregular shapes of houses and elevated houses with partially blocked floors to assess their aerodynamics.

6. CHAPTER VI

CONCLUSIONS AND FUTURE WORK

6.1 Summary of the Dissertation Findings

The ultimate goal of this dissertation is to provide an understanding of the main differences between the aerodynamics of elevated buildings and their on-ground replica. This is achived through investigating the role of the underside air gap in changing the wind flow through the structure using experimental and numerical simulations. First, a large-scale aerodynamic experimental study is conducted at the Natural Hazard Engineering Research Infrastructure (NHERI) Wall of Wind (WOW) Experimental Facility (EF) at Florida International University (FIU). The experimental program considers the on-ground case and commonly used stilt heights under varying wind directions. The program also includes a different number of stories (i.e., one-story vs. two-story elevated and on-ground homes). The experimental program results in an aerodynamic dataset for peak pressure time histories over the building surfaces. The resulting pressure-time history is used to evaluate the local peak and area average pressure coefficients on the roof, floor, and walls. In addition, the aerodynamic test program helps in identifying the high suction regions on the floor underside, which is hypothesized to be the main cause of failures during hurricanes and strong windstorms. The experimental pressure time history data is used to estimate wind loads on each building surface following the Components and Cladding design methodology from design standards. Second, the experimental program is complemented by numerical modeling using Computational Fluid dynamics (CFD) simulations to study the wind-structure interaction and assess the aerodynamic behavior of

elevated buildings compared to their on-ground counterparts. The CFD simulations include a parametric study, using Reynolds-Averaged Navier–Stokes (RANS) model, to evaluate the wind flow streamlines and the resulting mean forces for different stilt heights and floor aspect ratios. Moreover, Large Eddy Simulation (LES) model is also adopted to study instantaneous flow streamlines and the resulting peak pressure coefficients. More importantly, both the RANS and LES simulations and associated modeling parameters are validated against the experimental data. This is important contribution to the field of Wind Engineering as it can assist in future CFD studies of elevated structures.

From the experimental study, the local peak pressure coefficients (C_{Ppeak}) are calculated after applying the PTS technique, required for large scale wind tunnel testing peak pressure analysis, using the 3-sec wind speed at the roof mean height. Compared to their on-ground counterparts, the elevated models show no significant change in C_{Ppeak} values of the roof surface. The wall surfaces of the elevated cases experience lower positive and higher negative C_{Ppeak} at the lower edge due to the flow separation. High suction regions along the floor underside edges and around the stilts are observed.

The area-averaged pressure coefficients ($C_{P,\ avg,\ peak}$) for the roof surface of the on-ground case show a good agreement compared with the provided coefficients by ASCE 7-16 standard for a similar slab-on-grade building. The comparison shows higher values for the wall surface of the WOW models. Compared to the tested on-ground case, the elevated cases experience a slight change in the $C_{P,\ avg,\ peak}$ on the roof surface and lower $C_{P,\ avg,\ peak}$ on the wall surface. This comparison shows the applicability of using the provided pressure coefficient values of on-ground low-rise buildings, by ASCE 7-16, for the elevated cases roof only. For the wall surface, the author suggest to include the lower edge to the side

zones as it experience high suction in elevated cases. The wind speed increases due to the elevation increase should be considered because the resulting wind forces are expected to be higher for the elevated cases.

For the floor underside surface, based on the variation of the C_{Ppeak} over the surface, a zoning scheme is proposed. The proposed zoning scheme adopts an empirical equation that incorporates the stilt's width and height to calculate the width of the high suction zone at the edge of the floor. Based on the suggested zoning, the $C_{P,\ avg,\ peak}$ is calculated for the floor underside and is compared to flat roof external coefficients available in the ASCE 7-16 standard. This comparison shows the applicability of using the pressure coefficients provided by ASCE 7-16 for a flat roof to calculate wind forces on the floor underside surface of an elevated house where the reference wind velocity is taken at the mean roof height of the elevated house building. Otherwise, higher pressure coefficients should be used if the floor level is considered to be the reference height. These high-pressure values are provided in this dissertation.

While comparing different number of stories, the experimental results do not show a considerable effect between one-story and two-story elevated houses. The change in the C_{Ppeak} is slight and tends to be lower for the two-story case for the roof, walls, and floor surfaces. For the one-story elevated cases, the plot shows a considerable increase in the overall mean (global) uplift force on the roof surface and the floor underside as the stilt height increases. This floor suction, acting downward, is larger than the force acting upward on the roof surface.

From the RANS numerical simulations, the flow streamlines show the increase of the vortex size below the model floor as the stilt height increases. Also, the vortex size

decreases by increasing the model length. This leads to the concentration of the high suction at the windward edges of the floor surface. In the short stilt cases, the wind speed increases beneath the building floor due to the venture effect, a well-known phenomenon, occurring through the air gap. A flow circulation of the air took place between the intermediate stilts. The LES model provides enhanced data of the instantaneous flow streamlines, which clarifies the formation of vortices at the downstream region of each stilt for all wind directions. A high velocity gradient is also observed, which causes high negative pressure around the model stilts.

The resulting local mean pressure coefficients on the roof and floor surfaces, for the RANS model, are similar for different floor aspect ratios of the 2.15m elevated house, for 0º wind case (i.e., wind is parallel to the roof ridge). However, for 45º and 90º wind directions, the suction occurring on the roof surface and around the stilts on the floor surface is significant, especially when the aspect ratio is large. From the flow streamlines and the resulting pressure distribution, the study concludes that the higher suction along the edges is caused mainly due to wind acting perpendicular to the roof ridge. However, the wind acting in oblique directions is responsible for the high suction around the stilts. The total shear force of the building increases significantly as the stilt height increases while the total vertical force dropped by elevating the house due to the presence of a new force on the floor acting downward. By increasing the floor aspect ratio, the overturning moment and the vertical force significantly increases.

The LES numerical study adopts a 2.1m elevated house with a floor aspect ratio of 2 and stands on 12 stilts. This configuration is the most widely used in coastal areas based on recent damage survey studies. The model parameters are identified and experimentally

validated. The instantaneous streamlines at five seconds show a wind speed increase while the flow is entering the air gap. The wind speed drops down due to the presence of stilts and gets more turbulent. The mean wind speed below the model floor is found to reach 200% of the wind speed at the same height in the inlet. It is also noticed that the windward area affects the wind speed increase; a 50% increase in the wall width results in a 25% increase in the wind speed just after entering through the air gap. However, the increase of the model length along the wind direction does not affect the wind speed; it causes small speed jumps while passing through the model stilts. The comparison of the resulting mean and peak pressure coefficients in the LES models shows that the increase of the floor aspect ratio causes a slight increase in the suction area in all wind directions. However, adding new stilts introduces new high suction regions around each new stilt. This increase leads to a considerable increase in the total vertical force after counting the floor area increase.

Using LES viscous model with WALE subgrid model and vortex method to define flow turbulence, the mean and peak pressures are successfully simulated and are found in a good agreement with the experimental models.

The dissertation aims to show the controlling parameters and define their effect on the resulting wind pressures. The controlling parameters identified in this study are listed in the following bullets;

- Number of Stories.
  - The pressure coefficients over the roof, wall, and floor surfaces are lower by increasing the number of stories.
- Elevating low rise building over the ground level.

- Wind speed increases through the air gap, especially in small stilt cases (around 2m height)
- The average pressure coefficients decrease over the roof and wall surfaces for elevated cases.
- After elevation, suction wind force develops on the floor underside surface.
- The total vertical force decreases due to the new suction force on the floor surface.
- The total shear and overturning moment increase considerably due to the stilt height increase.

- Increasing the number of stilts
  - Around each new stilt, a new high suction region occurs on the floor surface.
- Increasing the floor aspect ratio
  - The total vertical force increases.
  - The wind flow speed increase through the air gap becomes more significant due to the increase in the windward wall surface area.

The conclusion of the current study justifies the observed damages to elevated buildings post-hurricane events. The wind speed increase due to the building height increase causes a typical failure in most coastal houses; cladding and cover removal. The presence of the air gap causes a considerable change in the wind flow streamlines. For instance, the flow separation at the lower edges causes typical wall and floor cover removal damage. The air circulation and the high wind speed gradient below the floor surface cause cladding removal around the columns and floor underside cover damage. Figure 6.1a shows a 50% of wall cladding removal only due to wind forces, during Hurricane Florence in North

Carolina. The suction affecting the floor underside surface causes cover removal, as shown in figure 6.1b. This kind of failure is critical and could lead to the change of the internal pressure and eventually lead to severe interior damage to the home. In the current numerical study, the noticed wind velocity increase is believed to be responsible for the damage to house attachments, as shown in figure 6.1b.

(a) (b) (c)

Figure 6.1 Cladding damages due to wind 2.2 m elevated houses (a) wall cover removal during Hurricane Florence in North Carolina, (b) floor cover removal during Hurricane Florence in North Carolina, and (c) floor cover removal during Hurricane Michael in Florida

As explained in the introduction, the damages shown are typical in most elevated houses along the coastline, as per post-hurricane survey reports. Therefore, by relying on the following recommendations, retrofitting existing buildings is essential to mitigate potential damage.

6.2 Design Recommendation and Future Work

6.2.1 General recommendation for the future design of elevated houses

The results provided in this study are used to develop several recommendations and to propose design guidelines to help enhance the available standards' provisions. This section includes a list of those guidelines to calculate wind loads on the cladding of elevated buildings. These recommendations are applicable only for the regular shape of gable roof

buildings as the ones presented in this dissertation. For other configurations of elevated buildings (i.e., larger number of stories, irregular shapes, and different roof types), more studies are encouraged to investigate their aerodynamic behavior.

- For low-rise building roof, the pressure coefficients used to design the cladding of the on-ground cases can be used in the elevated cases. However, a special attention should be paid to the consideration of the mean roof height of elevated structures as it affects the calculations of the wind forces on the surfaces, stilts, and foundations.
- For the wall surface, the zoning criterion and external pressure coefficients for on-ground low-rise buildings can be used for elevated houses with a modification. Since the lower edge of the wall is subjected to high suction, it is essential to use the high negative pressure coefficients provided in the codes for the side edges (zone 5 according to the ASCE standard) to design the lower edge of the wall surface.
- The floor surface should be divided into zones with respect to the stilt locations where the high suction zone is located to surround each stilt. The zone scheme proposed in chapter three can be used in case the building's stilts are located only at the edges. Otherwise, it is recommended to divide the floor surface into strips, as shown in figure 6.2 a, to consider the resulting high suction occurring around the stilts. The width of the zone "a" can be computed using the stilt height and the column size as explained in chapter three (Section 3.4.2/ Equation 3.2).
- After splitting the floor surface into zones, the pressure coefficients provided by ASCE 7-16 for a flat roof are applicable to be used to calculate wind forces, while

wind velocity should be taken at the mean roof height of the elevated building. Otherwise, higher pressure coefficients should be used if the wind speed is calculated at floor level. These higher pressure coefficients are provided in chapter three (Section 3.4.2).

- The numerical studies show that the high suction values, on the floor surface, are not considerably affected by the floor aspect ratio. Only the distribution of high suction regions is affected by the stilt location.
- The presence of an air gap causes a considerable increase in the wind velocity beneath the house that reaches 200% of the free flow speed. The presence of several stilts causes more turbulence in the flow. By increasing the windward wall area, the flow speed increase is more considerable. Therefore, any small structure or closed room located at the ground level should be designed considering this significant wind speed increase.
- Although the suction force acting on the floor surface is considerable, it does not cancel out the suction on the roof surface. The resulting vertical force primarily acts upward, affecting the stability of the building.

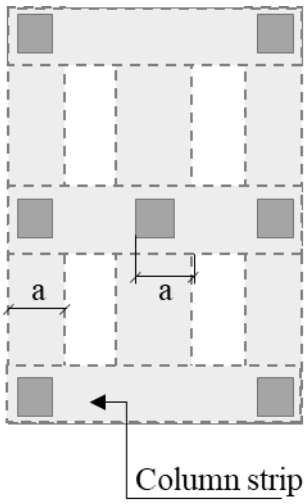

Figure 6.2 Proposed zone scheme on the floor surface with internal column strip

This year (2022), the newly released version of the American standard ASCE 7-22 is realsed and is showing new sections describing the wind flow effect on elevated houses component and cladding while considering the large-scale test findings reported in Chapter 2 of this dissertation [37], [38]. The new provisions are given for elevated houses with stilt heights larger than 0.6m. The new provisions use the same external pressure coefficients of low-rise buildings for the roof and walls of elevated cases. The pressure coefficients on the floor surface are considered the same as a flat roof surface. The adopted zoning scheme is the same as that for flat roof surface. However, the zone dimensions are calculated using the stilt height, which leads to underestimating pressure coefficients for small stilt cases and overestimating them for the large stilt case. As per the ASCE 7-22 provisions, for elevated buildings, it is recommended to use the velocity at the mean roof height to calculate the wind loads on components and cladding. This is proven to be sufficient in the current study (Chapter 3) for regular-shaped elevated buildings. The zoning criteria do not

include high suction zones for internal columns. For future verification and development of the available provisions, it is recommended to test tall elevated buildings (i.e., height of more than 18.3m) and partially enclosed elevated buildings.

6.2.2 Recommendations for the future studies

Generally, it is expected that the size, number, and locations of the stilts affect the resulting wind loads. Thus, more studies are needed to fill the current knowledge gap. In addition, other irregular shapes of elevated houses need to be studied to verify the applicability of the proposed scheme. It would be useful in the future to examine the effects of partially blocking the underneath of the building to study the peak pressures on elevated houses. The stairs attachment to the building didn't show a noticeable effect on the resulting pressure on the building surfaces, and it can be excluded from experimental testing to reduce time and cost. Future studies are encouraged to consider the simultaneous wind and wave actions on elevated buildings.

REFERENCES

[1] NOAA, “National Oceanic and Atmospheric Administration, Office for Coastal Management,” 2018.

[2] UN, “Engaging People to Protect the Planet.,” 2017.

[3] D. Hinrichsen, “Coasts in Crisis,” *Issues Sci. Technol.*, vol. 12, no. 4, pp. 39–47, Dec. 1996.

[4] NOAA, “Minor Modification to Saffir-Simpson Hurricane Wind Scale for the 2012 Hurricane Season,” 2012.

[5] M. Amini and A. M. Memari, “Review of Literature on Performance of Coastal Residential Buildings under Hurricane Conditions and Lessons Learned,” *J. Perform. Constr. Facil.*, vol. 34, no. 6, p. 04020102, 2020.

[6] R. J. Pasch, A. B. Penny, and R. Berg, “National Hurricane Center Tropical Cyclone Report, Hurricane Maria,” 2019.

[7] J. P. Cangialosi, A. S. Latto, and R. Berg, “National Hurricane Center Tropical Cyclone Report: Huricane Irma,” *Natl. Huricane Cent.*, no. September 2017, pp. 1–111, 2018.

[8] E. S. Blake and D. A. Zelinsky, “National Hurricane Center Tropical Cyclone Report, Hurricane Harvey,” no. 2005, pp. 1–77, 2018.

[9] A. Alipour *et al.*, “Hurricane Michael preliminary virtual assessment team (p-vat) report,” 2018.

[10] Artemis, “Hurricane Michael loss creeps to $7.2bn, but 17,347 claims still open,” pp. 1–2, 2019.

[11] C. Newmark and (RMS), “Hurricane Dorian Insured Losses in Caribbean from Wind, Storm-Surge. https://insurancejournal.com/news/international/2019/09/10/539310.htm,” 2019.

[12] T. Jeworrek, “Record hurricane season and major wildfires – The natural disaster figures for 2020,” 2021.

[13] B. Behnken and (NASA), “2020 Atlantic Hurricane Season,” *Center for Disaster Philanthropy’s (CDP)*, 2020.

[14] FEMA, “Recommended Residential Construction for Coastal Areas: Building on Strong and Safe Foundations. http://fema.gov/library/viewRecord.do?id=1853,” no. December, 2009.

[15] O. Bin, J. B. Kruse, and C. E. Landry, “Flood Hazards, Insurance Rates, and Amenities: Evidence from the coastal housing market,” vol. 75, no. 1, pp. 63–82, 2008.

[16] H. Kreibich, A. H. Thieken, T. Petrow, M. Müller, and B. Merz, “Flood loss reduction of private households due to building precautionary measures – lessons learned from the Elbe flood in August 2002,” *Nat. Hazards Earth Syst. Sci.*, vol. 5, no. 1, pp. 117–126, 2005.

[17] R. Gross, “Stilt Houses: 10 Reasons to Get Your House Off the Ground. http://redb.com/blog/2015/1/30/stilt-houses-10-reasons-to-get-your-house-off-the-ground,” 2015.

[18] T. Tomiczek, A. Kennedy, and S. Rogers, “Survival analysis of elevated homes on the bolivar peninsula after hurricane IKE,” *Adv. Hurric. Eng. Learn. from Our Past - Proc. 2012 ATC SEI Conf. Adv. Hurric. Eng.*, pp. 108–118, 2013.

[19] E. C. English, C. J. Friedland, and F. Orooji, “Combined Flood and Wind Mitigation for Hurricane Damage Prevention: Case for Amphibious Construction,” *J. Struct. Eng.*, vol. 143, no. 6, p. 06017001, 2017.

[20] L. Cochran, *Wind Issues in the Design of Buildings*. American Society of Civil Engineers, 2012.

[21] M. Amini and A. M. Memari, “Performance of Residential Buildings in Hurricane Prone Coastal Regions and Lessons Learned for Damage Mitigation,” in *5th Residential Building Design & Construction Conference*, 2020, no. March.

[22] P. MiraKijewski-Correa, Tracy; Alagusundaramoorthy *et al.*, “StEER - Hurricane Dorian: Preliminary Virtual Reconnaissance Report (PVRR).,” 2019.

[23] NSF, “The National Science Foundation (NSF), Network, and Structural Extreme Events Reconnaissance (StEER).,” 2019.

[24] J. D. Holmes, “Wind pressures on tropical housing,” *J. Wind Eng. Ind. Aerodyn.*, vol. 53, no. 1–2, pp. 105–123, 1994.

[25] J. D. Holmes and C. Osonphasop, “Flow behind two-dimensional barriers on a Roughened ground plane, and applications for atmospheric boundary layer modelling.” 8th Australasian Fluid Mechanics Conference, Newcastle, NSW, pp. 1–4, 1983.

[26] J. C. K. Cheung, J. D. Holmes, W. H. Melbourne, N. Lakshmanan, and P. Bowditch, “Pressures on a 1/10 scale model of the Texas Tech Building,” *J. Wind Eng. Ind. Aerodyn.*, vol. 71, pp. 529–538, 1997.

[27] R. P. Hoxey, A. P. Robertson, G. M. Richardson, and J. L. Short, “Correction of wind-tunnel pressure coefficients for Reynolds number effect,” vol. 69–71, pp. 547–555, 1997.

[28] R. P. Hoxey, A. . Robertson, G. M. Richardson, and J. L. Short, “Observations of Reynolds number sensitivity in the separated flow region on a bluff body,” *J. Wind Eng. Ind. Aerodyn.*, vol. 73, pp. 231–249, 1998.

[29] M. R. Goliber, “Pressure distribution on the roof of a model low- rise building tested in a boundary layer wind tunnel,” 2009.

[30] X. X. Cheng, L. Zhao, Y. J. Ge, J. Dong, and C. Demartino, “A comprehensive high Reynolds number effects simulation method for wind pressures on cooling tower models,” *Wind Struct. An Int. J.*, vol. 24, no. 2, pp. 119–144, 2017.

[31] L. S. Cochran and J. E. Cermak, “Full- and model-scale cladding pressures on the Texas Tech University experimental building,” *J. Wind Eng. Ind. Aerodyn.*, vol. 43, no. 1, pp. 1589–1600, 1992.

[32] M. Moravej, “Investigating scale effects on analytical methods of predicting peak wind loads on buildings,” FIU Electronic Theses and Dissertations. 3799, 2018.

[33] M. A. Mooneghi, P. Irwin, and A. G. Chowdhury, “Partial turbulence simulation method for predicting peak wind loads on small structures and building appurtenances,” *J. Wind Eng. Ind. Aerodyn.*, vol. 157, pp. 47–62, 2016.

[34] M. Amini and A. M. Memari, “CFD-Based Evaluation of Elevated Coastal Residential Buildings under Hurricane Wind Loads,” *J. Archit. Eng.*, vol. in press, no. 3, pp. 1–19, 2021.

[35] M. Amini and A. Memari, “Evaluation of Various Retrofit Strategies for Existing Residential Buildings in Hurricane Prone Coastal Regions,” in *5th Residential Building Design & Construction Conference*, 2020, no. March.

[36] American Society of Civil Engineering (ASCE), *Minimum Design Loads and Associated Criteria for Buildings and Other Structures (ASCE/SEI 7-16)*. 2016.

[37] J. H. Kim, M. Moravej, E. J. Sutley, A. Chowdhury, and T. N. Dao, “Observations and analysis of wind pressures on the floor underside of elevated buildings,” *Eng. Struct.*, vol. 221, no. July, p. 111101, 2020.

[38] N. Abdelfatah, A. Elawady, P. Irwin, and A. G. Chowdhury, “Wind Pressure Distribution on Single-Story and Two-Story Elevated Structures,” in *5th Residential Building Design & Construction Conference*, 2020, pp. 1–8.

[39] AS/NZS 1170.2, “Australian and New Zealand wind loading standard, Structural design actions. Part 2, Wind actions,” *AS/NZS 1170.2*, vol. 2011, no. 1170 2:2011, p. 96, 2011.

[40] S. Murakami, “Overview of turbulence models applied in CWE–1997,” *J. Wind Eng. Ind. Aerodyn.*, vol. 74–76, pp. 1–24, 1998.

[41] T. van Hooff, B. Blocken, and Y. Tominaga, “On the accuracy of CFD simulations of cross-ventilation flows for a generic isolated building: Comparison of RANS, LES and experiments,” *Build. Environ.*, vol. 114, pp. 148–165, 2017.

[42] C.-H. Hu, M. Ohba, and R. Yoshie, “CFD modelling of unsteady cross ventilation flows using LES,” *J. Wind Eng. Ind. Aerodyn.*, vol. 96, pp. 1692–1706, 2008.

[43] Y. Akamine, T. Kurabuchi, M. Ohba, T. Endo, and M. Kamata, “A CFD Analysis of the Air Flow Characteristics at an Inflow Opening,” *Int. J. Vent.*, vol. 2, no. 4, pp. 431–437, Apr. 2004.

[44] S. Emmerich and K. McGrattan, “Application of a Large Eddy Simulation Model to Study Room Airflow.,” ASHRAE Transactions, , -1, 1998.

[45] C. K. Choi and D. K. Kwon, “Wind tunnel blockage effects on aerodynamic behavior of bluff body,” *Wind Struct. An Int. J.*, vol. 1, no. 4, pp. 351–364, 1998.

[46] A. G. Chowdhury *et al.*, “Large-Scale Experimentation Using the 12-Fan Wall of Wind to Assess and Mitigate Hurricane Wind and Rain Impacts on Buildings and Infrastructure Systems,” *J. Struct. Eng.*, vol. 143, no. 7, p. 04017053, 2017.

[47] A. G. Chowdhury, K. Vutukuru, and M. Moravej, “Full- and Large-Scale Experimentation Using the Wall of Wind to Mitigate Wind Loading and Rain Impacts on Buildings and Infrastructure Systems,” in *11th Structural Engineering Convention*, 2018.

[48] H. P. A. H. Irwin, K. R. Cooper, and R. Girard, “Correction of distortion effects caused by tubing systems in measurements of fluctuating pressures,” *J. Wind Eng. Ind. Aerodyn.*, vol. 5, no. 1, pp. 93–107, 1979.

[49] ESDU (Engineering Sciences Data Unit), “Characteristics of atmospheric turbulence near the ground Part III : variations in space and time for strong winds.,” vol. 9232, no. October 1986, 2001, pp. 1–42.

[50] J. He, F. Pan, and C. S. Cai, “Assessment of ASCE 7-10 for wind effects on low-rise wood frame buildings with database-assisted design methodology,” *Wind Struct. An Int. J.*, vol. 27, no. 3, pp. 163–173, 2018.

[51] M. Moravej, P. Irwin, I. Zisis, A. G. Chowdhury, and B. Hajra, “Effects of roof height on local pressure and velocity coefficients on building roofs,” *Eng. Struct.*, vol. 150, pp. 693–710, 2017.

[52] N. Abdelfatah, A. Elawady, P. Irwin, and A. G. Chowdhury, “Experimental investigation of wind impact on low-rise elevated residences,” *Eng. Struct.*, vol. 257, no. March, p. 114096, 2022.

[53] N. Abdelfatah, A. Elawady, P. Irwin, and A. G. Chowdhury, “A study of aerodynamic pressures on elevated houses,” *Wind Struct. An Int. J.*, vol. 31, no. 4, pp. 335–350, 2020.

[54] B. Blocken, T. Stathopoulos, and J. Carmeliet, “CFD simulation of the atmospheric boundary layer: wall function problems,” *Atmos. Environ.*, vol. 41, no. 2, pp. 238–252, 2007.

[55] R. Patel, S. Ramani, S. Murakami, A. Mochida, Y. Hayashi, and S. Sakamoto, “Determination of Optimum Domain Size for 3D Numerical Simulation in ANSYS CFX,” *Int. J. Innov. Res. Sci. Eng. Technol. (An ISO Certif. Organ.*, vol. 3297, no. 6, pp. 4671–4679, 2007.

[56] A. Mochida, Y. Tominaga, and R. Yoshie, “AIJ Guideline for Practical Applications of CFD to Pedestriau Wind Environment around Buildings,” in *The Fourth International Symposium on Computational Wind Egineering (CWE2006)*, 2006, pp. 533–536.

[57] E. Näslund, P. M. Hellström, and J. G. Kral, *The Gut and Food Intake: An Update for Surgeons*, vol. 5, no. 5. 2001.

[58] S. M. Salim and S. C. Cheah, “Wall Y+ Strategy for Dealing with Wall-bouded Turbulent Flows,” in *Proceedings of the International MultiConference of Engineers and Computer Scientists*, 2009, vol. II.

[59] T. M. Soe and S. Y. Khaing, “Comparison of Turbulence Models for Computational Fluid Dynamics Simulation of Wind Flow on Cluster of Buildings in Mandalay,” *Int. J. Sci. Res. Publ.*, vol. 7, no. 8, pp. 337–350, 2017.

[60] A. Chaudhari, “Large Eddy Simulation for Large Eddy Simulation for Atmospheric Boundary Layer (ABL),” *Presentation*, p. 24, 2012.

[61] M. Amini and A. M. Memari, “LES simulations of wind - induced pressure on the floor system underside of elevated buildings,” *Wind Struct.*, vol. 5, pp. 397–407, 2021.

[62] F. Xing, D. Mohotti, and K. Chauhan, “Study on localised wind pressure development in gable roof buildings having different roof pitches with experiments, RANS and LES simulation models,” *Build. Environ.*, vol. 143, no. May, pp. 240–257, 2018.

[63] N. Abdelfatah and A. Elawady, “Numerical investigation of wind actions on elevated houses,” in *6th AAWE workshop*, 2021, pp. 94–97.

[64] H. Schlichting, *Boundary-Layer Theory. 6th Edition*. McGraw-Hill Book Company, New York., 1968.

[65] U. Y. Jeong, H.-M. Koh, and H. S. Lee, “Finite element formulation for the analysis of turbulent wind flow passing bluff structures using the RNG k−ε model,” *J. Wind Eng. Ind. Aerodyn.*, vol. 90, no. 3, pp. 151–169, 2002.

[66] Y. Tominaga, S. Akabayashi, T. Kitahara, and Y. Arinami, “Air flow around isolated gable-roof buildings with different roof pitches: Wind tunnel experiments and CFD simulations,” *Build. Environ.*, vol. 84, pp. 204–213, 2015.

[67] V. Yakhot, S. A. Orszag, S. Thangam, T. B. Gatski, and C. G. Speziale, “Development of turbulence models for shear flows by a double expansion technique,” *Phys. Fluids A*, vol. 4, no. 7, pp. 1510–1520, 1992.

[68] J. Franke, A. Hellsten, H. Schlünzen, and B. Carissimo, “Best Practice Guideline for the CFD Simulation of Flows in the Urban Environment: COST Action 732 Quality Assurance and Improvement of Microscale meteorological models,” *Meteorol. Model. Meteorol. Inst. Univ. Hamburg, Ger.*, vol. 44, p. 51, Jan. 2007.

[69] C.-K. Choi and D. K. Kwon, “Wind tunnel blockage effects on aerodynamic behavior of bluff body,” *Wind Struct. An Int. J.*, vol. 1, pp. 351–364, Sep. 1998.

[70] H. K. Versteeg and W. Malalasekera, *An Introduction to Computational Fluid Dynamics: The finite volume method 2nd Ed*, vol. 6, no. 4. Harlow: Pearson Education, 2007.

[71] C. Gorlé, J. Beeck, and P. Rambaud, “RANS CFD modeling of particle dispersion behind a rectangular building in the atmospheric boundary layer,” *5th Eur. African Conf. Wind Eng. EACWE 5, Proc.*, Jan. 2009.

[72] P. J. Richards and R. P. Hoxey, “Appropriate boundary conditions for computational wind engineering models using the k-ϵ turbulence model,” *J. Wind Eng. Ind. Aerodyn.*, vol. 46–47, pp. 145–153, 1993.

[73] Y. Jiang, M. Su, and Q. Chen, “Using large eddy simulation to study airflows in and around buildings,” *ASHRAE Trans.*, vol. 109 PART 2, no. 2, pp. 517–526, 2003.

[74] A. M. Aly and H. Gol-Zaroudi, “Peak pressures on low rise buildings: CFD with les versus full scale and wind tunnel measurements,” *Wind Struct. An Int. J.*, vol. 30, no. 1, pp. 99–117, 2020.

[75] H. A. Ibrahim, A. Elawady, and D. O. Prevatt, “Performance and Fragility of Elevated Structures During Hurricane Events,” in *6th American Association for Wind Engineering Workshop*, 2021, pp. 110–112.

[76] F. Nicoud and F. Ducros, “Subgrid-scale stress modelling based on the square of the velocity,” *Flow Meas. Instrum.*, vol. 62, pp. 183–200, 1999.

[77] T. S. Lund, “The Use of Explicit Filters in Large Eddy Simulation,” *Comput. Math. with Appl.*, vol. 46, no. 4, pp. 603–616, 2003.

[78] M. Weickert, G. Teike, O. Schmidt, and M. Sommerfeld, “Investigation of the LES WALE turbulence model within the lattice Boltzmann framework,” *Comput. Math. with Appl.*, vol. 59, no. 7, pp. 2200–2214, 2010.

[79] O. Ben-Nasr, A. Hadjadj, A. Chaudhuri, and M. S. Shadloo, “Assessment of subgrid-scale modeling for large-eddy simulation of a spatially-evolving compressible turbulent boundary layer,” *Comput. Fluids*, vol. 151, pp. 144–158, 2017.

[80] Z. Liu, “Investigation of flow characteristics around square cylinder with inflow turbulence,” *Eng. Appl. Comput. Fluid Mech.*, vol. 6, no. 3, pp. 426–446, 2012.

[81] C. Y. Lee and S. Cant, “Assessment of LES Subgrid-scale Models and Investigation of Hydrodynamic Behaviour for an Axisymmetrical Bluff Body Flow,” *Flow, Turbul. Combust.*, vol. 98, no. 1, pp. 155–176, 2017.

[82] D. A. Jones and D. B. Clarke, “Simulation of Flow Past a Sphere using the Fluent Code,” p. 35, 2008.

[83] F. Mathey, D. Cokljat, J. P. Bertoglio, and E. Sergent, “Assessment of the vortex method for large eddy simulation inlet conditions,” *Prog. Comput. Fluid Dyn.*, vol. 6, no. 1–3, pp. 58–67, 2006.

[84] E. Sergent, “Vers une méthodologie de couplage entre la Simulation des Grandes Echelles et les modèles statistiques,” 2002.

[85] M. El Rafei, L. Könözsy, and Z. Rana, “Investigation of numerical dissipation in classical and Implicit Large Eddy Simulations,” *Aerospace*, vol. 4, no. 4, 2017.

[86] P. Fernandez, “High-Order Implicit Large-Eddy Simulation for Transitional Aerodynamics Flows,” 2016.

[87] F. Sadek and E. Simiu, “Peak Non-Gaussian Wind Effects for Database-Assisted Low-Rise Building Design,” *J. Eng. Mech.*, vol. 128, no. 5, pp. 530–539, 2002.

VITA

NOURHAN ABDELFATAH

Born, GIZA, EGYPT

2007-2012	B.Sc., Civil Engineering Ain Shams University Cairo, Egypt
2013-2017	M.Sc., Structural Engineering Ain Shams University Cairo, Egypt
2013-2017	Teaching Assistant, Structural Engineering Ain Shams University Cairo, Egypt
2018-2022	Graduate Research Assistant Florida International University, CEE Dept. Miami, Florida, USA
2018 -2022	Doctoral Candidate Florida International University, CEE Dept. Miami, Florida, USA
2021	Recipient of the Dissertation Year Fellowship (DYF), Florida International University, CEE Dept. Miami, Florida, USA

PUBLICATIONS AND PRESENTATIONS

[J1] N. Abdelfatah, A. Elawady, P. Irwin, and A. G. Chowdhury, " A study of aerodynamic pressures on elevated houses," in *Wind and Structures An International Journal.*, vol. 31, no. 4, pp. 335-350, October 2020

[J2] N. Abdelfatah, A. Elawady, P. Irwin, and A. G. Chowdhury, " Experimental investigation of wind impact on low-rise elevated residences," in *Engineering Structures.*, vol. 257, p. 114096, March 2022

[C1] N. Abdelfatah, A. Elawady, P. Irwin, and A. G. Chowdhury, " Pressure coefficient distribution on elevated houses," in *5th American Association of Wind Engineering Work*, Miami, Florida, August 2018.

[C2] N. Abdelfatah, A. Elawady, P. Irwin, and A. G. Chowdhury, " Experimental study of wind effect on single story elevated house," in *2nd National Conference on Wind Engineering*, Bucharest, Romania, June 2019.

[C3] N. Abdelfatah, A. Elawady, P. Irwin, and A. G. Chowdhury, " Aerodynamic Study of Elevated Houses," in *15th International Conference on Wind Engineering*, Beijing, China, September 2019.

[C4] N. Abdelfatah, A. Elawady, P. Irwin, and A. G. Chowdhury, " Wind Pressure Distribution on Single-Story and Two-Story Elevated Structures," in *5th Residential Building Design & Construction Conference*, Pennsylvania, March 2020.

[C5] N. Abdelfatah, A. Elawady, P. Irwin, and A. G. Chowdhury, " Wind Effects on Coastal Elevated Structures," in *9th International Colloquium on Bluff Body Aerodynamics and Applications*, July 2020.

[C6] N. Abdelfatah, A. Elawady," Numerical investigation of wind actions on elevated houses" in *6th AAWE Workshop*, May 2021

[C7] N. Abdelfatah, A. Elawady," CFD Simulations of Elevated Houses Aerodynamics with Different Aspect Ratios" in 14*th ACWE conference*, May 2022

[D.S.] M. Jamal, N. Abdelfatah, C. Feng, A. Elawady (2019) "Large Scale Testing to Investigate the Aerodynamics of Elevated Houses", *Undergraduate Research Experience (REU), NHERI 2019* DesignSafe-CI. https://doi.org/10.17603/ds2-pd70-yg65.